DYNAMIC RANGE EXTENSION OF HETERODYNE FIBER-OPTIC INTERFEROMETERS VIA INSTANTANEOUS CARRIER MEASUREMENT

A Dissertation

Presented in Partial Fulfillment of the Requirements for the

Degree of Doctor of Philosophy

with a

Major in Electrical Engineering

in the

College of Graduate Studies

University of Idaho

by

David A. Mellick

April 2014

Major Professor: James F. Frenzel, Ph.D.

AUTHORIZATION TO SUBMIT
DISSERTATION

This dissertation of David Allen Mellick, submitted for the degree of Doctor of Philosophy with a major in Electrical Engineering and titled "Dynamic Range Extension of Heterodyne Fiber-Optic Interferometers Via Instantaneous Carrier Measurement," has been reviewed in final form. Permission, as indicated by the signatures and dates given below, is now granted to submit final copies to the College of Graduate Studies for approval.

Major Professor _____ Date _____
James F. Frenzel

Committee
Members _____ Date _____
Gregory W. Donohoe

_____ Date _____
Suat U. Ay

_____ Date _____
Michael J. Anderson

Department
Administrator _____ Date _____
Fred Barlow

Dean of the College
of Engineering _____ Date _____
Larry Stauffer

Final Approval and Acceptance by the College of Graduate Studies

_____ Date _____
Jie Chen

Abstract

Fiber-optic sensors are of interest in a wide range of fields. In particular, fiber-optic interferometers are ideally suited for acoustic and vibration measurement applications, such as in the oil exploration industry. Primary benefits of fiber-optic sensors include Electromagnetic Interference (EMI) immunity, remote interrogation, and the ability to multiplex hundreds of sensors on a single fiber. However, one issue impacting the adoption of fiber-optic sensing technology is limited dynamic range.

This dissertation presents a novel approach to extending the dynamic range of heterodyne modulated fiber-optic interferometers. By measuring and tracking the instantaneous heterodyne carrier frequency, a correction factor can be obtained to mitigate excession errors of the demodulator, thereby extending the high-end dynamic range.

Of particular importance to the dynamic range extension approach is how the carrier frequency is measured. Three methods of frequency discrimination are presented as part of this work. Two of the methods, Digital Instantaneous Frequency Measurement (DIFM) and Discrete Fourier Transform (DFT), are shown to be well suited for the extension technique. DIFM requires substantially fewer hardware resources, but DFT has a small performance advantage.

A MATLAB simulation script was developed to test the theory of this work. Simulations were conducted to test the viability of the individual frequency discrimination methods and the dynamic range extension approach itself. The simulations demonstrated the ability of the approach to provide a more than 20 dB dynamic range extension. The primary limitations of the approach are the available system bandwidth and the hardware resources required to measure that bandwidth.

The theory and simulations presented as part of this dissertation were verified through experimental testing. Both the DIFM and DFT variants of the approach were implemented in a Field Programmable Gate Array (FPGA) and tested under real-world conditions. The experimental results closely matched the simulations, and verified both as being capable of providing a reliable dynamic range extension of 20 dB or more.

Acknowledgments

First and foremost, I would like to thank my major professor Dr. James Frenzel. His guidance has helped me throughout my entire long and winding college experience. Without his unwavering support for my non-traditional college path, none of this would have been possible. I especially appreciate the added confidence boosts he provided when necessary.

I would also like to thank my entire committee, Dr. Gregory Donohoe, Dr. Suat Ay, and Dr. Michael Anderson. Discussions with them early on were instrumental in focusing the direction of my research. A special thank you also goes to the late Dr. Kenneth Noren, who served on the committee before his untimely passing. I had the pleasure of having Dr. Noren as an instructor for numerous courses.

Funding for this research was provided by the Naval Surface Warfare Center, Carderock Division's (NSWCCD), Section 219 fund. I would like to thank Dr. Jack Price, Dr. Paul Shang, Dr. Steve Potashnik, and Steve Finley for their support and backing.

A thank you goes to the "Bos Newton" duo. I sincerely appreciate all of your support in figuring out how to build the sensors and in helping setup the experimental tests for me. Thanks also for keeping me laughing through all the stress.

Lastly, I want to thank my wife and family. I could not have done this without their support. To my wife, thank you for picking up the slack at home during my long hours of work. Thank you for also tolerating my mood swings when things weren't going so well. Finally, thank you to my little girl Elizabeth Hope. Your arrival time has done more to keep me motivated and on schedule than anything else.

Table of Contents

List of Figures

List of Acronyms

ADC Analog to Digital Converter

AOM Acousto-Optic Modulator

ASE Amplified Spontaneous Emission

CNR Carrier to Noise Ratio

DDS Direct Digital Synthesizer

DFT Discrete Fourier Transform

DIFM Digital Instantaneous Frequency Measurement

DPLL Digital Phase Locked Loop

DRE Dynamic Range Extension

DWDM Dense Wavelength Division Multiplexing

EDFA Erbium Doped Fiber Amplifier

EMI Electromagnetic Interference

EOM Electro-Optic Modulator

FBG Fiber Bragg Grating

FFT Fast Fourier Transform

FIR Finite Impulse Response

FM Frequency Modulated

FPGA Field Programmable Gate Array

IFM Instantaneous Frequency Measurement

PECM Period Expansion/Contraction Measurement

PGC Phase Generated Carrier

PLL Phase Locked Loop

PMDI Path Matched Differential Interferometry

PMF Polarization-Maintaining Fiber

RIN Relative Intensity Noise

SDR Software Defined Radio

SMF Single-Mode Fiber

SOA Semiconductor Optical Amplifier

TDM Time Division Multiplexing

TIA Transimpedance Amplifier

TVR Transmit Voltage Response

List of Symbols

ν	Laser frequency (Hz)
ϕ_r	Reference arm phase (radians)
ϕ_s	Sensor arm phase (radians)
τ_{adc}	ADC sample time (seconds)
θ_m	Multi-tone fringe rate (radians per second)
θ_n	Broadband noise fringe rate (radians per second)
θ_{demod}	Demodulator fringe rate (radians per second)
θ_{s+n}	Sinusoidal signal plus noise fringe rate (radians per second)
A_s	Peak sinusoidal amplitude (radians)
B_{if}	Instantaneous carrier frequency bandwidth (Hz)
c	Free space speed of light (299,792,458 m / s)
f_c	Heterodyne carrier frequency (Hz)
f_d	Filtered output demodulation rate (Hz)
f_s	Sinusoidal modulation frequency (Hz)
f_{samp}	Demodulator sample rate (Hz)
i_{pd}	Photodiode current (Amps)

k	Optical wavenumber = $2\pi\lambda$
L_r	Length of fiber reference coil (Meters)
L_s	Length of fiber sensing coil (Meters)
n_{eff}	Effective fiber-optic index of refraction (≈ 1.465)
P	Optical power at the photodiode (Watts)
q	Electron charge (1.602 x 10^{-19} coulombs)
r	Photodiode responsivity (Amps/Watt)
R_l	Transimpedance amplifier load resistance (ohms)
T_e	Equivalent thermal temperature (°K)
V	Polarization visibility ranging from 0 to 1
y_{out}	DIFM output value

Chapter 1 Introduction

This dissertation presents an original approach to extend the dynamic range of heterodyne fiber-optic sensors. Fiber-optic sensors are of significant interest to the research community for their numerous potential advantages over traditional electronic-based sensors. However, dynamic range limitations of fiber-optic sensors have prevented researchers and system developers from capitalizing on their benefits in some applications. One example of these limitations was encountered during the design and development of a new large-scale fiber-optic hydrophone array to be utilized as an acoustic research and development platform. It was determined that even after optimizing design parameters to maximize dynamic range, the fiber-optic sensors would fail to meet the system requirements by nearly 20 dB. This led to a review of current dynamic range extension approaches within the literature. After finding few available options, the approach presented within was developed.

1.1 Motivation

Fiber-optic sensors are of significant interest to researchers and system developers because of their benefits. One such benefit is their wide dynamic range. This wide dynamic range, however, is still insufficient in a number of highly desirable applications. This is partially evident by the number and type of fiber-optic sensor systems currently deployed in real-world applications. Despite the fact that the majority of the research in the field was conducted in the 1980's and 1990's, only a few select fiber-optic sensor systems have reached production stage. These systems all have modest dynamic range requirements. There are currently no large-scale fiber-optic interferometric sensor systems in use by the research and development community, despite their significant benefits.

The motivation behind this dissertation is to increase the dynamic range of fiber-optic sensors such that their benefits can be realized in a wider array of applications. One such application where fiber-optic sensors are highly desired is in test and measurement systems for the acoustic research community. Factors such as Electromagnetic Interference (EMI) immunity,

remote sensor interrogation capabilities, and significantly lower system costs are commonly stated as advantages. These benefits were primary justifications for the development of a new large-scale hydrophone array utilizing fiber-optic sensing technology. However, it became evident in the early stages of development that the new array would not be able to meet the dynamic range requirements utilizing normal optimization techniques. Therefore, part of the motivation behind this dissertation is to achieve the necessary dynamic range increase such that this and other planned arrays will be able to fully meet their specified requirements. It should also be noted that the dynamic range increases which can be achieved with the proposed method can be utilized to develop larger Time Division Multiplexing (TDM) sensor arrays without sacrificing additional dynamic range.

1.2 Contributions

The contents of this dissertation contains several unique contributions to the field of fiber-optic interferometric sensing. While the issue of limited dynamic range has been discussed in the literature, little documented work has been found which provides a viable approach to dynamic range extension of large-scale interferometric systems. Therefore, the primary contribution of this dissertation is presenting a low overhead, reliable approach to extending the dynamic range of fiber-optic interferometers. It will be shown that this increase can be as much as 20 dB while requiring minimal hardware resources in an all-digital heterodyne demodulator. There are, however, limitations to the approach presented and they will be documented in detail.

One critical requirement of the dynamic range extension approach presented here is the ability to measure the instantaneous carrier signal in a heterodyne interferometer. The rate at which it must be measured and tracked presents several challenges. This dissertation will explore three unique methods for instantaneous carrier measurement. The first method is known as Digital Instantaneous Frequency Measurement (DIFM) and is based on an autocorrelation measurement of the digitized carrier signal. The second approach is based on Discrete Fourier Transform (DFT) measurements of specific frequencies within the bandwidth of heterodyne demodulator. The last method is known as Period Expansion/Contraction

Measurement (PECM). This approach measures the amount of expansion or contraction in the heterodyne carrier in the time domain. The advantages and limitations of all three methods will be discussed.

The high-end dynamic range limitations of an interferometric system are typically determined through a process known as fringe rate analysis. This process compares the fringe rate of the demodulator to the fringe rate of the maximum anticipated received signals. Literature covering fringe rate analysis typically only discusses the trivial case of single sinusoidal modulation. Fringe rate analysis of more complicated waveforms has been discussed in the literature, however, only recommended approaches have been suggested. No actual analysis has been documented. This dissertation provides fringe-rate analysis of single-tone sinusoidal, multi-tone sinusoidal, and broadband noise modulation. It also examines the case of single sinusoidal modulation under the impact of broadband noise conditions.

This dissertation makes unique contributions to the field of fiber-optic interferometric sensing in the areas of dynamic range extension and instantaneous carrier measurement. Experimental evaluations of both are documented within. These results provide guidance on selecting the most appropriate solution to fiber-optic system developers.

1.3 Dissertation Organization

Chapter 2 of this dissertation provides an overview of fiber-optic interferometric systems and provides a basis for the research presented within. This chapter covers basic fiber-optic interferometric configurations and TDM approaches. It also documents an all-digital demodulation approach which enables the dynamic range extension approach presented within this dissertation.

Chapter 3 examines the dynamic range considerations of fiber-optic interferometers. Various noise sources are presented which define the low-end of the dynamic range. Demodulation bandwidth limitations are analyzed which define the high-end of the dynamic range. With the dynamic range limitations addressed, a review of current dynamic range extension techniques found in the literature is provided.

Signal fringe rate analysis is the basis of Chapter 4. Since most coverage of fringe rate analysis found in the literature only address the simple case of single sinusoidal modulation, this chapter provides a more in-depth coverage of the topic. Being able to correctly calculate the expected fringe rate of a signal is critical in determining the maximum available dynamic range of a system. This chapter provides fringe rate analysis for several common modulation waveforms including single-tone sinusoidal, multi-tone sinusoidal, broadband noise, and single-tone sinusoidal with broadband noise.

Chapter 5 examines at various options for measuring the instantaneous heterodyne carrier frequency. The first part of the chapter is a literature review that explores different approaches for the application at hand. Three unique methods are then introduced. The first is based on an autocorrelation measurement of the carrier signal. This method is known as DIFM. The second approach uses discrete Fourier analysis to track specific carrier frequencies of the demodulator. A third method, known as PECM, involves determining the instantaneous carrier frequency from the amount of expansion or contraction of the carrier signal in the time domain. The advantages, limitations, and noise susceptibility of all three methods are presented.

The novel dynamic range extension technique is presented in Chapter 6. By measuring the instantaneous heterodyne carrier frequency, two critical pieces of information are obtained about the interferometer: the direction of instantaneous phase rotation and the instantaneous angular velocity. This chapter explores how these two pieces of information can be utilized to increase the dynamic range. This approach, however, is not without its limitations. The limitations to which this method can be utilized are defined.

Chapter 7 provides the experimental results for this dissertation. Dynamic range extension testing is performed for both the DIFM and DFT methods of frequency discrimination. The frequency tracking abilities are also tested and documented. An analysis is conducted to compare the results of the simulations to the results of the experimental testing for both techniques.

Chapter 8 concludes this dissertation. It includes a review of the contributions of this work and addresses the potential for future research.

Chapter 2 Fiber-Optic Interferometers

This chapter provides an introduction to fiber-optic interferometric technology. The requirements and process for heterodyne modulation are addressed, as are demodulation techniques for extracting the phase signal of interest. Of particular importance is the last section of this chapter in which an all-digital demodulation process is discussed. This new demodulation approach allows for the dynamic range extension technique presented within.

2.1 Fiber-Optic Sensors

Much of the research in the field of fiber-optic sensors dates back more than 30 years. In that time, numerous types of fiber-optic sensor technologies were developed. Fiber-optic sensors have been designed to sense various parameters of light. These include intensity changes, polarization states, and wavelength shifts [1]. Their popularity is due to their numerous potential benefits. These benefits include EMI immunity, remote interrogation capabilities, and the ability to multiplex hundreds of sensors in both time and wavelength on a single fiber. Two of the most popular fiber-optic technologies are interferometers and Fiber Bragg Gratings (FBGs).

Fiber Bragg gratings have had the most commercial success to date. FBGs are small changes in the refractive index that are etched into the surface of a fiber-optic cable. Numerous types of FBGs exist, each with their own unique characteristics. For optical sensing, the reflective FBG is most often used. The changes in refractive index cause the grating to reflect a specific wavelength of light [2]. Strains applied to the FBG will cause a shift in the wavelength reflected. By measuring the reflected wavelength of the FBG as it is modulated, the signal of interest can be recovered. FBGs have the benefits that they are simple to use, are inexpensive, and thousands of sensors can easily be multiplexed on a single fiber. The problems with FBGs are that they do not have the sensitivity or the dynamic range required by many applications. Although not as simple or cheap as FBGs, fiber-optic interferometers are the primary option

for applications that require high sensitivity and wide dynamic range.

Fiber-optic interferometers provide the highest sensitivity and widest dynamic range of any available fiber-optic sensor technology. They are also capable of remote interrogation and can be multiplexed into large-channel-count arrays. Because of these characteristics, fiber-optic interferometers are generally well suited for applications such as large acoustic and vibration sensing arrays. However, for some applications, even the wide dynamic range of the interferometer is still insufficient. This is the primary motivation behind the dynamic range extension approach presented within. An introduction to fiber-optic interferometer technology is now provided.

2.2 Mach-Zehnder

Interferometers, as their name suggests, are based on the interference of sinusoidally oscillating light waves. This involves combining two beams of light which travel separate paths before being recombined. The simplest fiber-optic interferometer is based on the popular bulk optic interferometer known as the Mach-Zehnder. Figure 2.1 shows the basic fiber-optic Mach-Zehnder interferometer configuration. It is assembled using two coils of fiber, two directional fiber-optic couplers, a light source, and one or more photodetectors. One of the fiber coils is considered the signal arm while the other is the reference. The light source is typically a long coherence laser such that when the light passes through the fiber arms and recombines back at the photodetector the two beams will mix coherently. The photodetector then generates an output current which, for an ideal lossless system using 50/50 couplers, is given by 2.1 [3].

$$i_{pd} = rP + rPV\cos(\phi_s - \phi_r) \tag{2.1}$$

P is the total amount of optical power hitting the photodetector with a responsivity of r. V is known as the polarization visibility and can range in value from 0 to 1 depending on the orthogonality of the polarization states between the signal and reference arms of the

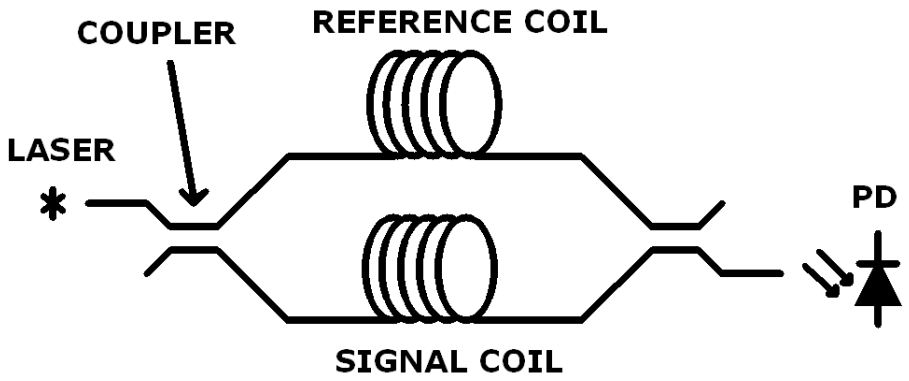

Figure 2.1: Mach-Zehnder fiber-optic interferometer

interferometer. For simplicity, V will always be assumed to be maximized at 1 within this dissertation. The terms ϕ_s and ϕ_r are the relative phases of the light in the signal and the reference arms, the magnitudes of which can be determined by 2.2.

$$\phi = n_{eff} k L \tag{2.2}$$

L is the total length of the fiber in the arm, n_{eff} is the effective refractive index of the fiber, and k is the optical wavenumber ($k = 2\pi\lambda$) [4]. A change in any one of these variables will shift the phase of the light exiting the arm, thereby changing the magnitude of i_{pd}. This is the basic mechanism utilized for fiber-optic interferometric sensing. For most fiber-optic interferometers the strategy is to couple a mechanical strain to the fiber in order to induce a change in L. However, strain applied to a fiber will also induce a change in n_{eff}. One problem is that temperature also heavily influences n_{eff}, making it impossible to distinguish between mechanical strains applied to the fiber and thermal fluctuations. But, since thermal fluctuations are typically low frequency in nature, they can be high-pass filtered from the data of interest. Because of the thermal effects and difficulties in making absolute measurements, fiber-optic interferometers are generally only considered suitable for dynamic sensing applications. Taking the derivative of equation 2.2 yields 2.3, the time varying phase equation. Equation 2.3 is useful in determining an interferometer's sensitivity to dynamic fluctuations, both intended and unintended sources.

$$\frac{d\phi}{\phi} = \frac{dL}{L} + \frac{dn_{eff}}{n_{eff}} + \frac{dk}{k} \tag{2.3}$$

Another problem encountered with the Mach-Zehnder interferometer is known as interferometric signal fading. From 2.1, it can been seen that the photodetector output is dependent on the cosine of the phase difference ($\Delta\phi = \phi_s - \phi_r$). If $\Delta\phi$ is biased around $\frac{\pm(2n+1)\pi}{2}$, also known as quadrature, then for a small change in $\Delta\phi$ a large change in i_{pd} will occur. However, if $\Delta\phi$ is biased at $\pm n\pi$, then the change in i_{pd} will be much smaller and heavily distorted. This is depicted in Figure 2.2. Early fiber-optic sensor researchers simply waited for the phases to drift into quadrature before acquiring data. Since this was not really practical, they developed several methods for overcoming interferometric signal fading [1]. One of the first approaches used was feedback to control a fiber-stretching phase modulator inserted into the reference arm of the interferometer to maintain the quadrature bias point. This, however, complicated the sensor design and made remote interrogation nearly impossible. Researchers then began investigating different types of modulation.

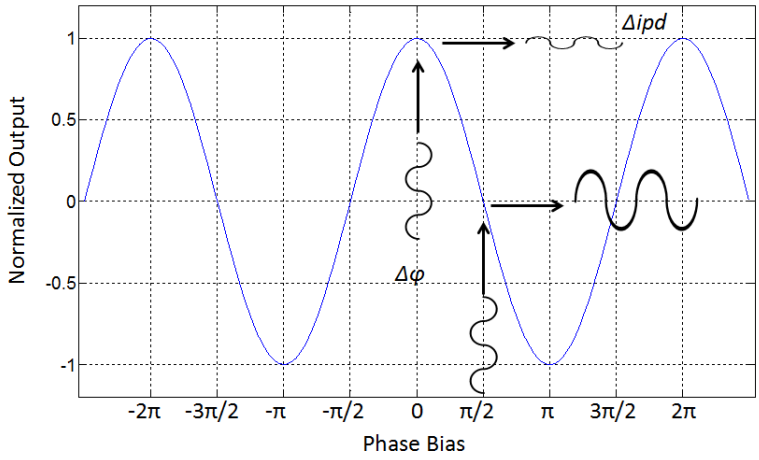

Figure 2.2: Interferometric signal fading

Although numerous types of modulation schemes have been developed for fiber-optic interferometers, the two most popular are known as heterodyne and Phase Generated Carrier (PGC) homodyne. PGC homodyne was one of the first modulation schemes developed for overcoming the signal fading problem. It uses a phase modulating device, often a piezoelectric fiber-stretcher, to induce a phase shift carrier onto the light passing through the

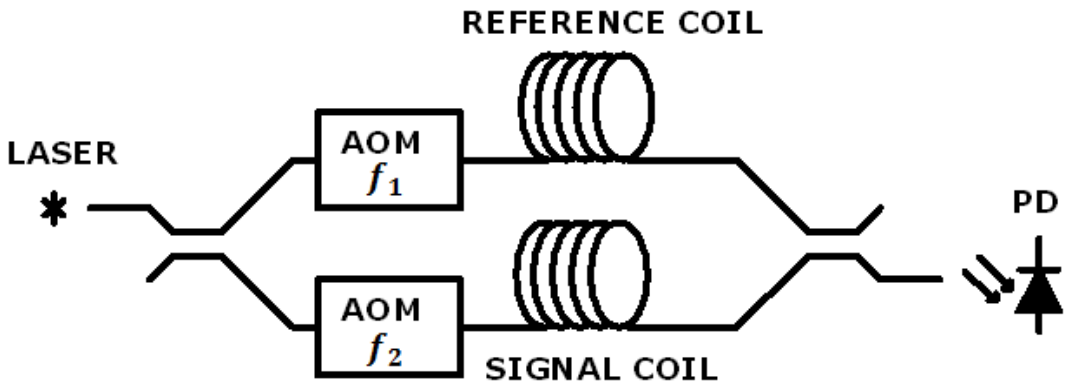

Figure 2.3: Heterodyne modulated Mach-Zehnder interferometer

reference arm. A demodulation technique commonly referred to as "differentiate and cross-multiply" was used by the receiver to extract the phase signal of interest from the carrier [3]. While PGC modulation is still widely used in fiber-optic sensor systems, it has in recent years largely been replaced by heterodyne modulation.

2.3 Heterodyne Mach-Zehnder

Heterodyne modulation is one technique for overcoming the interferometric signal fading problem in fiber-optic interferometers. Its popularity in recent years is largely due to its reduced demodulation processing requirements when compared to PGC demodulation. PGC also requires twice the bandwidth to achieve the same dynamic range when compared to the heterodyne approach [5]. Figure 2.3 shows a basic heterodyne modulated Mach-Zehnder fiber-optic interferometer.

The heterodyne modulated Mach-Zehnder includes the addition of an Acousto-Optic Modulator (AOM) to each arm of the interferometer. The AOM shifts the frequency of the incoming light by the frequency of the drive signal. The AOMs of Figure 2.3 are driven at frequencies f_1 and f_2 such that a resulting carrier frequency of $f_c = f_1 - f_2$ is generated in the photodetector current[1]. The photodetector current i_{pd} can now be determined from equation 2.4 [6].

[1]Appendix A provides the derivation of the heterodyne photodetector current equation.

$$i_{pd}(t) = rP + rPV\cos(2\pi f_c t + (\phi_s(t) - \phi_r(t))) \tag{2.4}$$

Assuming the reference fiber arm is well isolated from mechanical strains and temperature fluctuations, and ignoring the DC component of the output current, the time varying portion of i_{pd} can be written as

$$i_{pd\_sig}(t) = rPV\cos(2\pi f_c t + \phi_s(t)) \tag{2.5}$$

The significance of heterodyne modulation can be determined by examining equation 2.5. The i_{pd_sig} current is now a constant carrier at frequency f_c which is phase modulated by the phase of the light passing through the signal arm $\phi_s(t)$. This is in contrast to the basic Mach-Zehnder configuration in which the recovered signal was amplitude dependent. The phase modulated output of the heterodyne configuration not only mitigates the interferometric signal fading problem, it also reduces noise associated with optical amplitude fluctuations and polarization state changes.

While the heterodyne Mach-Zehnder is an improvement over the basic configuration, it does not allow for two highly desirable features of fiber-optic sensing: remote interrogation and TDM. Remote interrogation is not feasible since any additional fiber used, placed in either arm, to remote the location of the coils would be susceptible to unintended signals. TDM is not possible since the output of the heterodyne modulated Mach-Zehnder is continuous and does not allow for time division between sensors. Both of these capabilities can be realized by utilizing a pulsed heterodyne configuration.

2.4 Pulsed Heterodyne Michelson

Going to a pulsed heterodyne interferometer configuration allows for remote sensing and TDM. To do this, however, a Mach-Zehnder interferometer can no longer be used. The Mach-Zehnder is replaced with a Michelson interferometer. Figure 2.4 shows the basic

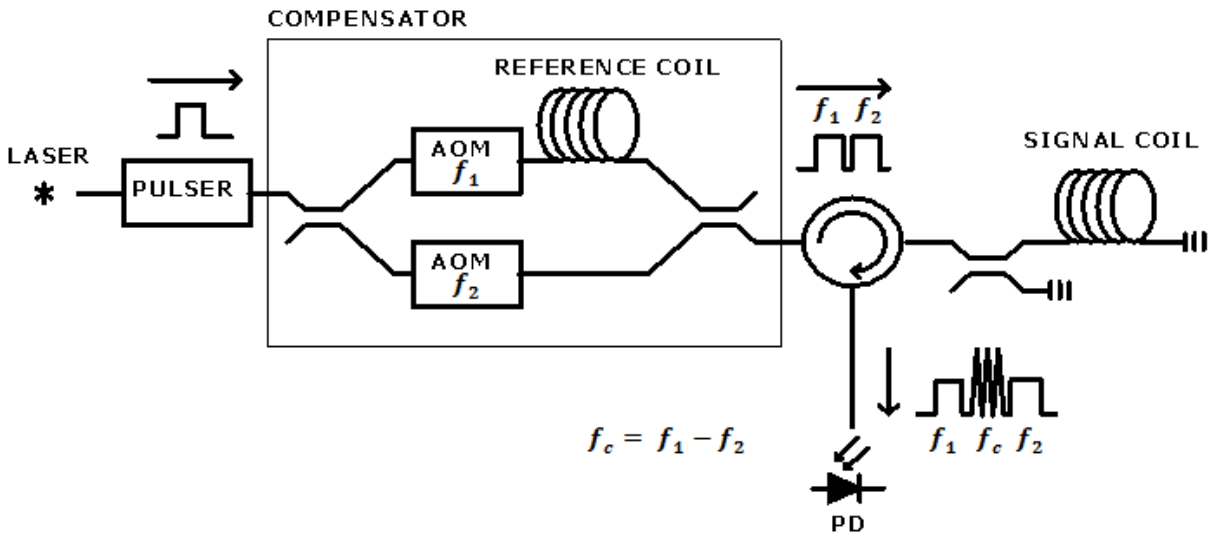

Figure 2.4: Pulsed heterodyne Michelson interferometer

configuration. In this configuration, the sensing fiber arm is removed from its normal Mach-Zehnder position and is placed at some remote location. Mirrors are added to the end of the sensor coil, creating a fiber-optic Michelson interferometer.

Optical pulses are used to interrogate the remote Michelson interferometer. The pulses are generated by the addition of an optical pulsing unit placed after the laser. Electro-Optic Modulators (EOMs), AOMs, or Semiconductor Optical Amplifiers (SOAs) can all be used for pulse generation, each with their own significant trade-offs. The optical pulses are launched into what is referred to as the compensating interferometer or the compensator. The compensator is a heterodyne modulated Mach-Zehnder interferometer with the sensing coil removed. The optical pulse that is launched into the compensator is split with an equal amount of optical power passing through each arm. The light in the reference arm is modulated by the AOM at f_1, while the light passing in the other is modulated at f_2. The pulse traveling in the reference coil is delayed in time by τ seconds, where the delay time τ is equal to the total delay time in the sensor coil, such that at the output of the compensator are now two pulses. One of the pulses is modulated at f_1. The other is modulated at f_2.

The two optical pulses are then launched towards the remotely located Michelson

interferometer. When the first pulse reaches the sensor 50% of the optical power is reflected by a mirror at the output of a directional coupler placed before the sensing coil. The other 50% of the first optical pulse travels through the sensing coil and is reflected by another mirror attached at the end of the coil. The optical delay time of the pulse in the sensing coil is equal to the delay time τ of the reference coil. The second pulse to enter the interferometer experiences the same power division and time delays. The reflected pulses then travel back to the photodetector and are overlapped in time as shown in Figure 2.4. Where the f_1 and the f_2 pulses overlap, the photodetector will generate a burst of heterodyne carrier signal at f_c. In this manner, for each optical pulse launched into the system a burst of heterodyne carrier is generated that can be demodulated by the receiver, allowing the phase signal of interest to be recovered.

The system architecture shown in Figure 2.4 is often referred to in the literature as Path Matched Differential Interferometry (PMDI) [4]. This is a result of the fact that the two optical pulses travel approximately the same path length, but that there can be a significant physical separation between the reference and the sensing coil. This separation allows the sensing coil to be located miles from the rest of the system and is one of the highly desirable benefits of fiber-optic sensing. Another benefit yet to be discussed is time-division multiplexing (TDM).

2.5 In-Line Michelson TDM

Time division multiplexing is one of the most desirable and most heavily researched areas of fiber-optic interferometry [7, 6, 4]. While numerous TDM architectures have been developed, this dissertation will primarily focus on the in-line Michelson array. In-Line Michelson TDM is an extension of the pulsed heterodyne configuration presented in the last section. Figure 2.5 shows a three sensor in-line array. The launch and receive hardware is the same as that depicted for the pulsed heterodyne Michelson interferometer in the last section.

Time division multiplexing is achieved by concatenating additional sensor coils together, separated by directional couplers with one end mirrored. The coupler ratios are carefully

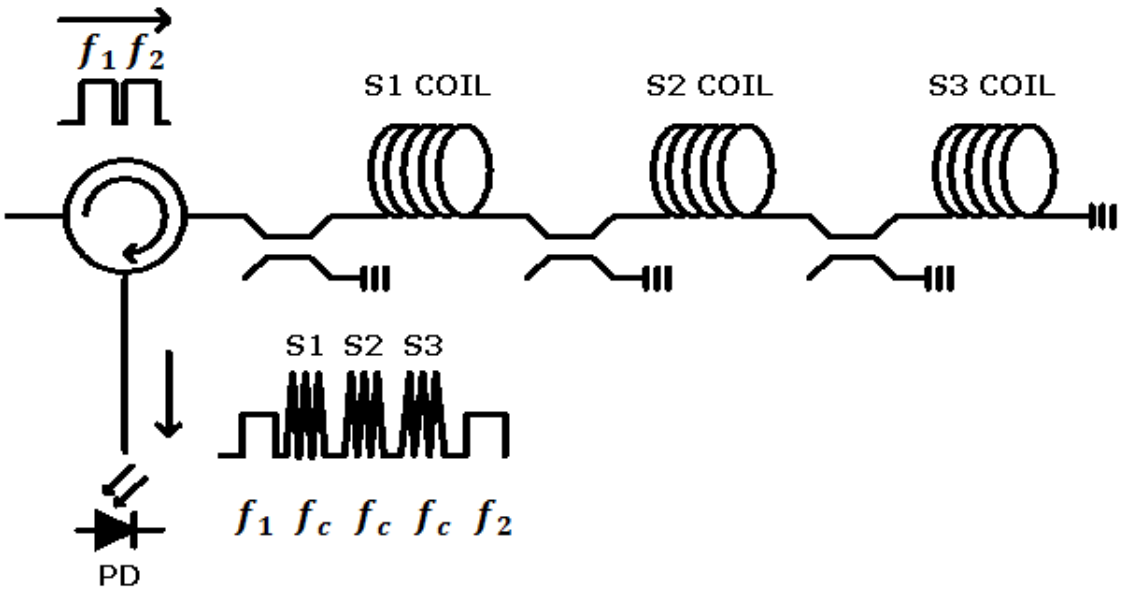

Figure 2.5: In-line Michelson TDM

selected such that the amount of light reflected from each coupler is approximately equal. However, in actual arrays, balancing the return light from the individual sensors is a non-trivial matter. Assuming balanced return levels, an optical waveform as shown in Figure 2.5 will be received by the photodetector. Each sensor coil, therefore, produces one burst of the heterodyne carrier. By properly gating the heterodyne bursts in time, the demodulator can recover the phase signal of interest from the individual sensors.

Numerous papers have been written on fiber-optic interferometric TDM. Arrays containing hundreds of sensors on a single fiber have been reported multiple times. Despite the popularity of TDM within the research community, TDM has one very significant drawback that is often overlooked. TDM reduces the maximum sample rate, and as will be shown later in this dissertation, reducing the sample rate will limit the sensors' maximum dynamic range. In many of the large TDM arrays reported on in the literature, this dynamic range reduction would greatly impact their viability for many applications.

2.6 Heterodyne Demodulation

Heterodyne modulated fiber-optic interferometric signals require demodulation at the receiver, also known as the demodulator or interrogation unit, in order to extract the phase signal of interest from the heterodyne carrier. Various approaches have been reported on in the literature to accomplish this task. The first widely used approach utilized a synchronous Zero-IF (Intermediate Frequency) front-end receiver, with the processing being handled by what is referred to as "differentiate and cross-multiply" analog circuitry [3]. This approach, however, suffered from numerous problems and, as a result, other methods were explored. The most widely used approach to date is referred to in the literature as a digital demodulator. This uses a synchronous Zero-IF analog front end, the outputs of which are also low-pass filtered in the analog domain. The low-pass filtered outputs are then digitized, with the acquired data being processed in the digital domain. Although this type of demodulator is referred to in the literature as digital, this dissertation will refer to them as analog since the most critical parts of the demodulation process are still carried out in the analog domain. However, a new type of all-digital demodulator was recently developed, as a part of this work, which fully incorporates the analog front-end circuitry following the Transimpedance Amplifier (TIA) into the digital domain, allowing for the dynamic range extension approach being presented within this dissertation. Both the analog and the all-digital demodulators are now presented.

2.6.1 Analog Demodulation

Figure 2.6 depicts the architecture of a heterodyne fiber-optic analog demodulator. This is currently the most widely used approach found within the literature [6, 4]. The architecture is known as a synchronous Zero-IF receiver. Some literature refers to this type of demodulator as a homodyne demodulator since it utilizes only a single frequency conversion stage. This should not be confused with PGC homodyne demodulation. Likewise, receivers which use multiple conversion stages are often referred to as heterodyne. It should be noted that the heterodyne component of the interferometers refers to the difference in modulated carrier frequency components between the signal and the reference arm, not the number of conversion

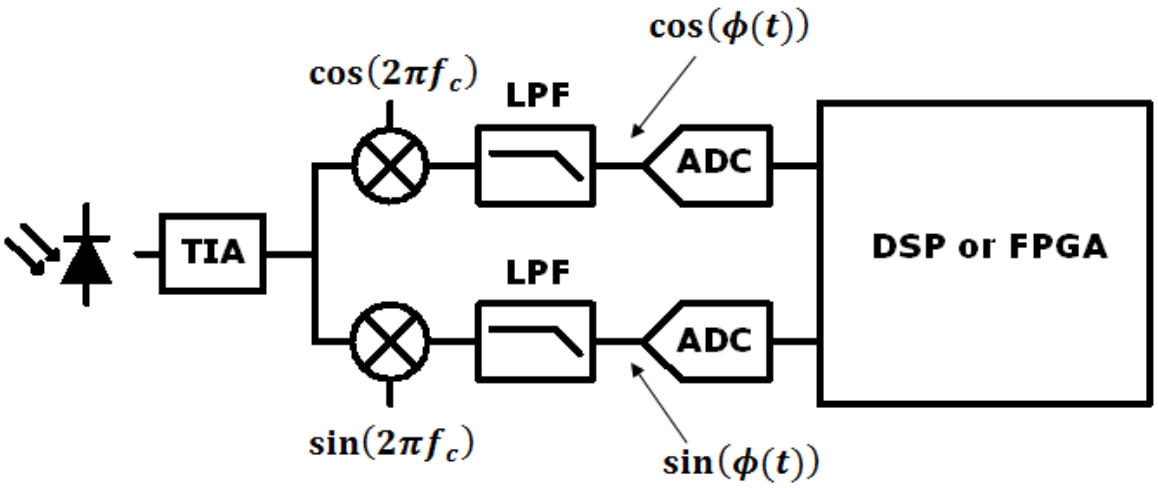

Figure 2.6: Analog heterodyne demodulation

stages in the receiver.

One reason heterodyne modulation has become popular for fiber-optic sensors is because of the relatively low processing overhead required for demodulation. The incoming optical signal is first converted to an output current, which is then converted to a usable voltage by the TIA. Most actual demodulators will likely contain some additional gain, attenuation, or filtering stages, however, for simplification these have been omitted. The voltage output of the TIA is then fed to two analog mixers. These mixers are driven by what are known as the in-phase (I) and quadrature (Q) components of f_c, one at $\cos(2\pi f_c)$ and the other at $\sin(2\pi f_c)$. Frequency mixing of the incoming heterodyne carrier at f_c with the I/Q components is performed in order to down convert it to baseband where it can be processed. However, in the down-conversion process an additional high frequency term is generated at $2f_c$. This high frequency signal must be removed and is, therefore, passed through a low-pass filter. After the low-pass filters, the signals are digitized by two Analog to Digital Converters (ADCs). At the input to one ADC now exists $\cos(\phi_s(t))$, at the other $\sin(\phi_s(t))$.

Extracting the phase signal of interest $\phi_s(t)$ from the cosine and sine can be accomplished in a number of ways [4]. The most popular method is the use of a four-quadrant arctangent calculation where

$$\phi_s(t) = \arctan(\frac{\sin(\phi_s(t))}{\cos(\phi_s(t))}) \tag{2.6}$$

Calculating the arctangent is usually one of the most computationally intensive aspects of demodulation. Various techniques exist, each with their own tradeoffs in performance and computational requirements. Several different approaches will be discussed in the following section.

Analog demodulation suffers from several drawbacks. Small differences in the I/Q processing paths can lead to noise in the demodulated output. Noise can arise from such issues as DC offsets in the various stages and small phase differences in the transfer function of the low-pass filters. Calibration of the analog circuitry is required to minimize the impact of such effects. This can add significant cost and complexity to the demodulator design. One way to mitigate these issues is to move the analog front-end circuitry into the digital domain.

2.6.2 Digital Demodulation

Digital demodulation resolves many of the problems typically encountered with analog demodulators. By moving the synchronous front-end analog circuitry into the digital domain, differences between the I/Q paths are eliminated and, therefore, less noise is produced in the output. An all-digital approach also simplifies the hardware by eliminating much of the required analog front-end and calibration circuitry.

Figure 2.7 depicts the basic all-digital demodulation architecture. The digitization now occurs directly after the TIA, although in most practical systems some additional gain and filtering stages may be inserted between. The analog mixers have been replaced with digital multipliers, while the analog low-pass filters have been replaced with Finite Impulse Response (FIR) filters. The FIR filters can be simple rectangular averaging filters or more advanced implementations depending on the available input data and the system requirements for high frequency noise suppression.

Since the arctangent processing is one of the most computationally intensive parts of the

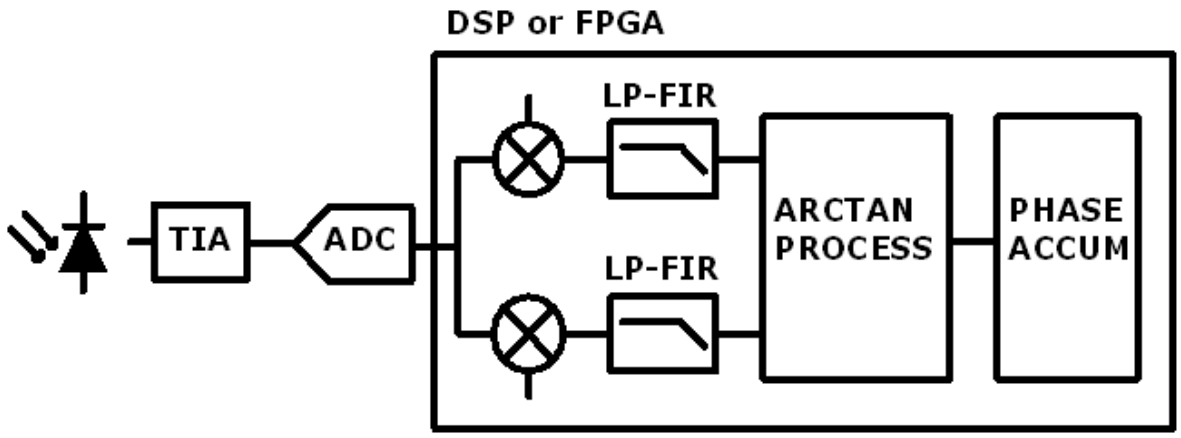

Figure 2.7: Digital heterodyne demodulation

digital demodulation process it must be carefully considered during the design stage. Numerous approaches exist for arctangent calculation. Three common approaches to arctangent computation are the CORDIC algorithm, look-up tables, and Taylor series approximations. The amount of processing time required by each is a direct function of the input value and the required output accuracy. Most implementations will require an output which is accurate to approximately 1 μrad so as to not introduce an additional source of error. The input value z will have the largest impact on the amount of required processing.

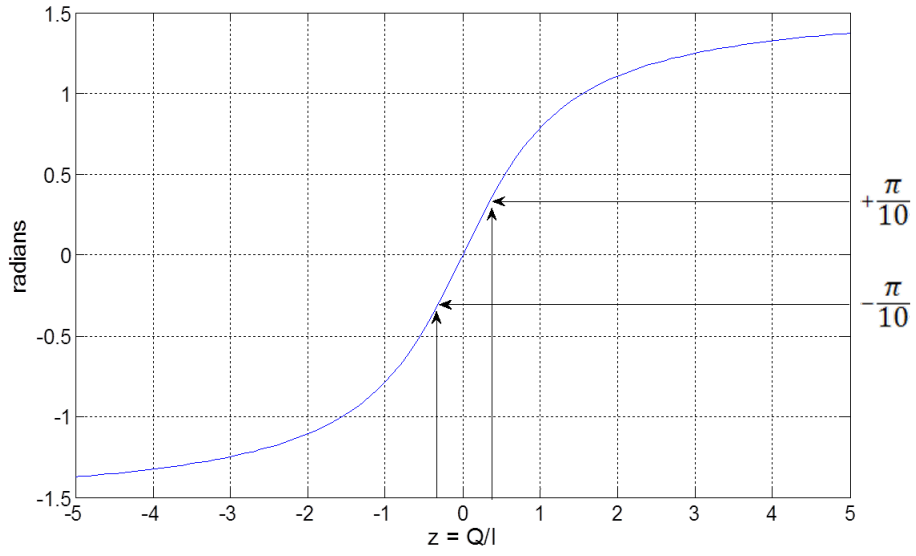

Figure 2.8: Arctangent output curve

Figure 2.8 shows the output curve for the arctangent function. For input values of z between ± 0.3, the output will be in the range of $\pm\frac{\pi}{10}$. It can be seen in the figure that within this range the arctangent output is nearly linear. The further away from this region, the more the output becomes non-linear. Regardless of the computational approach, arctangent calculations within the linear section of the function will require far less processing than those outside. For example, an arctangent calculation using a Taylor series approximation can be defined as

$$\arctan(z) = z - \frac{z^3}{3} + \frac{z^5}{5} - \frac{z^7}{7} + \ldots \tag{2.7}$$

If the input value z to the arctangent function is .3, then only the first three terms of the Taylor series are sufficient to meet the 1 μrad error requirement. However, if z lies only slightly in the non-linear part of the curve, at a value of .99, then as many 350 terms are required. As this example shows, it is highly desirable to limit the arctangent processing to the linear portion of the curve. One arctangent calculation is required for each demodulation point. This may be as many as 1-2 million per second. Such processing requirements can pose a problem if not handled properly.

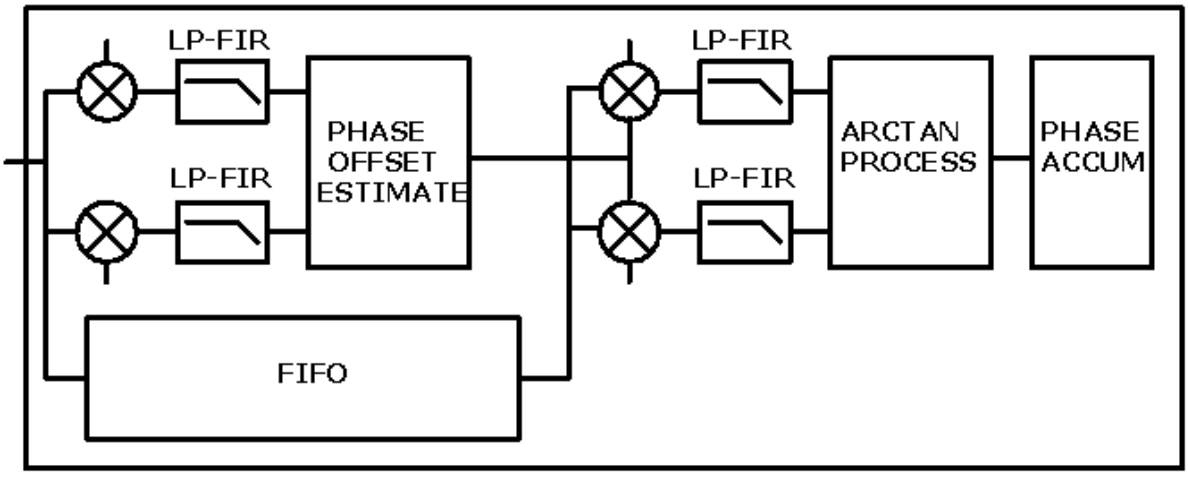

Figure 2.9: IQ reprocessing heterodyne demodulation

One advancement in the all-digital demodulation approach, developed as part of this work, is known as I/Q reprocessing. The purpose of the I/Q reprocessing is to significantly reduce the

arctangent computational load by ensuring that all calculations be carried out in the linear part of the curve. The I/Q reprocessing architecture is shown in Figure 2.9. This architecture breaks down the demodulation process into two specific stages. The first stage is used to determine an approximate phase offset with regards to the free-running I/Q clocks. While this is being calculated, the incoming data is being stored in a FIFO memory for later processing. Once the phase offset estimate has been determined, the digital multipliers of the second stage are phase adjusted such that they are nearly in phase with the data contained in the FIFO, thus ensuring that the magnitude of the z value passed to the arctangent processing circuitry is always less than .3. The amount to which the multipliers were phase shifted is then added back in to the final arctangent output. Using this technique, the arctangent computational requirements can be met with a simple three term Taylor series calculation. Although the I/Q reprocessing requires two stages and some additional hardware resources, the overall computational simplification is significant. This is the approach taken in the digital demodulator used in the experimental research portion of this dissertation.

Lastly, the all-digital demodulation approach has one very important advantage. In an analog demodulation approach the frequency mixing is conducted prior to digitization. Thus, no information about the received heterodyne carrier is available in the digital domain. In an all-digital demodulator the heterodyne carrier is sampled directly, and any information contained in it is therefore available for processing. Information such as the carrier's amplitude, frequency, and even noise content are all valuable. For this research, however, the most important piece of information that is obtained is the instantaneous frequency of the carrier, which will provide the dynamic range increases presented in this dissertation. Such a technique would not be easily achievable in an analog demodulation approach.

Chapter 3 Dynamic Range Limitations

Chapter 3 examines dynamic range issues encountered with fiber-optic sensors. Methods for determining both the upper and lower bounds on the dynamic range of fiber-optic interferometers are evaluated. A literature review is then provided which explores approaches for extending the dynamic range found within the literature.

3.1 Fiber-Optic Interferometer Dynamic Range

The dynamic range of a heterodyne fiber-optic interferometer is defined as the difference between the smallest and largest phase change that can be measured. Dynamic range requirements vary widely by application. However, many papers found in the literature state that the sensors should have a minimum dynamic range of 120 dB [3]. Most papers written on fiber-optic interferometers demonstrate dynamic range levels that achieve this mark. Yet, for some applications, as much as 160 dB or more is required to fully meet system specifications. Achieving this level of dynamic range is a non-trivial task even after optimizing all available design parameters.

Fiber-optic interferometric coils themselves have very large dynamic ranges. A 100 m fiber-optic coil constructed of 80 μm bend insensitive fiber has been shown to have a strain-induced failure limit of over 240 dB [3]. Therefore, the sensor is not a limiting factor. Rather, the limitations are factors of the system used to interrogate the sensor. Such issues will be presented later in the chapter.

One paper touted a fiber-optic system as having a dynamic range of 177 dB at 1 Hz [6]. Specifying dynamic range at a given frequency is required since fiber-optic sensors are said to be bandwidth limited. This topic will be explored in depth in the following section; however, it should be noted that with fiber-optic interferometers, the maximum dynamic range decreases with frequency at a rate equal to 20 dB per decade for sinusoidal modulation. Therefore, the system with a reported 177 dB dynamic range at 1 Hz only achieves a 110 dB dynamic range at 10 kHz. As a result, the dynamic range specifications of fiber-optic sensors

must always be accompanied by bandwidth requirements for proper evaluation.

Another common misconception about fiber-optic interferometer dynamic range is that it can be compared to electronic-based system dynamic range. With traditional electronic-based sensor systems, the dynamic range can be increased or decreased with additional gain and/or attenuation stages. No such comparable approach exists with fiber-optic sensors. Before the dynamic range extension techniques described within this dissertation were available, only a few options existed. First, reduce the system noise floor. This increases the minimum resolvable signal and allows for a less responsive sensor to be used. The second method is to increase the maximum sample rate of the system and extend the high-end limitation. A third option, which was only recently published in the literature, is known as derivative pulse interrogation [8]. Derivative pulse interrogation will be discussed in the literature review. This dissertation now examines the low-end system noise floor limitations, the high-end bandwidth limitations, and the available dynamic range extension techniques found in the literature, such as derivative pulse interrogation.

3.2 Low-End Limitations

Dynamic range increases can be achieved by reductions in the system noise floor. This section introduces the numerous noise sources present in a fiber-optic interferometric system that contribute to the overall noise floor and determine the minimum achievable phase resolution.

3.2.1 Laser Phase Noise

Laser phase noise is generated from frequency noise of the laser being converted to a phase through an optical length path mismatch between the signal and the reference arms. The magnitude of the laser phase noise $\delta\phi_{laser\_phase}$ can be determined from 3.1

$$\delta\phi_{laser\_phase} = \frac{2\pi n_{eff}(L_s - L_r)\delta\nu}{c} \tag{3.1}$$

Most laser manufacturers will provide phase noise specifications with a standard 1 m path differential. However, in many interferometer applications it is possible to achieve a less than 1 m differential and reduce the overall contribution of laser phase noise. Static strains must also be considered when path matching as they will impose changes in n_{eff} that will be indistinguishable from changes in the path length.

Recent advances in laser technology have significantly reduced the impact from laser phase noise. High coherence lasers are now commercially available with frequency linewidths less than 1 kHz [9]. The phase noise contributions from such lasers are below 1 μrad/$\sqrt{\text{Hz}}$ for frequencies above 100 Hz.

3.2.2 Laser RIN

Relative Intensity Noise (RIN) is the result of small fluctuations in the output power of the laser. Its spectrum shows up as sidebands around the carrier, which appears as phase noise in the measurement band after demodulation. Laser manufacturers provide RIN spectrum levels in units of dB/Hz. The phase noise contribution from RIN can be determined from 3.2, where RIN is the spectral levels provided by the manufacturer.

$$\delta\phi_{laser\_rin} = 10^{\frac{\sqrt{RIN(f)}}{20}} \tag{3.2}$$

For RIN levels less than -130 dB, the phase noise contributions will be less than 1 μrad/$\sqrt{\text{Hz}}$. As with laser phase noise, recent advances in laser technology have made RIN levels sufficiently small. Typical RIN levels are now under -130 dB/Hz for frequencies above 100 Hz [9].

3.2.3 Oscillator Phase Noise

Fiber-optic interferometric systems use a single master oscillator to drive both the modulation of the AOMs and the synchronous demodulation electronics. Use of more than one oscillator

within the system would generate significant phase noise as even highly stable oscillators will drift relative to each other. But, phase noise of the single oscillator will still be present in the demodulated output spectrum. Oscillator phase noise is provided by the manufacturer in much the same way as RIN. The units are provided in dBc/Hz. Ultra-low phase noise oscillators can now be purchased with phase noise levels of less than -140 dBc/Hz above 100 Hz. Such levels contribute sub 1 μrad/$\sqrt{\text{Hz}}$ noise and can generally be ignored.

3.2.4 Fiber Thermal Noise

Fiber-thermal noise is an inherent property of the fiber itself, originating from small fluctuations in n_{eff} as a result of small variations in temperature [10]. The magnitude of the fiber thermal noise is dependent on numerous parameters. However, a generalized approximation has been developed based solely on the length of the fiber [4].

$$\delta\phi_{fiber\_th} = 10^{\frac{\sqrt{-147+\log(L_s)}}{20}} \tag{3.3}$$

The approximation assumes that the noise is purely white. However, there is substantial role-off above 10 kHz in actual systems. This can typically be ignored since other sources of noise will dominate above 10 kHz.

3.2.5 Transimpedance Amplifier (TIA) Thermal Noise

TIA thermal noise is associated with electronic noise from the photodetector's transimpedance amplifier. If a sufficiently quiet amplifier circuit is used, then the primary source of thermal noise will be generated by the TIA load resistor [4].

$$\delta\phi_{tia\_th} = \frac{\sqrt{4kT_e/R_l}}{rP} \tag{3.4}$$

The minimum detectable phase shift as a result of TIA thermal noise can be found from

equation 3.4. T_e is the equivalent thermal temperature, k is Boltzmann's constant, and R_l is the TIA load resistance. For TIA circuits using load resistors 100k ohms or greater, the contribution from TIA thermal noise will be below 1 μrad/$\sqrt{\text{Hz}}$ for $P > 1\,\mu$W.

3.2.6 Optical Shot Noise

Optical shot noise is generated as a result of fluctuations in the average number of the photons hitting the detector. Equation 3.5 can be used to determine the minimum detectable phase shift based on the average amount of light received at the photodetector, where q is the electron charge [6].

$$\delta\phi_{i\_shot} = \frac{\sqrt{2qrP}}{rP} \tag{3.5}$$

It can be seen from this equation that as the received optical power is increased, the minimum detectable phase shift improves. However, most practical systems which incorporate Erbium Doped Fiber Amplifiers (EDFAs) will not be limited by shot noise.

3.2.7 EDFA Spontaneous-Spontaneous Noise

Erbium doped fiber amplifiers are widely used within large fiber-optic interferometric sensor systems. EDFAs allow for optical amplification without the need to convert the signals to the electrical domain and back. Although many different optical amplifier technologies have been developed, the EDFA is still the preferred choice for interferometric systems. They provide high levels of gain, low noise figures, and suffer little from non-linear optical effects. EDFAs are used within fiber sensor systems as transmitter power boosters, mid-range extenders, and receiver pre-amplifiers. The EDFA noise considerations presented in the following two sections relate to EDFAs as pre-amplifiers to the receiving photodetectors. Such amplifiers are common in large TDM and Dense Wavelength Division Multiplexing (DWDM) systems.

Several different sources of noise are introduced to the system with the use of EDFAs. The

two most dominant sources are known as spontaneous-spontaneous and signal-spontaneous. EDFAs generate low levels of amplified light known as Amplified Spontaneous Emission (ASE) across the gain spectrum of the device. This ASE can then mix with itself on the receiving photodiode. This is known as spontaneous-spontaneous noise. Its phase noise contribution can be determined from equation 3.6, where h is Planck's constant, F is the noise figure of the amplifier, v_{opt} is the frequency bandwidth of an ASE limiting filter, and D is the duty cycle of the received optical pulses into the EDFA [6].

$$\delta\phi_{sp\_sp} = \frac{hvF\sqrt{v_{opt}}}{VPD} \tag{3.6}$$

For a DWDM system, v_{opt} will commonly be set at the channel bandwidth of 100 GHz. D is dependent on the number of TDM multiplexed channels. For TDM systems with a large number of channels, D will be small, and the contribution from spontaneous-spontaneous noise will be significant. Even for non-TDM systems, use of an EDFA pre-amplifier will introduce enough noise to be one of the primary limiting factors.

3.2.8 EDFA Signal-Spontaneous Noise

A second noise term generated by the use of an EDFA pre-amplifier is known as signal-spontaneous. This develops from beating of the incoming optical signal with the ASE [6].

$$\delta\phi_{sig\_sp} = \frac{\sqrt{2Fhv}}{V^2PD} \tag{3.7}$$

The level of this phase noise can be determined from equation 3.7. In general, spontaneous-spontaneous noise will dominate; however, if the polarization visibility V is small, then its impact must be considered as well.

3.2.9 Double Rayleigh Scattering

Photons encountering imperfections in the fiber itself can cause what is known as Rayleigh scattering, in which the light can scatter in any direction. However, light scattered in the reverse direction can create problems. If the reverse scattered light undergoes a second reverse reflection, the light will then be traveling in the original direction but out of phase with the incident wave. If a long coherence wavelength laser is used, and the fiber lengths between the source and receiver are more than a few kilometers, the double Rayleigh scattered noise contribution can be significant [4]. Quantifying the magnitude of this noise is difficult as it is highly system-architecture dependent. Also, although not truly Rayleigh scattering, discrete reflections from system components, fiber connectors, and fiber-splices complicate the calculation. Double Rayleigh scattering effects can be reduced by the use of separate input and output fiber leads from the optical pulse generator to the sensor and back to the receiver. The insertion of directional optical isolators along the fiber leads can also reduce the impact of scattering noise.

3.2.10 Finite Extinction Ratio

The modulation devices used to generate the optical interrogation pulses are generally treated as perfect on/off switches. In reality, they suppress only a portion of the light. The ratio at which the light is allowed to pass in the on state to the amount which is blocked in the off state is known as the extinction ratio. Light which is allowed to pass during the off state creates unintended continuous interferometers. Like Rayleigh scattering effects, determining the impact of finite extinction noise is difficult. Experimental results have shown that finite extinction ratios between 60 dB and 100 dB are required to minimize any noise [6]. Such extinction levels require specialized devices or cascading of multiple units.

3.2.11 Polarization Fading and Noise

Light in the signal and reference paths can become polarized as it travels down the fiber. If the angle of the polarization states between the two paths becomes orthogonal, then mixing will not take place on the photodetector. When this occurs, the Carrier to Noise Ratio (CNR) is reduced, and the signal of interest will be unrecoverable. This is known as polarization signal fading, the magnitude of which depends on the angle of polarization between the two arms. This has been one of the most challenging aspects of fiber-optic interferometry. It has also been one of the most heavily researched. Numerous approaches have been developed for reducing the severity of polarization fading. These include polarization diversity receivers, polarization switching, and Faraday rotator mirrors. Of them, Faraday mirrors are the simplest to implement and provide nearly complete polarization fading mitigation [11]. Their cost, however, has largely prohibited their use in the past. Though, their prices have dropped in recent years to the point that their benefits now outweigh the costs in many applications. For systems utilizing Faraday mirrors, this report will assume that the polarization visibility will be maximized at $V = 1$.

In addition to polarization signal fading, polarization noise can also be introduced into the system. Polarization changes generate amplitude modulations of the received carrier signal. These amplitude modulations will show up as sidebands in the output spectrum. The same techniques which are used to mitigate polarization fading also mitigate polarization noise. Again, Faraday rotator mirrors are a near ideal solution since they eliminate polarization fluctuations [4]. The effects of polarization fading and polarization noise will not be included in the total noise analysis because they can largely be eliminated with the use of Faraday mirrors.

3.2.12 Total Phase Noise

The lower limit of the dynamic range is determined by the system's total phase noise floor. This can be found by taking the square root of the sum of the squares of the individual noise sources, since they are considered to be statistically uncorrelated [6].

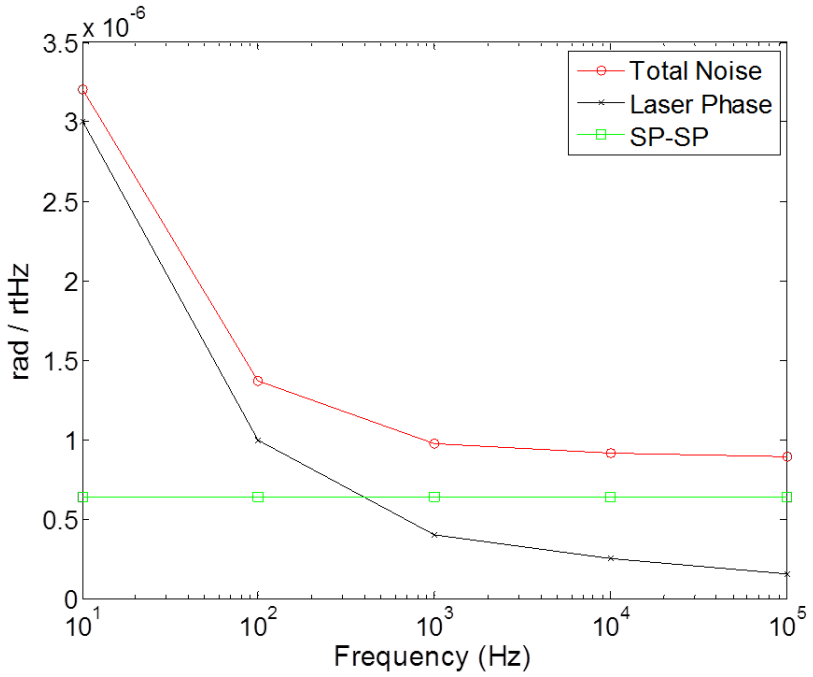

Figure 3.1: Phase noise with EDFA

$$\delta\phi_{total} = \sqrt{\delta\phi^2_{total}} \tag{3.8}$$

$$\delta\phi^2_{total} = \delta\phi^2_{laser\_phase} + \delta\phi^2_{laser\_rin} + \delta\phi^2_{osc} + \delta\phi^2_{fiber\_th} + \delta\phi^2_{tia\_th} + \delta\phi^2_{i\_shot} + \delta\phi^2_{sp\_sp} + \delta\phi^2_{sig\_sp} \tag{3.9}$$

Which source or sources of phase noise contribute most to the system noise floor is dependent on a wide variety of factors, but can be separated into two cases: systems using an EDFA preamplifier and those which do not. Phase noise plots are provided for the two cases in Figure 3.1 and 3.2. The system parameters used in the generation of these plots are as follows: $L_s = 100$ m, $r = .9$ A/W, $P = 10u$W, $T_e = 600°$K, $R_l = 128$ kΩ, $V = 1$, $F = 2.5$, $\nu_{opt} = 100$ GHz, and $D = .5$. Values for laser phase noise, laser RIN, and oscillator phase noise were taken from manufacturer datasheets.

For systems where the optical power is sufficiently low at the input to the demodulator, it may be desirable to boost the input power using a preamplifier. Using a preamplifier will

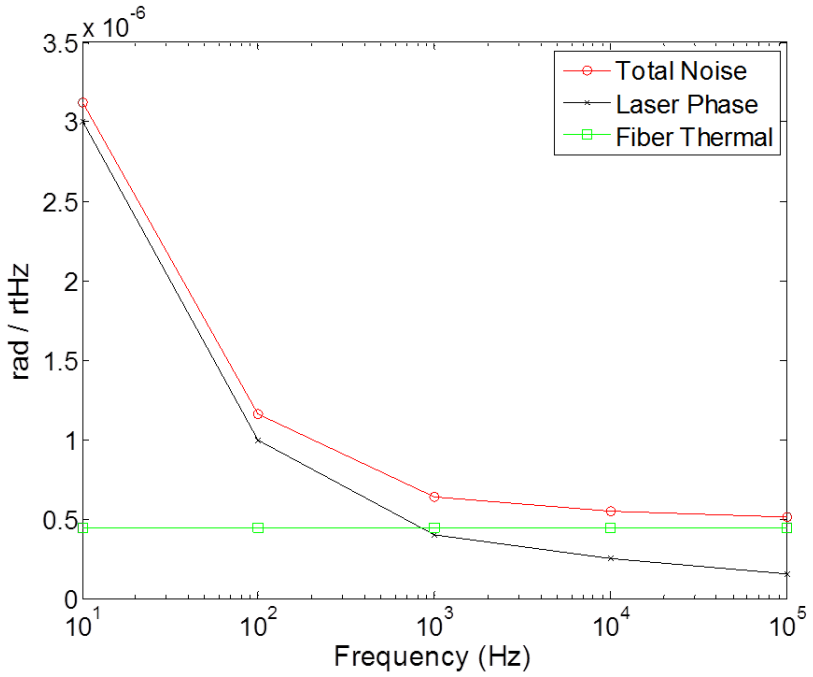

Figure 3.2: Phase noise without EDFA

increase the CNR, but will introduce spontaneous-spontaneous and signal-spontaneous noise. This noise will dominate all other sources above several hundred hertz as seen in Figure 3.1. It should be noted that parameters used in Figure 3.1 are a best case scenario since only a single sensor with perfect polarization visibility is used. In most systems using EDFAs this will not be the case, and high levels of spontaneous generated noise will dominate the entire frequency band, severely limiting the low-end noise floor.

Optical preamplifiers are not required if the input power to the demodulator is approximately -30 dBm or more. In this scenario, and assuming that optimal system components are being utilized, the noise floor will be determined by either the laser phase noise or fiber thermal noise. Figure 3.2 shows the floor when using a 1 kHz linewidth laser, a 1 m path difference, and a 100 m sensing coil. For this scenario, it can be seen that laser phase noise will dominate below 1 kHz, and fiber thermal noise will dominate above. If, however, the linewidth of the laser were reduced or the path differential minimized, the fiber thermal noise would dominate a greater region of the spectrum. Likewise, if the sensor fiber length L_s were reduced, the contribution from thermal noise would be less, and laser phase noise would dominate.

In general, the other sources of noise discussed earlier will be lower than the laser phase noise or fiber thermal noise. However, their magnitudes are all in the range of .1 μrad/$\sqrt{\text{Hz}}$ and .5 μrad/$\sqrt{\text{Hz}}$. The total impact of these different noise sources establishes a limit just below 1 μrad/$\sqrt{\text{Hz}}$ that is difficult, at best, to improve upon. In reality, other sources of noise, which are more difficult to quantify, may dominate. This includes finite extinction ratio noise, double Rayleigh scattering, and polarization effects. Increasing the high-end dynamic range limitation is a more feasible approach for any significant dynamic range increases.

3.3 High-End Limitations

The high-end limitation of a fiber-optic interferometer's dynamic range is based solely on the interrogation sample rate f_{samp}. Each pulse of light used to interrogate the sensor results in a single phase measurement. Since the demodulation process used in this work uses an arctangent calculation to extract the phase information of interest from each pulse, the most that the phase can change in either direction is limited to $\pm\pi$. The maximum rate of phase change is therefore determined by equation 3.10.

$$\theta_{demod} = \pm\pi f_{samp} \tag{3.10}$$

θ_{demod} is often referred to in the literature as the fringe rate of the demodulator. This is the maximum rate of phase change generated by the sensor for which the demodulator can accurately recover the signal. If a signal generates a phase change greater than this limit, then the demodulator output will be invalid. This is known as an "excession" of the demodulator [4]. Determining the fringe rate of the signal θ_{sig} is often the challenging part. This is the focus of Chapter 4. However, for sinusoidal modulation, it will be shown that the signal fringe rate will be equal to the frequency of the sinusoid times its amplitude. Using this information, it can be shown that the maximum sinusoidal amplitude A_s that can be measured at a particular frequency is determined by equation 3.11.

$$A_s = \frac{f_{samp}}{2f_s} \tag{3.11}$$

From equation 3.11, it can be seen that for a given frequency of f_s the only option for increasing A_s is to increase f_{samp}. However, the maximum sampling rate f_{samp} is determined by numerous factors. The most critical of these are the sensor coil length L_s, the number of TDM channels, the rise/fall times of the pulsing unit, and the ability of the demodulation hardware to process the incoming data. Assuming no TDM is utilized and given the pulse width requirements of 400-500 ns for the demodulation hardware used in this research, f_{samp} is limited to around 1 MHz. Assuming $f_{samp} = 1$ MHz, the frequency dependent maximum values of A_s can be determined. These values can be used as the high-end dynamic range limitation for sinusoidal modulation. Different modulating waveforms will have different dynamic range limitations.

3.4 Dynamic Range Determination

The overall system dynamic range is determined from the difference in the maximum and minimum resolvable phase signal. The maximum signal was determined as A_s. The minimum was found to be ϕ_{total}. Plotting the logarithmic values of each, and taking the difference between the upper and lower limits, results in the dynamic range of Figure 3.3, labeled as "DR".

The calculated dynamic range of Figure 3.3 is valid only for single sinusoidal modulation and the system parameters defined earlier in the chapter. These dynamic range values should also be considered best case. Environmental conditions such as acoustic noise, vibrations, and thermal fluctuations can dominate the lower phase noise limit and reduce the actual measurable dynamic range.

Obtaining dynamic range levels above those presented in the section is difficult with present technology. A few dB increase may be possible on either the high or the low side with further optimizations. For systems which require dynamic range levels well above those presented

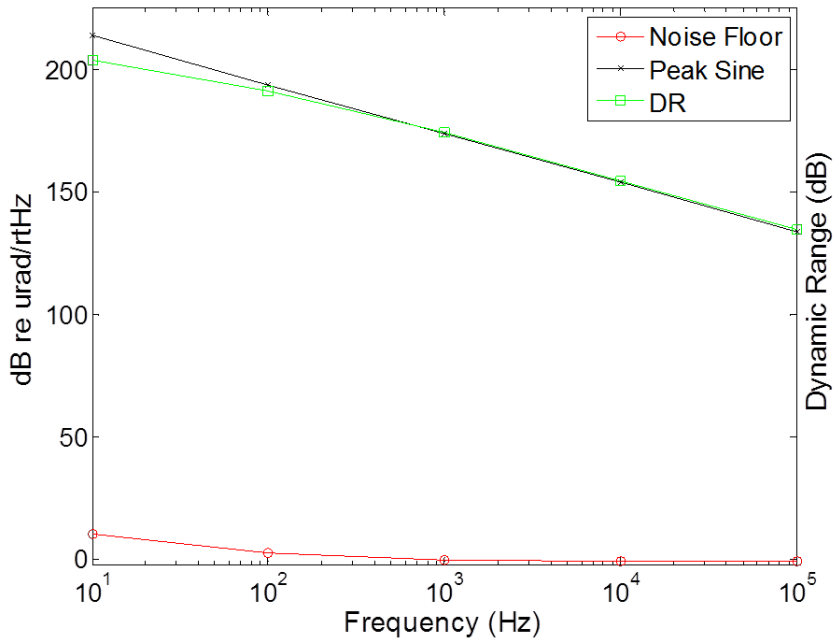

Figure 3.3: Calculated dynamic range with an EDFA

within, only one other viable technique has been presented for substantial dynamic range extension prior to this work. The following section examines previous attempts at dynamic range extension and approaches used in similar applications.

3.5 Dynamic Range Extension Literature Review

Little research is found in the literature covering fiber-optic interferometric dynamic range extension. Numerous papers have demonstrated how to calculate the available dynamic range, however, most fail to mention the limitations or provide any extension techniques. Most of the available literature in the area of fiber-optic interferometric systems has focused on the development of large TDM systems. Such systems are comprised of hundreds of channels multiplexed in both time and wavelength [7, 6, 4]. Unfortunately, TDM reduces f_{samp} for each additional sensor multiplexed. Thus, the dynamic range of such systems is significantly reduced. This reduced dynamic range impacts the type of applications where these large arrays can be utilized. Even systems which do not utilize any TDM, and for which the other system parameters are optimized, the maximum dynamic range may be insufficient.

One recently published approach to dynamic range extension is known as derivative pulse interrogation [8]. Prior to the method presented in this dissertation, derivative pulse interrogation was the only viable extension technique. Details of this method are provided in the following section. The other methods documented below are largely considered impractical for large sensor systems. Their practicality is limited to single sensor systems for lab applications. Several other papers have been written in recent years which explore the dynamic range differences between PGC homodyne and heterodyne modulation and how to optimize them [12, 5]. Such work does not actually provide for any range extensions beyond what has previously been reported. The following sections discuss different methods found in the literature for dynamic range extension.

3.5.1 Derivative Pulse Interrogation

Derivative pulse interrogation was the only viable dynamic range extension approach prior to this work [8]. However, it was only recently published, being released after the completion of most of this dissertation. According to the paper, it was derived from work presented in a much older paper using Bessel function tracking for dynamic range extension [13]. It should also be noted that the work presented in the recent paper was focused on phase noise sensitivity measurements, not dynamic range extension. The derivative pulse interrogation method was used in the paper to improve the lower phase noise limit, not extend the upper range. It did, however, mention the use of derivative pulse interrogation for high-end dynamic range extension, but provided only a few details. As such, the specifics regarding this approach are not well understood.

The derivative pulse interrogation method works by generating additional pulses in the received pulse stream which are lower in sensitivity than the standard pulses by a substantial amount. This is accomplished by reducing the pulse widths used to interrogate the sensors and adding an additional compensator stage at the receiver to generate the derivative pulses. Standard pulses are formed by overlapping two pulses that hit two different mirrors at the same time. Derivative pulses are generated by overlapping two different pulses on the same mirror at two different times. Since the derivative pulses interrogate the same mirror at two

different times, the pulse that is generated can be considered a phase derivative. Derivative pulses taken from both mirrors of a sensor are subtracted in order to obtain the reduced sensitivity phase measurement. This reduced sensitivity is documented to be as much as 78 dB less at 100 Hz but increase by 6 dB per octave. The details behind these numbers were not presented in the paper, neither were the specifics of how the reduced sensitivity measurements should be used to increase the dynamic range. However, this is currently the only other documented source which discusses a viable technique for overcoming the $\pm\pi$ limitations in a pulsed heterodyne fiber-optic interferometric system.

Although few details have yet to be provided regarding derivative pulse interrogation, several drawbacks are evident. First, twice the number of optical interrogation pulses are required, thus reducing the maximum achievable f_{samp}. Therefore, to obtain an overall increase in dynamic range requires an initial reduction. Also, the additional compensation coil required at the receiver is a potential problem. Besides the requirement of additional hardware, the extra compensator coil introduces a path imbalance which increases the laser phase noise. The derivative interrogation method can reportedly subtract out the added laser phase noise, but the coil itself can be another source for picking up environmental noise. No additional compensation coils or hardware are required for the dynamic range extension approach presented in this dissertation.

3.5.2 Predictive Phase Algorithms

One paper identifies the potential dynamic range limitations and discusses an extension approach explored by the researchers. This was an overview paper of high performance fiber-optic sensing [4]. However, the dynamic range extension technique briefly mentioned in this paper was found to not be viable by the researchers. The approach was to use predictive waveform tracking algorithms for predetermined signals. They found that this method was only viable in a few select situations. The details provided in the article were largely omitted since they determined it to be of little value and not relevant to the larger paper.

3.5.3 Multi-wavelength Interrogation

Multi-wavelength interrogation approaches are common in the literature. Their popularity arise from the fact that they feature unambiguous absolute phase resolution. This allows for interferometric measurements down to DC in some applications [14]. They are also touted as having wider dynamic ranges. Multi-wavelength interrogation approaches generate beat frequencies with wavelengths longer than the frequencies of the individual lasers, leading to a larger dynamic range. Despite this advantage, the dynamic ranges of multi-wavelength techniques are relatively small. A dynamic range of 93 dB was reported in one paper using two wavelengths [15]. For a four wavelength system, a 152 dB dynamic range was achieved [16]. More than 160 dB is estimated for a five wavelength system [17].

Despite the interest in multi-wavelength interrogation approaches, they are not without issue. The use of multiple lasers and additional interrogation hardware makes them less than ideal for large multiplexed systems. The multi-wavelength approaches demonstrated to date are also passively interrogated and subject to interferometric signal fading. Lastly, the resolution and the ability of multi-wavelength systems to achieve wide dynamic ranges are dependent on the coherence of the lasers. For interferometric systems interrogated remotely over more than a few miles, the laser coherence requirements become quite challenging. As a result of these issues, multi-wavelength interrogation approaches are not well suited for large scale remotely interrogated fiber-optic interferometric systems.

3.5.4 Phase-Polarization Measurement

One of the earliest attempts at dynamic range extension was the combined use of interferometric and polarization measurements on the same sensor [18]. The interferometric sensing provides the high resolutions needed while the polarization sensing, being much less sensitive, provides a large unambiguous measurement range. Researchers were able to successfully implement this approach in the lab using bulk optics. However, practical fiber-optic sensors based on this approach would be much more challenging. Remotely interrogated sensor systems which utilize EDFAs, mux/demux units, optical circulators, and

Single-Mode Fiber (SMF) complicate polarization measurements. Additionally, most large interferometric sensor systems require some form of polarization signal fading mitigation to stabilize the phase measurement, which would prevent any potential implementation of this type of dynamic range extension.

3.5.5 Summary

Both the high and low-end dynamic range limitations were presented in this chapter. The low-end was shown to be limited by numerous sources at the 1 μrad/$\sqrt{\text{Hz}}$ noise level. The high-end was shown to be bandwidth limited. Little dynamic range improvement can be achieved on either end with current technology. A literature review also showed few viable options. The details of the most promising option, derivative pulse interrogation, have not yet been fully published.

It was stated previously that the available dynamic range is dependent on the fringe rate of the modulating waveform itself. This dissertation now provides a fringe rate analysis for several different waveform types.

Chapter 4 Signal Fringe Rate Analysis

It was shown in Chapter 3 that the fringe rate of the demodulator must always be greater than the fringe rate of the measured signal. A violation of this requirement will result in an error in the recovered signal. Determining the fringe rate of the demodulator is straight forward since it is based entirely on the sample rate f_{samp}. Determining the fringe rate of the signal can be much more challenging. However, knowing the fringe rate of the expected received signals is critical in accurately determining the high-end dynamic range limitations.

Several papers have previously demonstrated fringe rate analysis of single-tone sinusoidal modulation [3, 6, 4]. Little work has been found which addresses more complicated waveforms. Of particular interest is fringe rate determination of broadband noise and its dynamic range reduction factor. The remainder of the chapter explores fringe rate analysis on several commonly encountered waveforms including single-tone sinusoidal, multi-tone sinusoidal, and broadband noise. The impact of broadband noise on single-tone sinusoidal modulation is also analyzed.

4.1 Single Sinusoidal Modulation

For a heterodyne interferometer system, it was shown in Chapter 2 that the time varying component of the photodetector current i_{pd_sig} can be determined from equation 4.1. The current is comprised of a continuous carrier signal at f_c which is modulated by the phase of the light in the sensor arm $\phi_s(t)$.

$$i_{pd\_sig}(t) = rPV\cos(2\pi f_c(t) + \phi_s(t)) \tag{4.1}$$

If $\phi_s(t)$ is sinusoidally modulated then it will take the form of equation 4.2.

$$\phi_s(t) = A_s\sin(2\pi f_s(t)) \tag{4.2}$$

The fringe rate of the signal θ_s is determined by taking the derivative of $\phi_s(t)$.

$$\theta_s(t) = 2\pi f_s A_s \cos(2\pi f_s(t)) \tag{4.3}$$

Since the peak fringe rate is typically what is of interest, the above equation can be reduced to equation 4.4 [4].

$$\theta_s = 2\pi f_s A_s \tag{4.4}$$

Equation 4.4 is what was defined as the sinusoidal fringe rate in the previous chapter. As can be seen, it is a function of both the signal's amplitude and frequency. Thus, the maximum amplitude signal A_s that the demodulator can properly recover is dependent on the signal frequency f_s. This gives the high-end dynamic range limitation a 20 dB per decade roll-off. It was also shown previously that since the maximum measurable phase between any two demodulated points is $\pm\pi$, the fringe rate of the demodulator is given by equation 4.5 . Therefore, the maximum sinusoidal amplitude A_s that can be measured is determined by setting equation 4.4 equal to 4.5.

$$\theta_{demod} = \pm\pi f_{samp} \tag{4.5}$$

$$A_s = \frac{f_{samp}}{2f_s} \tag{4.6}$$

Equation 4.6 specifies the maximum measurable sinusoidal amplitude based on the frequency of the signal and the system sample rate. A plot of maximum sinusoidal amplitudes versus system samples rates is shown in Figure 4.1. Three different common f_{samp} rates are provided. A 10 kHz sample rate limit is typical for very large scale TDM multiplexed systems, 100 kHz is an approximate limit for large scale TDM multiplexing, and 1 MHz is typical of a non-TDM multiplexed system. As can be seen in the figure, there is a 40 dB dynamic range

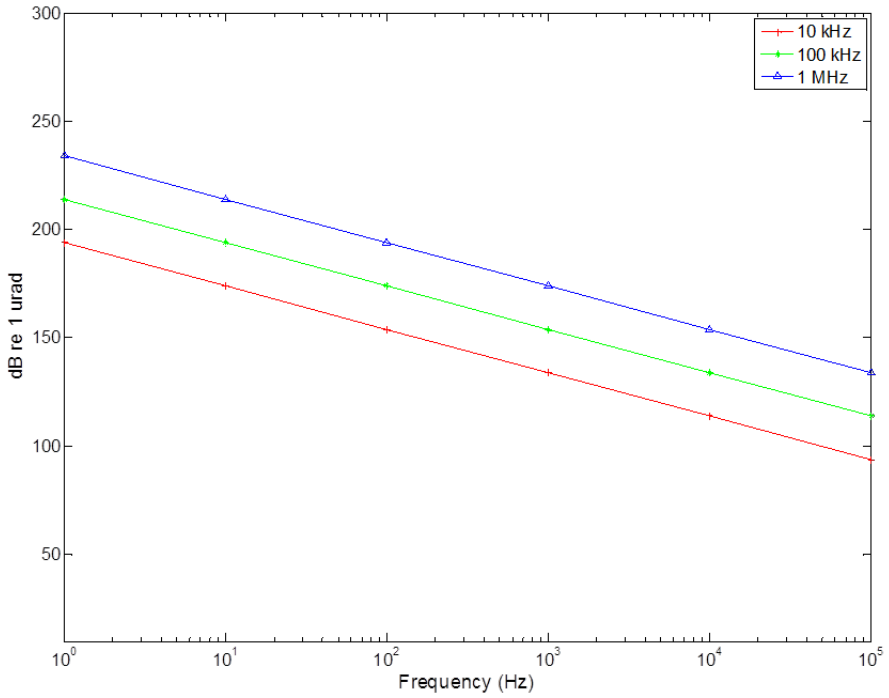

Figure 4.1: Peak sinusoidal fringe rates at different f_{samp} rates

differential between a very large scale TDM multiplexed system and a non-TDM multiplexed system. Such considerations are critical in the initial development stages of a fiber-optic sensor system. Still, this fact has largely been ignored in the existing literature.

4.2 Multi-tone Modulation

Calculating a fiber-optic interferometric system's dynamic range based only on single sinusoidal modulation does not accurately model most real-world situations. For example, multi-tone waveforms are often used in acoustic and vibration testing to reduce the total amount of time needed to collect spectral information. Therefore, it is critical to be able to determine the multi-tone dynamic range in order to properly limit the exciter's drive levels.

If all of the sinusoids in a multi-tone waveform start in phase, then determining the multi-tone

fringe rate is straightforward. All of the individual peak fringe rates will line up in time and add together. For a waveform comprised of m sinusoids, the multi-tone fringe rate value then becomes

$$\theta_m = 2\pi \sum_{n=1}^{m} f_m A_m \tag{4.7}$$

Equation 4.7 can be considered the worst case scenario for multi-tone dynamic range. Use of this value is recommended when the phases of the driving exciters are either unknown or unsynchronized. In the case that the phase alignment between the waveforms is known and can be controlled, some dynamic range improvement can be realized. However, the magnitude of the improvement is generally small and is dependent on a wide range of factors including the number of sinusoids, the frequencies and amplitudes, and the duration of the waveforms. It has been determined through simulations, as part of this work, that dynamic range improvements achieved through phase adjustments is typically only on the order of 1 dB.

The use of multi-tone waveforms will decrease the maximum dynamic range of a fiber-optic interferometer system. For systems which require the absolute highest peak dynamic ranges, the use of multi-tone waveforms should be avoided.

4.3 Broadband Noise

Broadband noise fringe rates have not been addressed previously in the literature. Yet, all systems will be influenced by some level of broadband noise. This noise can be the result of undesired ambient conditions such as background acoustics or from intentional noise generating sources. System noise sources such as those identified in the previous chapter will also introduce a level of broadband noise. Distinguishing system noise from measured noise is usually impossible. Regardless of the source, determination of the broadband fringe rate is critical since it can have an impact on the overall measurable dynamic range. As will be shown later, it will also have an impact on the dynamic range extension approach.

The following broadband noise fringe rate analysis assumes only band-limited white noise. This can be simulated as a series of uniformly distributed random numbers occurring between peak amplitudes $\pm A_n$, at a rate of f_{samp}. Since only the peak fringe rate is of interest, this can be determined as the largest phase shift occurring between any two demodulated data points. This results in the maximum broadband noise fringe rate θ_n of equation 4.8.

$$\theta_n = 2A_n f_{samp} \tag{4.8}$$

Equating 4.5 and 4.8 yields the maximum peak noise level.

$$A_{n\_pk} = \frac{\pi}{2} \tag{4.9}$$

Since A_{n_pk} is a constant, increasing f_{samp} will not result in an increased dynamic range as it did with sinusoidal modulation. However, increasing f_{samp} will still increase the maximum broadband fringe rate θ_n. This is a result of the highest measurable frequency $f_{nyq} = \frac{f_{samp}}{2}$ dominating the fringe rate and setting the limitation on the dynamic range.

The above analysis assumes band-limited white noise with a sharp high frequency roll-off f_h that exists at f_{nyq}. In most practical systems this will not be the case. The location, or the lack thereof, of the high frequency roll-off within the measurement band is critical. If the roll-off occurs at a frequency greater than f_{nyq}, aliasing can create the potential for both noise and demodulator excessions. If the roll-off occurs below f_{nyq}, then it may be possible to increase the peak noise level without overloading the demodulator. Such considerations should be examined for each system. For the ideal case where f_h occurs at or below f_{nyq}, 4.8 can be generalized to determine the maximum fringe rate based on f_h.

$$\theta_n = 4A_n f_h \tag{4.10}$$

For a peak broadband noise of amplitude $A_{n\_pk} = \frac{\pi}{2}$ and a demodulator resolution of 1 $\mu\text{rad}/\sqrt{\text{Hz}}$, the measurable dynamic range is 124 dB. Such high levels of noise do not occur

naturally in most physical systems. Generating these levels of noise can even be a challenge. The real concern with broadband noise is how it can potentially reduce the available dynamic range of other high fringe rate signals.

4.4 Single Sinusoid with Broadband Noise

This section explores the potential impact of broadband noise on high fringe rate sinusoids. As with multiple sinusoids, the peak fringe rates of a single sinusoid and broadband noise (with a high frequency roll-off at f_h) are additive. Thus, the total peak fringe rate for a sinusoid plus noise θ_{s+n} becomes

$$\theta_{s+n} = 2\pi f_s A_s + 4A_n f_h \tag{4.11}$$

It was shown in the last section that the peak measurable noise amplitude is $A_{n\_pk} = \frac{\pi}{2}$. As stated previously, such high levels are not encountered in most system. However, if we assume $A_n = \frac{\pi}{4}$ and $f_h = \frac{f_{samp}}{2}$, and again equate equations 4.5 to 4.11, it can be shown that the maximum amplitude of the sinusoid that can be measured is

$$A_s = \frac{f_{samp}}{4f_s} \tag{4.12}$$

It should be noted that equation 4.12 is only a factor of 2 less than that derived previously for single sinusoidal modulation alone. This shows that, even for large amplitude broadband noise, the reduction in dynamic range available for the sinusoid is minimal. In this example, the amplitude of the noise was reduced by 6 dB from the maximum measurable limit, and the high frequency roll-off occurred at the Nyquist frequency, yet, resulted in only a 6 dB reduction in the sinusoidal dynamic range.

The significance of this analysis is that for most real world applications the impact of even moderate levels of broadband noise can be ignored. What is still to be answered is the

potential impact of the broadband noise on the dynamic range extension technique presented in this paper. This will be addressed in a later chapter.

Chapter 5 Instantaneous Heterodyne Carrier Frequency Measurement

The dynamic range extension approach presented in Chapter 6 requires frequency discrimination of the received heterodyne carrier signal. Consequently, for the dynamic range extension approach to be feasible, a method must first be determined for measuring the instantaneous carrier frequency. This chapter explores potential options based on the system requirements. The first part of the chapter is a literature review. It explores two unique approaches to instantaneous carrier discrimination in the digital domain. However, as will be discussed, only one of the two is well suited for the application at hand. Two additional approaches will also be explored as part of this chapter. The first is based on Discrete Fourier Transform (DFT) analysis. The second is an approach to discriminate frequency via measurement of the amount of expansion or contraction in the carrier signal. Limitations to the different techniques will be addressed.

An understanding of the requirements for frequency discrimination is critical in determining an appropriate measurement approach. It is common in heterodyne modulated interferometric sensor systems for the carrier frequency to have a bandwidth that exceeds 10 MHz. Measurement of this wide of a bandwidth, with a high resolution and accuracy, can be a challenge. Knowing the rate, resolution, and bandwidth with which the carrier must be measured is important. Some of these questions will not be able to be fully addressed until Chapter 6. However, some general rules can be stated. First, an instantaneous carrier frequency measurement must be made for every demodulation point. Second, the entire bandwidth must be measurable, but the resolution requirements are forgiving. Rather than measuring every frequency in the required bandwidth with a high resolution, only select frequencies or frequency bands will actually have to be measured. Lastly, averaging of the frequency measurements between two or more demodulation points is required for the extension approach to work. This averaging further simplifies the need for absolute frequency determination.

5.1 Literature Review

Prior to the start of this dissertation, a literature review was conducted to locate potential methods for measuring the instantaneous carrier frequency that would meet the requirements stated previously. Since Fourier analysis was previously determined to be a suitable candidate, it was not included as part of the literature review. It will be discussed later in the chapter as one of the primary measurement techniques.

Instantaneous frequency measurement is a topic of high interest in the Software Defined Radio (SDR) literature. Software defined radio is a recent area of research that focuses on radio communication systems in which the processing is performed almost entirely in the digital domain. Such research has been facilitated in recent years with the advent of high-speed digital electronics. The potential benefits of SDR include lower-cost hardware, more efficient utilization of the available spectrum, and more flexible communication systems. Because of these benefits, SDR has received substantial research interest in recent years. Discrete frequency discrimination is a topic which has been addressed in numerous SDR papers. Two methods which have been explored include Digital Instantaneous Frequency Measurement (DIFM) and Digital Phase Locked Loops (DPLLs).

5.1.1 Digital Instantaneous Frequency Measurement

The ability to quickly discriminate the frequency of an incoming signal has long been a requirement in communication, radar, and electronic warfare systems. One of the most widely used techniques to date is known as Instantaneous Frequency Measurement (IFM). IFM is based on an autocorrelation measurement of the received signal with a fixed time delay of τ_d. Early IFM receivers operated entirely in the analog domain. However, as early as the 1960's, developers began digitizing the output of the analog receivers, thus giving them the name DIFM receivers [19]. DIFM technology has evolved significantly since the early days. Today, a true DIFM receiver is considered one in which the entire processing is conducted in the digital domain. Although different DIFM architectures exist, the standard form is depicted in Figure 5.1 [20, 21].

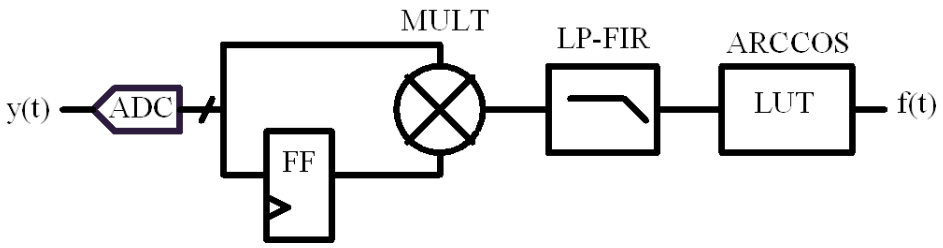

Figure 5.1: Digital Instantaneous Frequency Measurement receiver

The digitized incoming signal is split between two paths. One path is fed directly to a digital multiplier unit. The other path contains one or more delay elements before sending the signal to the same multiplier. In an analog IFM approach the time delay τ_d of the path can be set at any continuous value. However, in the all-digital version described within this dissertation, the delay path can only be set to multiples of the ADC sample time interval τ_{adc}. Thus, the path may contain one or more delay registers, the number of which will determine the usable frequency detection bandwidth. This will be analyzed further later in the chapter.

It has been shown that for an input carrier signal of $y(t) = A_c \cos(2\pi f_c t))$, after digitization and mixing, the resulting output signal will be of the form [20]

$$\begin{aligned} y_{mix}[n] = & \frac{A_c^2}{D^2} 2^{2N-1} [\cos(2\pi f_c \tau_{adc} m) + \cos(4\pi f_c \tau_{adc} mn - 2\pi f_c \tau_{adc} m)] \\ & + \frac{A_c^2}{D^2} 2^{2N} [\cos(2\pi f_c \tau_{adc} mn)\epsilon_q(n-m) + \cos(2\pi f_c \tau_{adc} m(n-m))\epsilon_q(n)] \\ & + \epsilon_q(n)\epsilon_q(n-m) \end{aligned} \tag{5.1}$$

For equation 5.1, A_c is the carrier amplitude, N is the number of ADC bits, D is the input-voltage dynamic range, and ϵ_q is the quantization error. The number of ADC delay samples is specified by m. As can be seen from the equation, two terms exist near DC. One contains the instantaneous carrier frequency information, the other, the quantization error magnitude. The DC terms are extracted from the output of the mixing stage by running the signal through a low-pass FIR filter, resulting in equation 5.2, where $|H_{LPF}(0)|$ is the low-pass filter gain at DC.

$$y_{filt}[n] = |H_{LPF}(0)|[\frac{A_c^2}{D^2}2^{2N-1}[\cos(2\pi f_c \tau_{adc} m)] + \epsilon_q(k)\epsilon_q(n-m)] \tag{5.2}$$

It was shown in [20] that, for even a 10-bit ADC, the quantization error is negligible. However, most all-digital demodulators will utilize 12-16 bit ADCs to maximize the low-end dynamic range. Thus, the contribution from quantization noise can usually be ignored. Using this assumption, and performing some algebraic reorganizing, the resulting equation provides the instantaneous carrier frequency as its output.

$$f_c \approx \frac{1}{2\pi\tau_{adc}m} \arccos\left(\frac{y_{filt}[n]}{|H_{LPF}(0)|\frac{A_c^2}{D^2}2^{2N-1}}\right) \tag{5.3}$$

One issue that arises with DIFM receivers is their dependence on the amplitude of the carrier A_c. It can be seen from equation 5.3 that the arccos term is a function of both $y_{filt}[n]$ and A_c. In early DIFM receivers utilizing analog front-ends this dependency was compensated for with the use of auto gain controllers and equalization filters. Recently, an all-digital approach to amplitude correction was published [20]. This technique uses the fact that if $m = 0$ in equation 5.2, it can be reduced to

$$y_{amp}[n] = |H_{LPF}(0)|\frac{A_c^2}{D^2}2^{2N-1} \tag{5.4}$$

Equation 5.4 is in fact the peak amplitude output of equation 5.2 . Therefore, dividing equation 5.2 by 5.4 yields an amplitude independent output equation.

$$y_{out}[n] = \cos(2\pi f_c \tau_{adc} m) \tag{5.5}$$

Most DIFM implementations utilize lookup tables in order to extract the instantaneous carrier frequency f_c from the cosine term. However, as will be discussed later in the chapter, such steps are not required within this work. The value $y_{out}[n]$ can be used directly in the dynamic range extension approach.

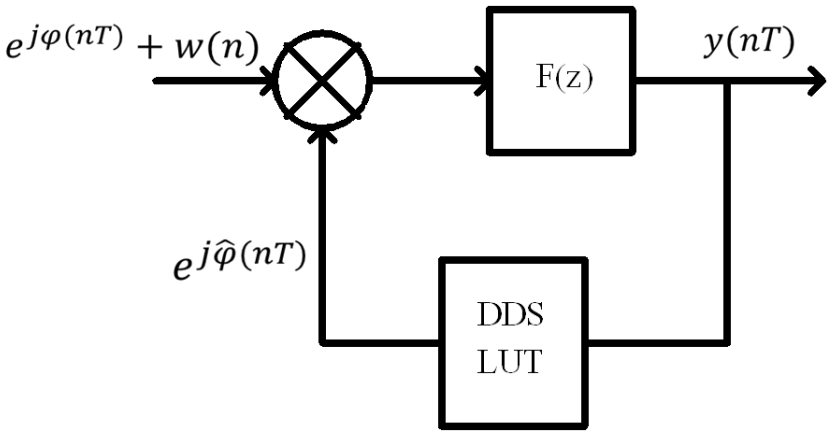

Figure 5.2: Digital phased locked loop

The literature review has shown that the DIFM method of frequency discrimination is well suited for the research within. Literature was also identified which demonstrated a reliable approach to removing the standard DIFM carrier amplitude dependency issues. It should also be noted the efficiency at which the DIFM output value can be processed. The output can be calculated in real-time and at high-speeds with as little as a single multiplier, adder, and divider circuit. Because of this efficiency, DIFM will be evaluated as one of the primary frequency measurement techniques later in the chapter.

5.1.2 Digital PLLs

Phased locked loop technology has long been used for frequency discrimination. With the recent interest in SDR, researchers have published numerous papers covering the topic of DPLLs. Their implementation largely follows that of their analog counter part. Figure 5.2 depicts one recently reported DPLL implementation [22].

A DPLL is comprised of three main components: a phase detector, a loop filter, and a Direct Digital Synthesizer (DDS) circuit. The first component is the phase detector. The phase detector is typically implemented as a digital multiplier, where the incoming digitized signal is multiplied by both the in-phase and quadrature version of the reference signal. The output of the phase detector contains both the low frequency signal of interest and an unwanted high

frequency component. As a result, the output of the phase detector is passed through the second main component, the loop filter. The loop filter is a 1^{st} order low-pass digital filter, the output of which is an error signal used to frequency adjust the DDS. The DDS is responsible for producing the sine and cosine versions of the reference frequency, given the error input from loop filter. DDS circuits are commonly implemented as large lookup tables in memory.

The published reports on DPLL technology has largely been underwhelming [22, 23]. While it may serve its purpose in some applications such as FM receivers, it is not well suited for instantaneous frequency measurement when compared to other available options. The literature has shown that the processing time is significant and the output rate is slow. While the performance could be improved with additional hardware, the typical DPLL already uses significantly more resources than a DIFM receiver. There are also issues with tracking large phase and frequency excursions. Because of these issues, DPLL technology is not considered a viable option for frequency discrimination in the dynamic range extension approach.

5.2 Digital Instantaneous Frequency Measurement

It was shown previously in this chapter that DIFM is a viable and efficient technique for measuring the instantaneous carrier frequency. The process involves making two autocorrelation measurements and dividing the results. One autocorrelation measurement is made with a fixed number of ADC delay samples given by m. The other is made with a zero delay (i.e. $m = 0$). The zero delay measurement determines the peak output value of the autocorrelation process and is used to normalize the non-zero delay autocorrelation value. Using this approach, one obtains the following:

$$y_{out}[n] = \cos(2\pi f_c \tau_{adc} m) \tag{5.6}$$

Further processing could be performed in order to extract f_c; however, it is not required. As will be shown, the output value y_{out} can be used directly. What is left to be determined is the

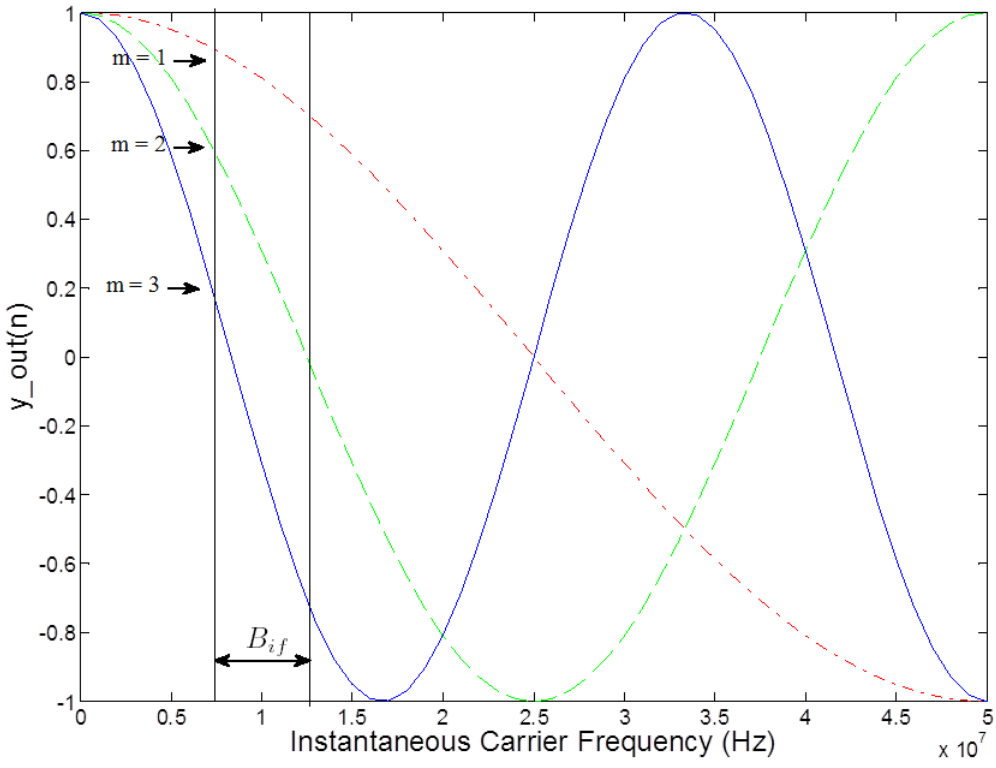

Figure 5.3: y_{out} for different sample delays m

optimal value of m. For most systems f_c and τ_{adc} will be fixed based on the available hardware. This then leaves the value of m to determine the usable range of y_{out}. For example, the heterodyne interrogation hardware and demodulation electronics used in the experimental portion of this research use a nominal carrier frequency of $f_c = 10$ MHz and an ADC sample rate of $f_{adc} = 100$ MHz. Given these values, Figure 5.3 shows the usable y_{out} range for $m = 1, 2$, and 3.

In selecting the optimal value of m, the bandwidth B_{if} of the instantaneous carrier frequency about the nominal carrier frequency must be considered. For sinusoidal modulation, the bandwidth can be determined from $B_{if} = 2A_s f_s$, twice the peak fringe rate of the signal. A bandwidth of $B_{if} = 5$ MHz will be assumed for the moment. The optimal choice of m is one which provides a nearly linear output of y_{out} over the range of B_{if}, around the nominal carrier value. It must also provide a large differential in the output y_{out}. As can be seen in Figure 5.3, for $m = 1$, the output is in the non-linear part of the curve, and the differential output over

the bandwidth around f_c is very limited. For $m = 2$, the output operates much closer to the linear part of the curve. The differential output over the given bandwidth has also significantly increased. The optimal value, however, is obtained for a value of $m = 3$. This value provides a highly linear and wide differential output over the required measurement bandwidth. As such, a value of $m = 3$ will be utilized for the following simulations and experimental tests.

It should be noted that the issue of optimal m selection was addressed in [20]. It was shown that a DIFM receiver should use $m = 1$, provided that $f_c = f_{adc}/4$. It can be seen in Figure 5.3 that if $f_c = 25$ MHz, the output will be linearly optimized for $m = 1$. However, the differential output over the bandwidth would be much less than that for $f_c = 10$ MHz and $m = 3$. The lower differential output will be shown in the next chapter to make the dynamic range extension approach more susceptible to noise. Therefore, a proper evaluation based on system parameters should be conducted when selecting a value for m.

5.2.1 Hardware Implementation

A value of $m = 3$ was just shown to be optimal for the DIFM application at hand. Other design implementation considerations must still be addressed. In a typical implementation, such as that shown in Figure 5.1, a low-pass FIR filter is placed after the digital multiplier performing the frequency mixing. The performance of this filter is critical in suppressing high-frequency components from generating noise in the output. While complex FIR filter types could be utilized, a simple rectangular (boxcar) filter provides sufficient attenuation levels provided the input data is properly windowed. In the all-digital demodulation architecture used within this dissertation, proper windowing of the incoming data is required for the rectangular FIR filters following the I/Q multipliers. Thus, the windowed data is already available to the DIFM receiver with no additional processing required. The rectangular FIR filters can therefore be reduced to a simple summing circuit. Figure 5.4 shows the DIFM hardware architecture, implemented within an FPGA, as part of the experimental portion of this dissertation.

One advantage of the DIFM implementation in Figure 5.4 is the limited number of hardware resources required. The entire receiver can be constructed with as little as one multiplier, one

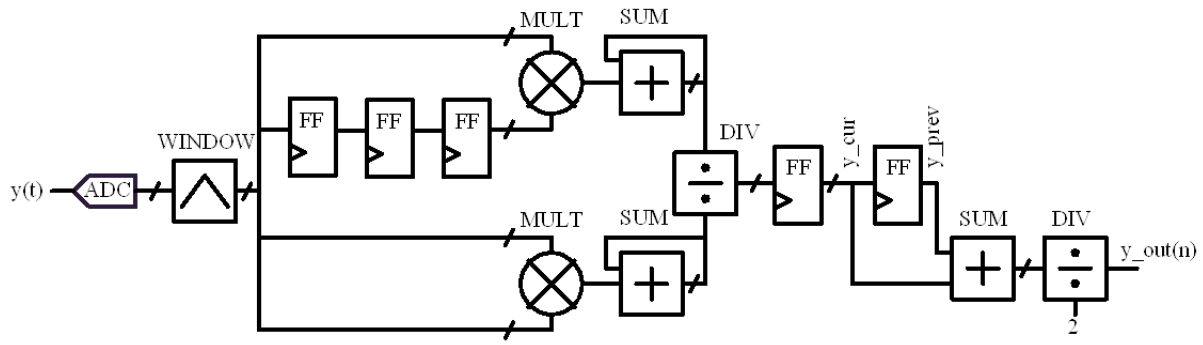

Figure 5.4: DIFM hardware implementation

adder, and one divider circuit. However, for the demodulator presented within this dissertation, a parallel processing approach is required to reduce the overall computation time. The additional summing and divider circuitry at the end of the processing chain is used to implement a two-point instantaneous frequency average. This will be shown in the following chapter to improve the reliability of the dynamic range extension technique. The required hardware resources for the parallel processing approach is still significantly less than for the other frequency measurement techniques presented later in the chapter. In addition to the hardware efficiency, the DIFM method also provides excellent frequency tracking, as will now be shown in the following simulations.

5.2.2 Simulations

A heterodyne demodulation simulation script was developed in MATLAB. This simulator can be configured to evaluate a wide range of system parameters and operating conditions. The simulations were configured to match the parameters of the available heterodyne demodulation hardware used in the experimental portion of this work. These system parameters are as such: $f_c = 10$ MHz, $f_{adc} = 100$ MHz, and $N_{adc} = 16$ bits. The demodulation hardware output sample rate is $f_d = 81920$ Hz. However, it was determined early in the development of this system that the high-end dynamic range would not be met with this sample rate. Therefore, a demodulation oversample rate of $f_{samp} = 655360$ Hz (81920 Hz * 8x oversample rate) was utilized. This was determined to be the fastest interrogation rate achievable without impacting the low-end noise floor, given the

demodulation approach and available hardware. The oversampled data is filter decimated back down to the desired rate of 81920 Hz. The use of oversampling and filter-decimating the data not only provides a higher upper-end dynamic range, it also provides a low-end dynamic range improvement as some of the noise is averaged out.

The simulations within will be conducted using the oversample rate since this is the rate at which the demodulation hardware must be able to perform. Given $f_{samp} = 655360$ Hz, the maximum optical pulse width at the demodulator will be 763 nsec; however, edge transition times and transient effects will limit this to a lesser window. A 500 nsec window within each pulse is utilized, equaling 50 ADC data samples at 100 MHz of the received 10 MHz nominal carrier signal. The MATLAB code used to simulate the DIFM hardware of Figure 5.4 is shown below, where *D_samp* is the 50-point Nuttall-windowed carrier signal data. The full simulation code is provided in Appendix A.

Listing 5.1: DIFM MATLAB simulation code

```
DIFM_auto = sum([D_samp,0,0,0].*[0,0,0,D_samp]);
DIFM_cf   = sum(D_samp.*D_samp);
DIFM_last = DIFM_cur;
DIFM_cur  = DIFM_auto/DIFM_cf;
DIFM_avg  = mean([DIFM_cur  DIFM_last]);
```

As was stated earlier, the dynamic range extension approach requires an average instantaneous carrier frequency measurement between the current and the previous demodulation point. Thus, the output value of both the simulator and the actual hardware implementation is a two point average. Therefore, the following simulations plot the given input waveform versus the average instantaneous carrier frequency.

The first simulation to be conducted is a carrier noise floor analysis. The level of noise in the output must be sufficiently small in order to ensure that errors are not potentially introduced by the dynamic range extension approach itself into the demodulated output. Figure 5.5 shows the DIFM noise floor with no input signal. A 40 dB CNR is used since this will be shown to be a minimum receive level for most fiber-optic interferometer systems. As can be seen from the figure, the peak-to-peak noise level of y_{out} is approximately .004. This will be shown in

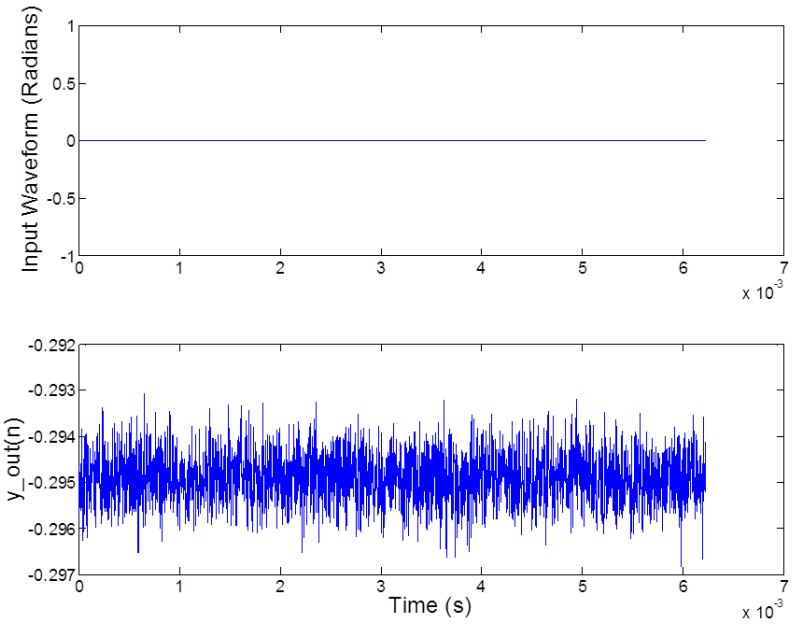

Figure 5.5: Simulated DIFM output with $A_s = 0$ radians, and CNR = 40 dB

the next chapter to equal 3% noise in the dynamic range extension technique. This low level of noise is well tolerated by the interferometer system presented within this dissertation.

The nominal output value of y_{out} in Figure 5.5 is also of interest. Based on equation 5.6, a nominal value of -.309 would be expected for $m = 3$ and $f_c = 10$ MHz; however, a value of -.295 is actually obtained. It was determined via simulations that this small difference is the result of windowing the input data. Experimental testing has confirmed these findings. Experimental testing has also found that the windowed boxcar filtering approach provides substantially lower high-frequency noise components in the output when compared to other FIR filter types. As a result, the windowed boxcar approach provides the best results despite the small offset in the output.

The next three simulations were conducted with a sine wave signal input that results in a peak carrier bandwidth of $B_{if} = 6.4$ MHz. This value represents the bandwidth required for a 20 dB dynamic range extension. The input waveforms have been Hanning weighted to reduce startup transients. A CNR of 40 dB was assumed. Figure 5.6 shows the simulation results for an input of 3200 radians at 1 kHz. As can be seen, the output y_{out} closely tracks the

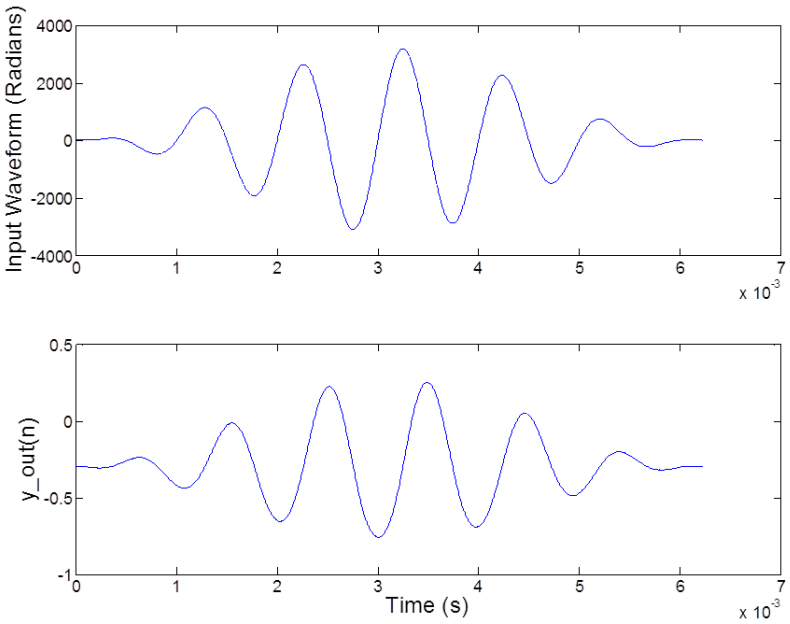

Figure 5.6: Simulated DIFM output with $A_s = 3200$ radians, $f_s = 1$ kHz, and CNR = 40 dB

waveform shape of the input. The apparent phase shift in the output is a result of the instantaneous frequency being the derivative of the phase. When the input is at a minimum or maximum, the instantaneous carrier frequency approaches its nominal y_{out} value. Likewise, when the input crosses the x axis, the rate of phase change is at its maximum, resulting in the peak instantaneous values.

The output values obtained for y_{out} match those expected from the plot of Figure 5.3 over the bandwidth of interest. A nominal output value of -.295 is obtained. The simulation peaks are at values of 0.252 and -0.757. Calculated peak values are at 0.285 and -0.794. These small variations are primarily the result of the input waveform not being sampled exactly at the peak frequencies. Simulations using either higher sample rates or lower input frequencies have confirmed this analysis.

Figure 5.7 shows the simulation for a sine wave of 320 radians at 10 kHz. The carrier bandwidth has been maintained at $B_{if} = 6.4$ MHz. As expected, the peak y_{out} values obtained are now 0.258 and -0.756, nearly identical to that measured in the previous simulation.

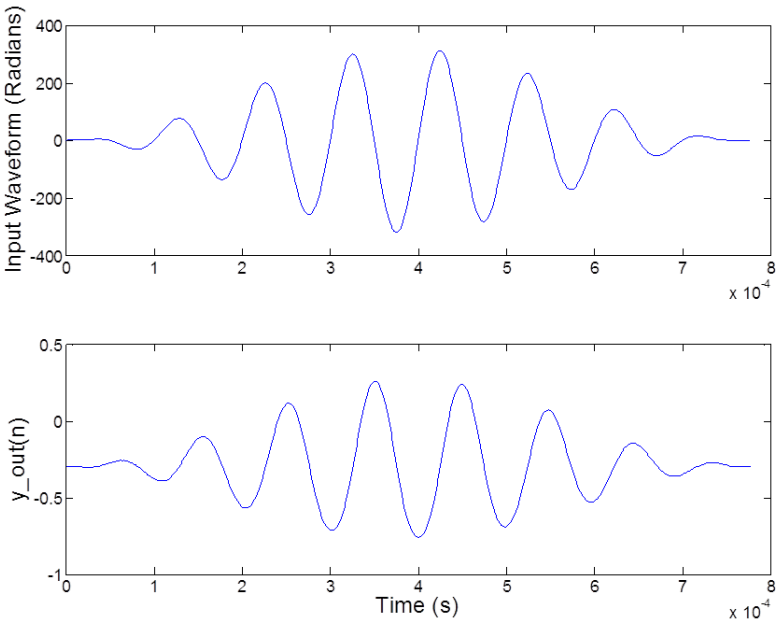

Figure 5.7: Simulated DIFM output with $A_s = 320$ radians, $f_s = 10$ kHz, and CNR = 40 dB

If the input frequency is increased by another factor of 10, but the peak bandwidth is again maintained, we see the same results as the previous two simulations. Figure 5.8 plots the results for an input sine wave of 32 radians at 100 kHz. The simulated peak y_{out} values are at 0.20 and -0.711. These reduced numbers are, again, the result of the sampling points relative to the peak values of the waveform and are not an issue.

These simulations have shown that the instantaneous carrier frequency can be accurately tracked over a wide bandwidth. This approach works well for both low-frequency and high-frequency input waveforms. There are, however, limitations to this approach, which will now be addressed.

5.2.3 Limitations

Two potential limitations to the DIFM approach are the minimum CNR requirements and the peak maximum bandwidth. The first issue to be addressed is the CNR requirement. It is well known that Frequency Modulated (FM) and phase modulated systems require a minimum

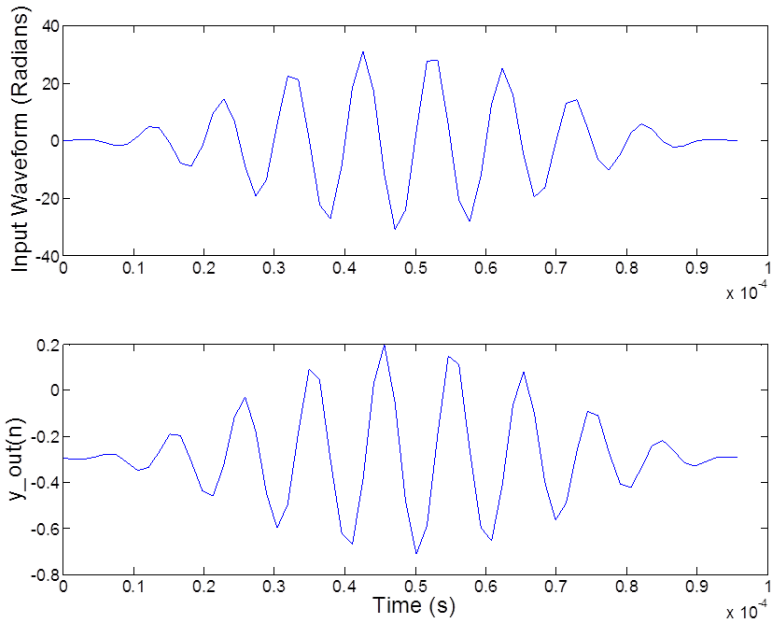

Figure 5.8: Simulated DIFM output with $A_s = 32$ radians, $f_s = 100$ kHz, and CNR = 40 dB

CNR ratio to operate. It is also known that the quality of the received signal in an FM system improves as the CNR increases. Therefore, there are two issues to be addressed regarding CNR levels in a DIFM receiver. First, what is the minimum CNR requirement to operate? Second, what CNR levels are required such that the noise levels do not introduce error in the demodulated output?

The simulations shown previously utilized a CNR of 40 dB. The simulation shown in Figure 5.7 is now repeated at CNR levels of 6,12, and 18 dB. Figure 5.9 shows the DIFM output with only a 6 dB CNR level. As can be seen, while the carrier signal still appears to be tracked, the levels of high-frequency noise is significant and would result in substantial error being introduced into the dynamic range extension approach. Figure 5.10 shows an improvement in the output by increasing the CNR to 12 dB. However, this still contains levels of noise which are incompatible with the approach presented in the next chapter. By increasing the minimum CNR to 18 dB, such as in Figure 5.11, the noise levels are sufficiently low so that DIFM output can reliably be used to extend the dynamic range. Increasing the CNR levels further only helps to eliminate noise and improve reliability in the process.

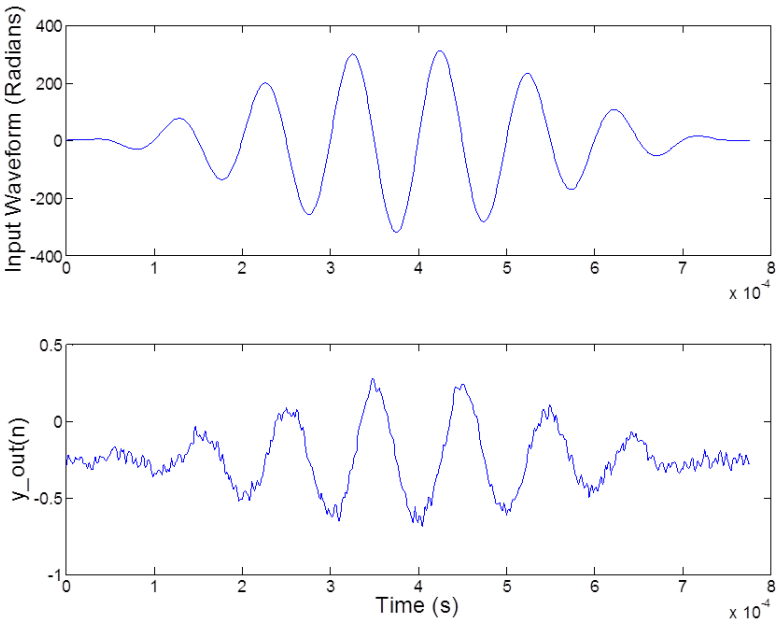

Figure 5.9: Simulated DIFM output with $A_s = 320$ radians, $f_s = 10$ kHz, and CNR = 6 dB

The CNR is one of the most critical parameters in a fiber-optic interferometric systems. A high CNR must be maintained in order to obtain a low-noise floor in the measurement band of interest. Such systems will typically have a CNR level that exceeds 40 dB. Therefore, since noise in the DIFM approach is only an issue for CNR levels below 20 dB, it can be assumed that this will be a non-issue for most practical systems.

The second limitation of the DIFM approach which must be addressed is the maximum bandwidth that can be utilized. It was shown previously that the DIFM technique worked well over a bandwidth $B_{if} = 6.4$ MHz. This bandwidth will be shown in the next chapter to facilitate a 20 dB dynamic range improvement over the standard demodulator output for the specified system parameters. The question that must now be addressed is, what is the maximum increase that can be achieved? This is, again, largely related to the selection of the delay value m. The value of m is chosen to bias the output in the linear part of the cosine curve. It is also chosen to provide a large differential in the y_{out} output over the desired bandwidth of the system. As will be shown, a large differential provides noise immunity in the tracked output and improves reliability in selecting the appropriate phase correction factor. However, increasing the differential output reduces the maximum bandwidth B_{if} that can be

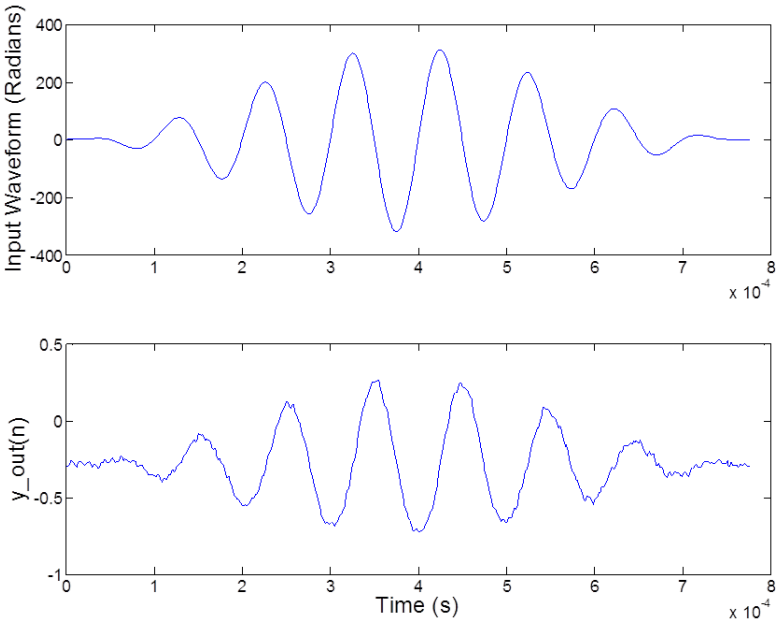

Figure 5.10: Simulated DIFM output with $A_s = 320$ radians, $f_s = 10$ kHz, and CNR = 12 dB

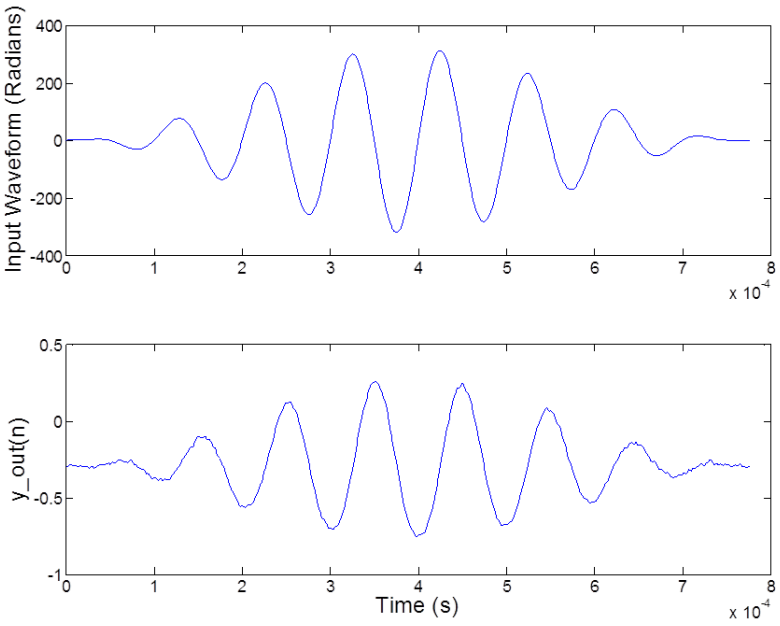

Figure 5.11: Simulated DIFM output with $A_s = 320$ radians, $f_s = 10$ kHz, and CNR = 18 dB

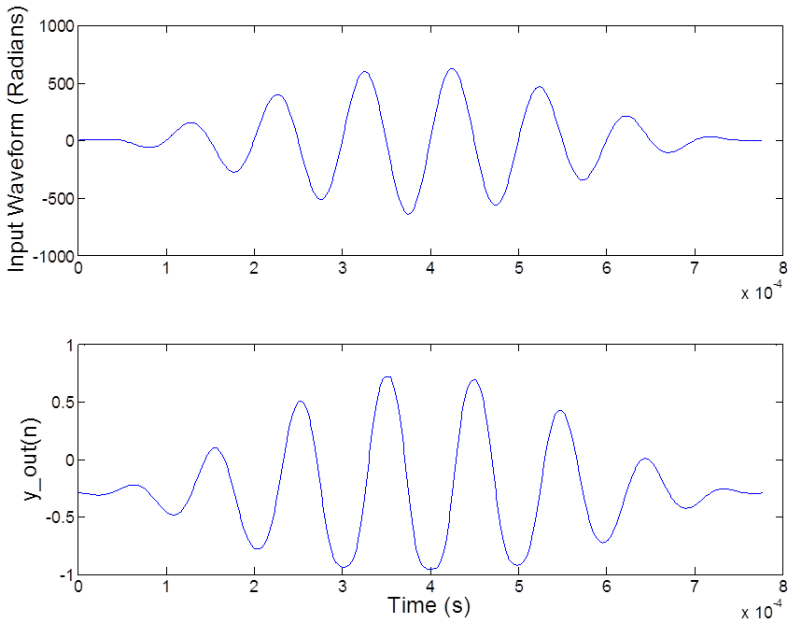

Figure 5.12: Simulated DIFM output with $A_s = 640$ radians, $f_s = 10$ kHz, and CNR = 40 dB

measured. A 26 dB dynamic range extension would require a bandwidth $B_{if} = 12.8$ MHz. Figure 5.12 shows the non-linear effects that would be introduced into the DIFM output at this bandwidth. While some non-linearity in the output can be tolerated, when the differential in the output between specified frequencies becomes less than the noise levels of the receiver, no additional gains can be achieved. Figure 5.13 shows the case when extending the bandwidth for a dynamic range extension of 32 dB. In this case, not only has the usable linear frequency range been exceeded, so has the range of the cosine output. Therefore, it can be shown that a hard bandwidth limitation exists for outputs that approach ± 1. The point at which this occurs is dependent on numerous system parameters.

The DIFM approach has been shown to have only one primary limitation: the maximum bandwidth that can be tracked. Its implementation requires few hardware resources, while its output has been shown to be able to successfully track both low and high frequency waveforms. The DIFM method is, therefore, well suited to the dynamic range extension approach presented in the next chapter.

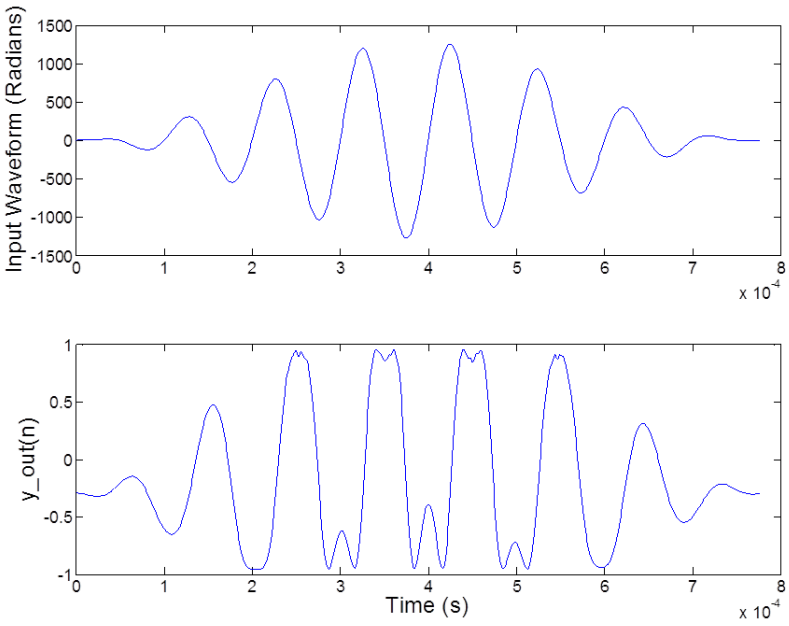

Figure 5.13: Simulated DIFM output with $A_s = 1280$ radians, $f_s = 10$ kHz, and CNR = 40 dB

5.3 Discrete Fourier Transform

Fourier analysis can be used for determining the instantaneous carrier frequency. In particular, a Fast Fourier Transform (FFT) could be utilized to track the carrier signal with a high degree of accuracy and resolution. However, the hardware requirements of such an approach would be excessively demanding when considering the bandwidth that must be covered and the rate at which it must carried out. Despite this, a reduced overhead DFT approach can be used. As stated previously, while the entire bandwidth of the carrier must be tracked, only a select set of frequencies must be measured. Determining which frequencies to track is a topic addressed in Chapter 6. However, to obtain a 20 dB dynamic range extension for the interferometer system used in the experimental portion of this dissertation, a total of 22 discrete frequencies must be tracked over a bandwidth of 6.4 MHz. This is feasible with most modern programmable hardware.

Equation 5.7 provides the DFT in a form that will be implemented within this dissertation.

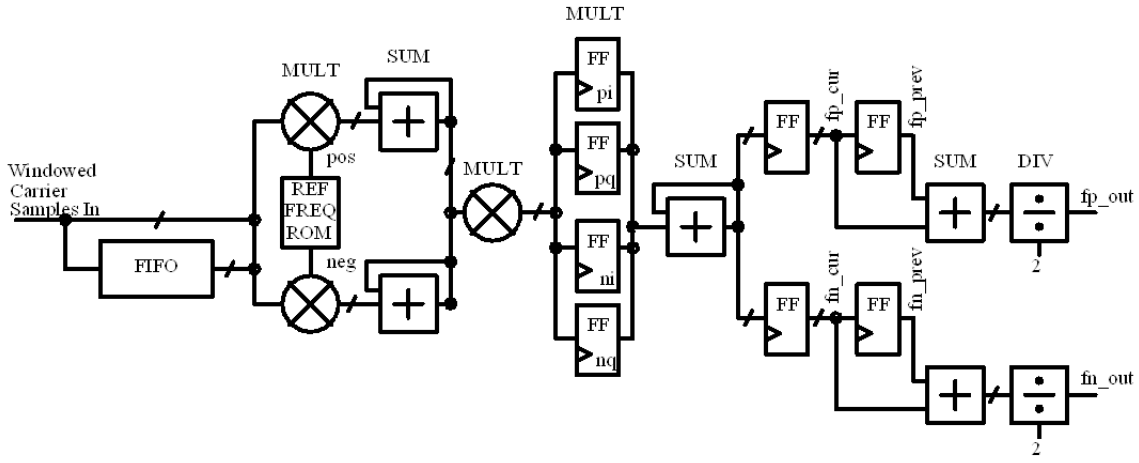

Figure 5.14: DFT processing hardware

$$X[k] = \sum_{n=0}^{N-1} x(n) \left(\cos(\frac{2\pi kn}{N}) - j \sin(\frac{2\pi kn}{N}) \right) \tag{5.7}$$

By multiplying the received carrier signal by the sine and cosine of the frequency being tracked and computing the magnitude, the Fourier coefficient of that frequency can be determined. If this operation is conducted for each of the selected frequencies in the desired bandwidth, the approximate instantaneous carrier frequency can be determined by selecting the largest coefficient. This approach works since the absolute frequency of the carrier signal is not required. Only the location of the instantaneous carrier signal within specific frequency bands of the system bandwidth is important.

5.3.1 Hardware Implementation

Numerous hardware implementations exist for computing a DFT. For an application such as this, where the results are needed at the same rate as the demodulator output, a high throughput approach is required. To meet the performance requirements of the demodulator used within this dissertation, a parallel processing DFT technique is used.

Figure 5.14 shows the hardware implementation of the DFT processing for the first two frequencies tracked. As can be seen from the figure, each frequency tracked requires two

dedicated multiplier and summing circuits. The reference frequency waveforms are stored in on-chip memory. The data being supplied to the DFT circuitry in Figure 5.14 is assumed to be windowed at the input to the demodulator. If this is not the case, then the data must also be windowed for the DFT processing to operate without significant errors being introduced.

A total of 44 dedicated multipliers and summing circuits are required to track the 22 DFT frequencies. Although the hardware requirements are not insignificant, they are implementable in most modern programmable devices. It should be noted that a significant reduction in the required hardware could be achieved with serialized hardware if the demodulation rates were reduced.

As with the DIFM approach, each DFT computation must be averaged between the current instantaneous frequency measurement and the previous one. This will again be shown to improve the reliability in the dynamic range extension approach. The averaging computations are conducted using the same hardware resources that perform the DFT processing for this implementation. Additional comparator circuitry is, however, required in selecting the highest DFT coefficient as the approximate instantaneous carrier frequency. This additional hardware is usually minimal.

5.3.2 Simulations

The MATLAB heterodyne demodulation scripts used in the last section were modified to support simulation testing of the DFT frequency tracking. The system parameters used were the same as those specified previously. Twenty-two frequencies were tracked over a bandwidth of $B_{if} = 6.4$ MHz. Half of the 22 frequencies tracked are where the expected demodulated output direction of rotation is positive, the other half are where the demodulated outputs are expected to have negative rotational directions. This will be explained further in Chapter 6. The MATLAB code for one positive frequency and one negative frequency is provided below. A full listing of the DFT simulation code is provided in Appendix C.

Listing 5.2: DFT MATLAB simulation code

```
fp   = fc + 1*fsamp/4;
fn   = fc - 1*fsamp/4;

DFT_c  = cos(2*pi*fp*t_ext).*D_samp;
DFT_s  = sin(2*pi*fp*t_ext).*D_samp;
DFT_m = sqrt(sum(DFT_s)^2 + sum(DFT_c)^2);
DFT_p_buf = [DFT_p_buf(2:end), DFT_m];
DFT_p_avg = mean(DFT_p_buf);
DFT_p = [DFT_p, DFT_p_avg];

DFT_c  = cos(2*pi*fn*t_ext).*D_samp;
DFT_s  = sin(2*pi*fn*t_ext).*D_samp;
DFT_m = sqrt(sum(DFT_s)^2 + sum(DFT_c)^2);
DFT_n_buf = [DFT_n_buf(2:end), DFT_m];
DFT_n_avg = mean(DFT_n_buf);
DFT_n = [DFT_n, DFT_n_avg];
```

The first simulation conducted of the DFT frequency discrimination approach is a carrier noise floor analysis. The analysis is again carried out using a CNR of 40 dB since this is a typical minimum level required by most fiber-optic interferometer systems. To demonstrate the noise performance of the system, four of the 22 frequencies being tracked are shown in Figure 5.15.

The displayed frequencies are the four closest to the nominal carrier at $f_c = 10$ MHz. Two of the frequencies tracked are with expected demodulated outputs of positive rotation. These occur at frequencies of 9.51 MHz and 10.16 MHz. The two frequencies tracked with expected demodulated outputs of negative rotation occur at 9.84 MHz and 10.49 MHz. Although difficult to see from the figure, the top trace is actually comprised of the DFT coefficients for both the 9.84 MHz and the 10.16 MHz frequencies. The bottom trace is comprised of the coefficients for 9.51 MHz and 10.49 MHz. These results are to be expected since the 9.84 MHz

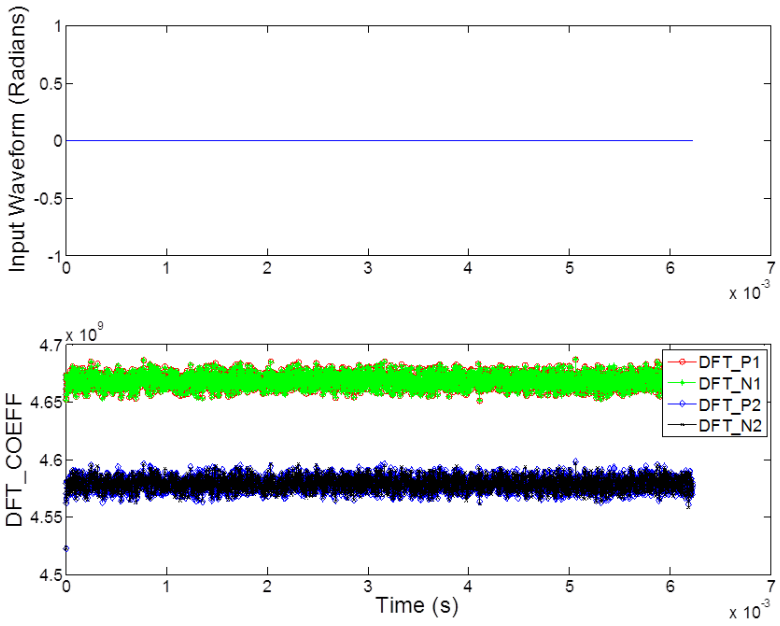

Figure 5.15: Simulated DFT output with $A_s = 0$ radians, and CNR = 40 dB

and 10.16 MHz frequencies are an equal $\frac{1}{4}f_{samp}$ away from the nominal carrier of $f_c = 10$ MHz. Likewise, the 9.51 MHz and 10.49 MHz are an equal $\frac{3}{4}f_{samp}$ away. With no input signal, the instantaneous carrier frequency should remain at the nominal carrier frequency, and any DFT coefficients taken at an equal distance from the carrier signal should remain equal. Therefore, these results are consistent.

As can be seen from Figure 5.15, the peak noise levels of the top two traces are equal to those of the bottom two. These levels, however, can be shown to cover approximately 30% of the dynamic range extension bands. This is a magnitude higher than that obtained for the DIFM approach. Still, this high level of noise will be shown to be satisfactory for a 20 dB dynamic range extension since the noise is common to all coefficients.

The next three simulations were conducted using the same waveforms as for the DIFM approach. These waveforms test the DFT instantaneous carrier frequency tracking abilities over a bandwidth of 6.4 MHz, that which is required for a 20 dB dynamic range extension. The first simulation is shown in Figure 5.16. The waveform is a Hanning weighted 1 kHz 3200 radian pulse. Plotted are the input phase signal and the DFT coefficients for the first four

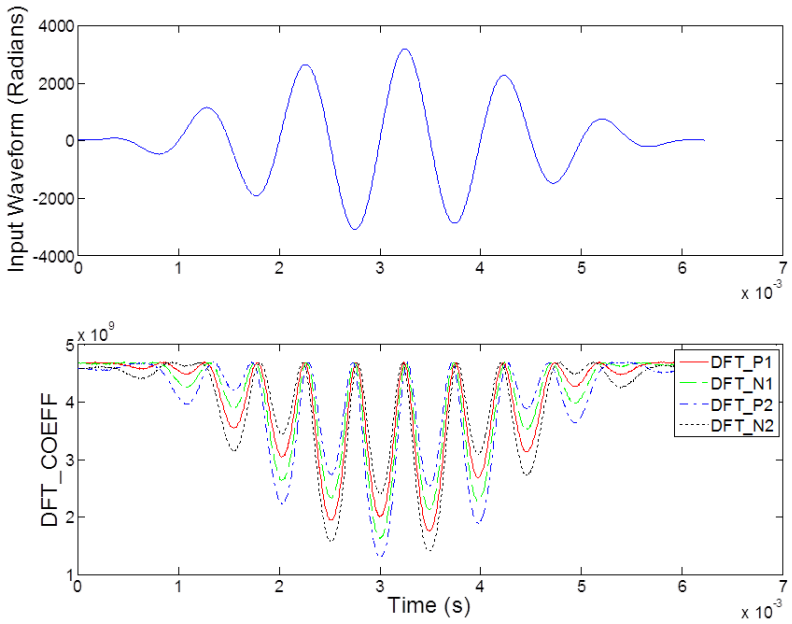

Figure 5.16: Simulated DFT output with $A_s = 3200$ radians, $f_s = 1$ kHz, and CNR = 40 dB

frequencies tracked, as discussed previously. This figure shows the ability of the DFT approach to successfully track the waveform over the specified bandwidth. As expected, where the angular velocity of the input waveform is at its highest, at the positive slope of the waveform, the DFT coefficient at 10.49 MHz is the highest. Likewise, when the angular velocity is at a minimum, the DFT coefficient at 9.51 MHz is the highest. This is as anticipated.

Figure 5.17 shows a zoomed in selection of the previous figure to clearly demonstrate how the DFT coefficients vary with the input waveform.

Figure 5.18 is a simulation with a 10 kHz 320 radian input waveform. The figure has, again, been zoomed in on a particular part of the waveform to more clearly show the changing coefficients. The results show that the coefficients accurately track the signal.

The last waveform test was conducted with a 100 kHz 32 radian input. The results are shown in Figure 5.19. This shows that even for high frequency input signals, the DFT approach can successfully track the instantaneous carrier frequency.

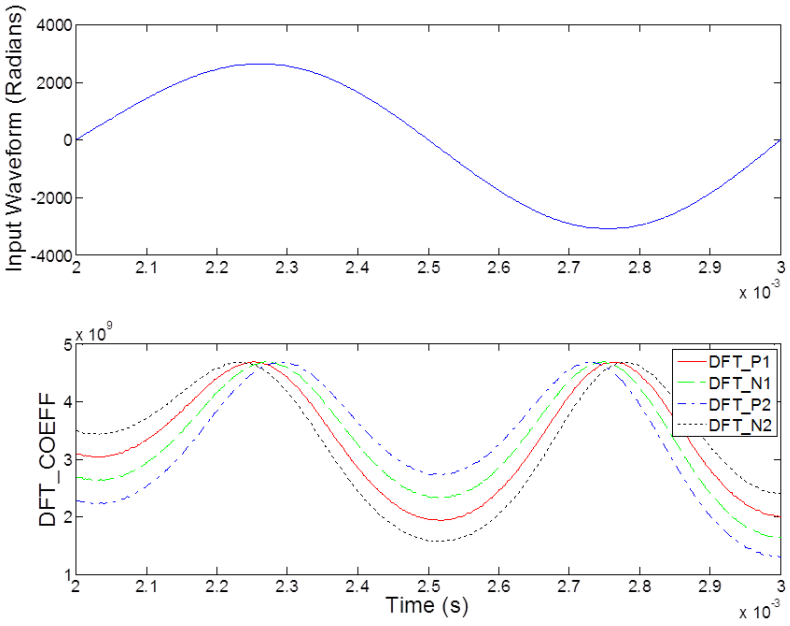

Figure 5.17: Simulated DFT output with $A_s = 3200$ radians, $f_s = 1$ kHz, and CNR = 40 dB (Zoom)

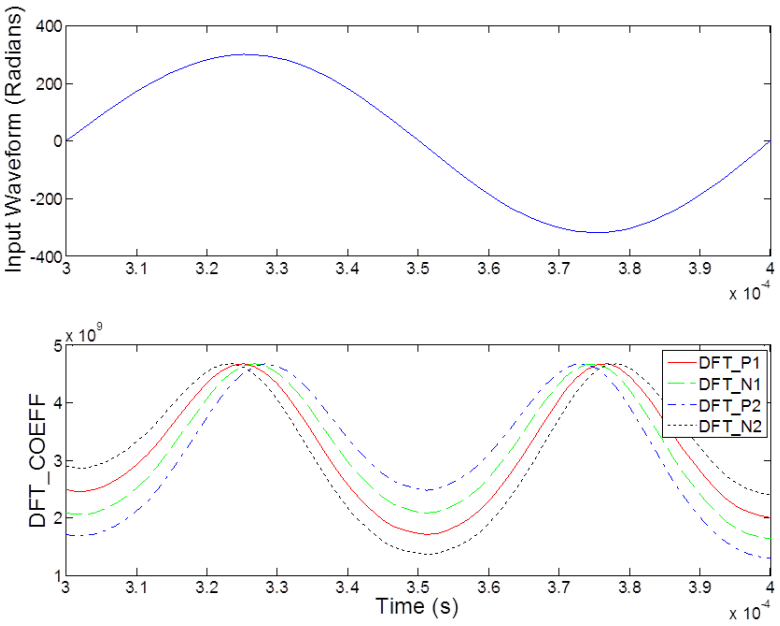

Figure 5.18: Simulated DFT output with $A_s = 320$ radians, $f_s = 10$ kHz, and CNR = 40 dB (Zoom)

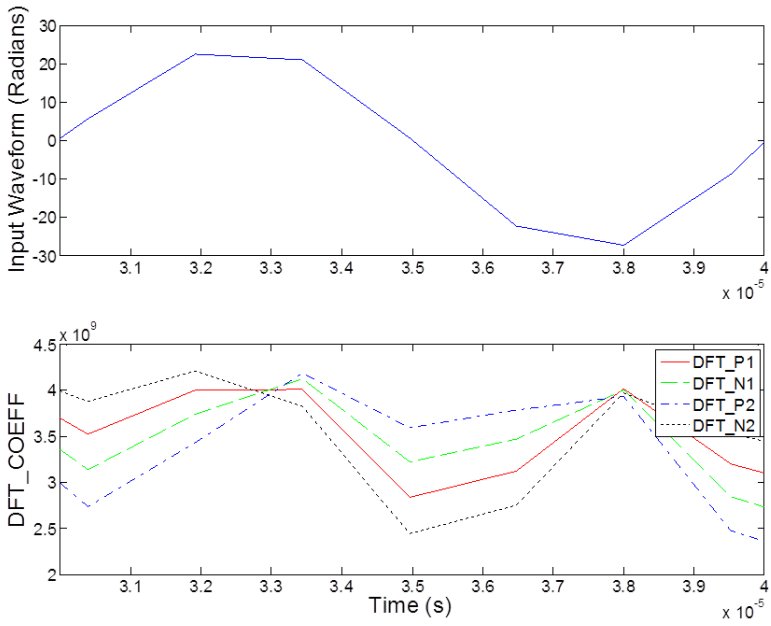

Figure 5.19: Simulated DFT output with $A_s = 32$ radians, $f_s = 100$ kHz, and CNR = 40 dB (Zoom)

5.3.3 Limitations

The primary limitation of the DFT method of frequency measurement is the required hardware resources. For the DFT hardware implementation used in this dissertation, each frequency tracked will require two dedicated multipliers and two summing circuits. The number of frequencies tracked depends on the desired dynamic range extension and the bandwidth that is required. Each additional 6 dB dynamic range that is added requires a doubling of the system bandwidth and the number of hardware resources. For dynamic range increases above 20 dB, the amount of hardware required can become excessive. This is in contrast to one the primary benefits of the DFT approach, which is that it is highly extensible to wide bandwidths. This allows, in theory, for much larger dynamic range increases than the other two frequency discrimination methods presented. However, the hardware requirements put a practical limit to the achievable gains.

The second limitation of the DFT approach is the CNR requirement. It was shown earlier that for a CNR of 40 dB, the noise floor of the DFT outputs was nearly 30% of the band

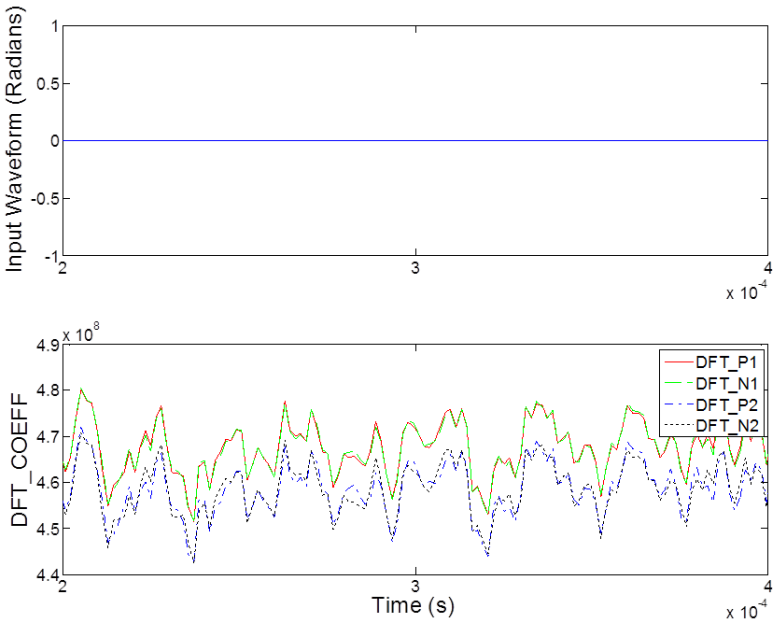

Figure 5.20: Simulated DFT output with $A_s = 0$ radians, and CNR = 20 dB (Zoom)

between adjacent measurement frequencies. This, at first, appears to be significant; however, dynamic range extension simulations have shown that this level of noise is well tolerated. This can be explained since the dynamic range extension approach takes only the highest DFT coefficient as the instantaneous carrier. It is also the result of the noise being common to all DFT measurements. Figure 5.20 show a zoomed in plot of the DFT noise floor with a 20 dB CNR.

It should be noted that the DFT dynamic range extension approach works in simulations with a 20 dB CNR. In fact, only a 6-12 dB CNR level is actually required for marginal operation despite the visibly high levels of noise. However, higher CNR levels will provide significantly improved levels of reliability. Figure 5.21 shows the noise floor with a 6 dB CNR.

Despite the apparently high levels of noise in the DFT measurement outputs, both the DFT and DIFM frequency discrimination techniques have roughly the same CNR requirements. Both can potentially operate with as little as 6 dB; but for higher reliability, a minimum of 20 dB is recommended. However, once again, since a minimum of 40 dB is generally required for low-noise interferometer operations, this limitation will not normally be an issue.

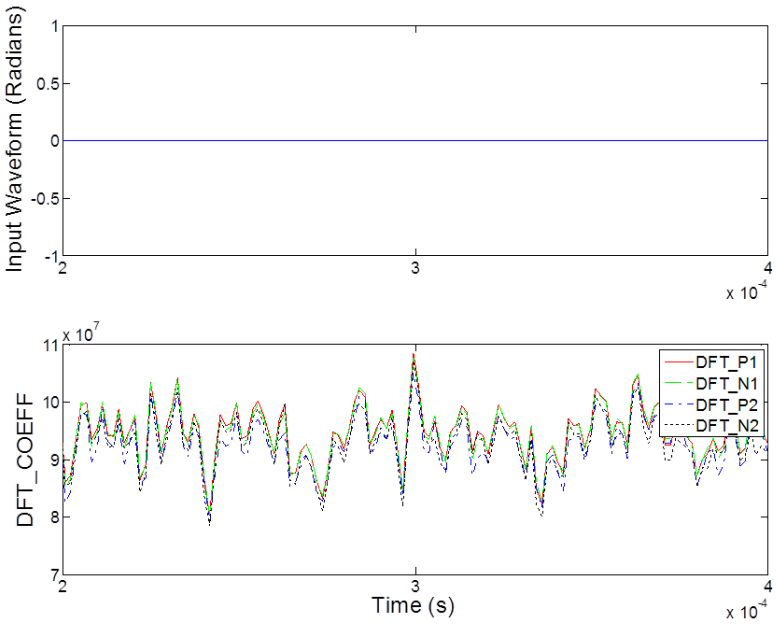

Figure 5.21: Simulated DFT output with $A_s = 0$ radians, and CNR = 6 dB (Zoom)

The only significant limitation the DFT approach is the amount of required hardware resources. Although the DFT outputs have higher levels of noise than the DIFM method, this does not appear to have an impact on its frequency tracking abilities. Therefore, the DFT method has been determined to be well suited for use in the dynamic range extension approach.

5.4 Period Expansion/Contraction Measurement

A unique method of frequency discrimination called Period Expansion/Contraction Measurement (PECM) was developed as part of this dissertation. This approach measures the amount of expansion or contraction of the carrier signal in the time domain. It was initially developed as a low hardware resource alternative to the DFT approach presented previously, before the DIFM method had been properly evaluated. While PECM is a viable approach, it will be shown that it suffers from more limitations than the other two methods presented, and the hardware resources utilization is only slightly less than that of DIFM. As such, it is being presented only for completeness of the chapter.

The PECM frequency discrimination technique is based on the standard definition for a periodic signal, where

$$x(t) = x(t+T) \tag{5.8}$$

If $x(t)$ is replaced with a sampled carrier signal (where $N = f_{adc}/f_c$), Equation 5.8 becomes

$$\sin(2\pi n/N) = \sin(2\pi(n+N)/N) \tag{5.9}$$

Equation 5.9 states that for a carrier signal which is sampled an integer N number of times per cycle, if a point on the curve is selected, then N points later the same value will be present. However, if the carrier signal deviates from its nominal frequency, then this assumption will be false and a difference between the two points will be measured. This difference can be determined from equation 5.10, where A_{max} is the maximum ADC value, and A_c is the peak sampled carrier amplitude.

$$y[n] = \left(\frac{A_{max}}{A_c}\right)\left(\sin\left(2\pi n\frac{f_i}{f_{adc}}\right) - \sin\left(2\pi\left(n+\frac{f_{adc}}{f_c}\right)\frac{f_i}{f_{adc}}\right)\right) \tag{5.10}$$

This approach requires that the samples be taken in the linear part of the curve. Ideally, the first sample would be taken directly at the zero crossing in order to maximize the usable range and minimize non-linear noise. This, however, is not generally possible and is one of the primary limitation of this method. How close to the zero crossing the signal can be sampled is dependent on the ratio of $\frac{fi}{f_{adc}}$. If the deviation from the zero crossing is small, then the equation above can be simplified to

$$y[n] = \left(\frac{A_{max}}{A_c}\right)\left(\sin\left(2\pi\frac{f_i}{f_c}\right)\right) \tag{5.11}$$

Equation 5.11 shows that if the zero crossing is used as the reference point, the output value

$y[n]$ will vary according to the ratio of the instantaneous carrier frequency to the nominal carrier frequency. The value of $y[n]$ can be used directly in the dynamic range extension approach.

One technique that was found to minimize the zero crossing error and to maximize the linear output range is to measure the differential across only a half carrier cycle. Using this approach, equation 5.10 becomes

$$y[n] = \left(\frac{A_{max}}{A_c}\right)\left(\sin\left(2\pi n\frac{f_i}{f_{adc}}\right) + \sin\left(2\pi\left(n + \frac{f_{adc}}{2f_c}\right)\frac{f_i}{f_{adc}}\right)\right) \tag{5.12}$$

The half carrier cycle approach was determined to be a substantial improvement over the full carrier cycle approach. Yet, there are still several issues which limit its overall usability. These will now be addressed in the following simulations.

5.4.1 Hardware Implementation

Although an actual hardware implementation of the PECM method will not be tested as part of this dissertation, the following hardware implementation can be simulated. A half-cycle PECM method will be utilized for the simulations. For the PECM method to operate as designed, the carrier signal must be sampled as close to zero crossing as possible in order to maximize the linear output range. The carrier should also be sampled at the same relative point on each cycle of the carrier to reduce noise. These two requirements lead to an efficient implementation where the zero crossing is used as the reference point. The sample point either before or after the zero crossing can be utilized, provided the same point is used consistently. However, the maximum distance from the zero crossing to the carrier samples is dependent on the samples per carrier cycle. Therefore, simulations will be conducted at several different f_s sample rates.

5.4.2 Simulations

The following PECM MATLAB simulations utilize the same system parameters as outlined in the previous examples with two exceptions. First, the data samples have not been windowed. Windowing of the data samples for this approach does not provide any benefit; it only complicates the analysis. Second, the carrier sample rate f_{adc} will be varied to demonstrate the requirements for a high $\frac{f_{adc}}{f_c}$ ratio.

The following MATLAB code was used in the PECM simulations.

Listing 5.3: PECM MATLAB simulation code

```
PECM_last = PECM_cur;
for j = 1:samples
 if ( D_samp(j) < 0 ) && ( D_samp(j+1) > 0 )
   PECM_cur = D_samp(j) + D_samp(j+(fadc/fc)/2);
   break;
 endif;
endfor;
PECM_avg = (PECM_last+PECM_cur)/2;
PECM_lst = [PECM_lst PECM_avg];
```

A noise floor analysis was first conducted for the PECM method. The first simulation was conducted using $f_{adc} = 100$ MHz and a CNR of 40 dB. Figure 5.22 shows that under these conditions the peak-to-peak noise levels are roughly .04. This translates to a 10% error in the frequency measurement band of the dynamic range extension approach and can lead to noise in the demodulated output.

Increasing f_{adc} does not make a significant improvement in the noise floor. Figure 5.23 shows that for increasing f_{adc} to 500 MHz, only a slight improvement in the noise floor can be detected. This suggests the the high levels of noise are not related to the location of the samples relative to the zero crossing.

The high noise floor is a result of the CNR. While a 20 dB CNR was sufficient for both the

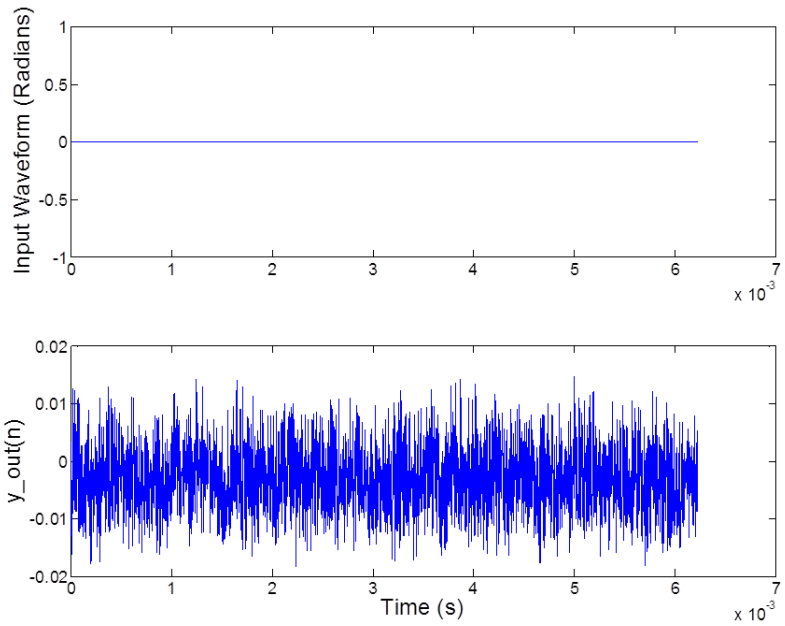

Figure 5.22: Simulated PECM output with $A_s = 0$ radians, $f_{adc} = 100$ MHz, and CNR = 40 dB

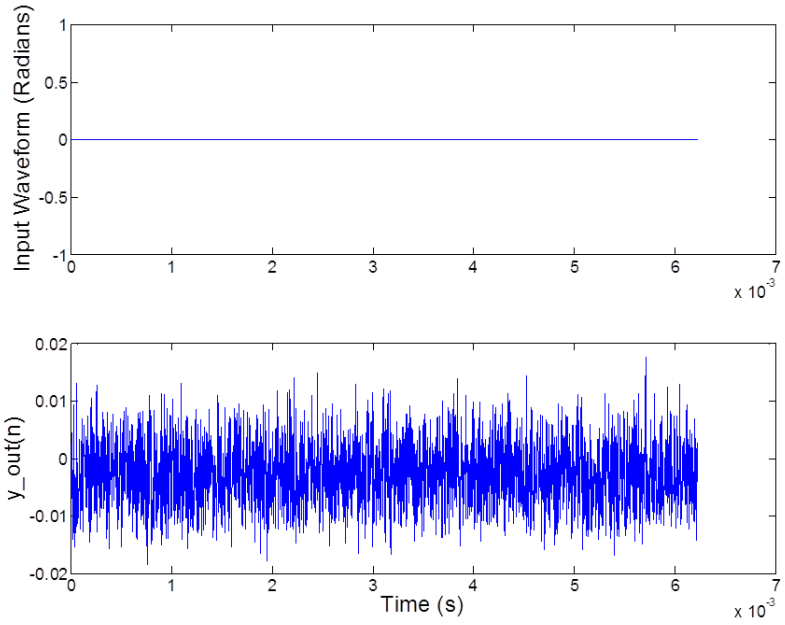

Figure 5.23: Simulated PECM output with $A_s = 0$ radians, $f_{adc} = 500$ MHz, and CNR = 40 dB

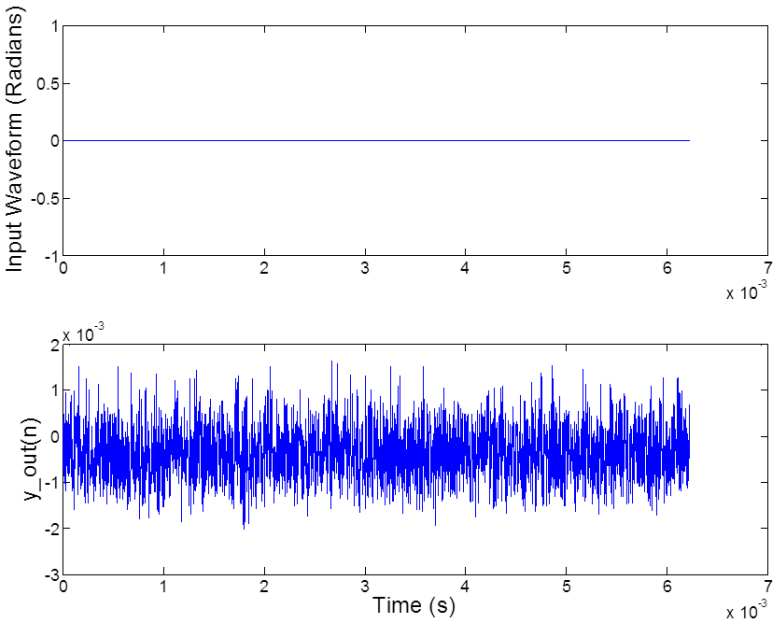

Figure 5.24: Simulated PECM output with $A_s = 0$ radians, $f_{adc} = 100$ MHz, and CNR = 60 dB

DIFM and DFT approach, for the PECM method, a 40 dB CNR is only marginally sufficient. Figure 5.24 shows the noise floor improvement by increasing the CNR to 60 dB. Under these conditions, the noise error has dropped to less than 1%, making PECM a potentially viable option for frequency discrimination. The issue, however, is that obtaining a CNR greater than 40 dB can be difficult in some applications.

For the remaining simulations, a 60 dB CNR will be assumed to eliminate it as a possible source of noise. A peak bandwidth $B_{if} = 6.4$ MHz is, again, used since this will be required to facilitate a 20 dB dynamic range extension. Figure 5.25 shows the ability of the PECM method to track a 3200 radian 1 kHz waveform using a carrier sample rate of $f_{adc} = 100$ MHz. Substantial noise can be seen in the output. This noise increases with the bandwidth of the waveform and is most severe at the peaks. Unfortunately, the peaks of y_{out}, or the inflection points of the input waveform, will be shown in the next chapter to be the most susceptible to generating errors in the dynamic range extension approach.

Since the noise of Figure 5.25 increases with the bandwidth of the signal, it can be shown to

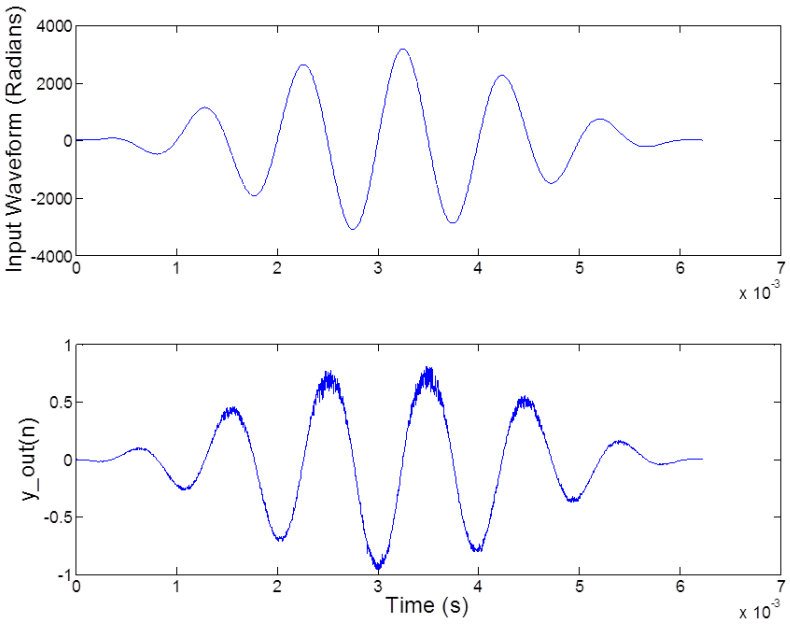

Figure 5.25: Simulated PECM output with $A_s = 3200$ radians, $f_s = 1$kHz, $f_{adc} = 100$ MHz, and CNR = 60 dB

be generated by non-linearities as a result of the sampling points relative to the zero crossing. This can be improved by increasing the f_{adc} sample rate to minimize this effect. Figure 5.26 shows the reduction in the output noise by increasing the sample rate to $f_{adc} = 500$ MHz.

Figures 5.27 and 5.28 show the PECM output for waveforms at 10 kHz and 100 kHz, both with $B_{if} = 6.4$ MHz.

As has been shown, the PECM method of frequency discrimination can successfully track the incoming waveforms and produce a low-noise output, provided the carrier signal has a high CNR and is significantly oversampled. These limitations are now addressed.

5.4.3 Limitations

The preceding simulations demonstrated the two primary limitations of the PECM frequency discrimination method; the first of which is a requirement for a high CNR. With both the

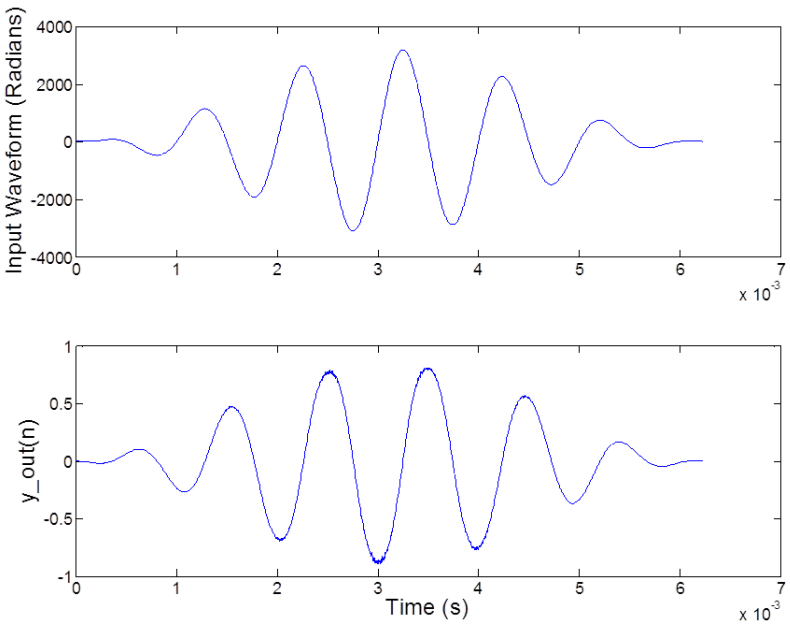

Figure 5.26: Simulated PECM output with $A_s = 3200$ radians, $f_s = 1$ kHz, $f_{adc} = 500$ MHz, and CNR = 60 dB

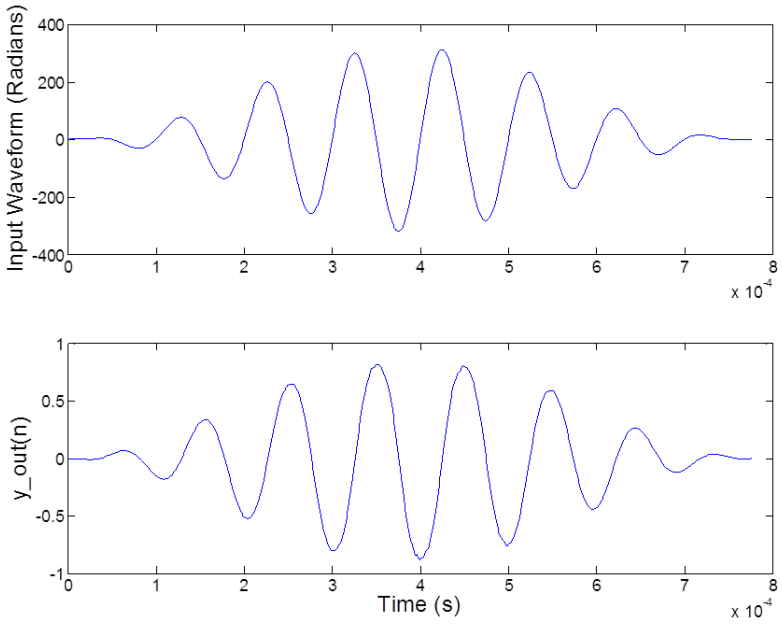

Figure 5.27: Simulated PECM output with $A_s = 320$ radians, $f_s = 10$ kHz, $f_{adc} = 500$ MHz, and CNR = 60 dB

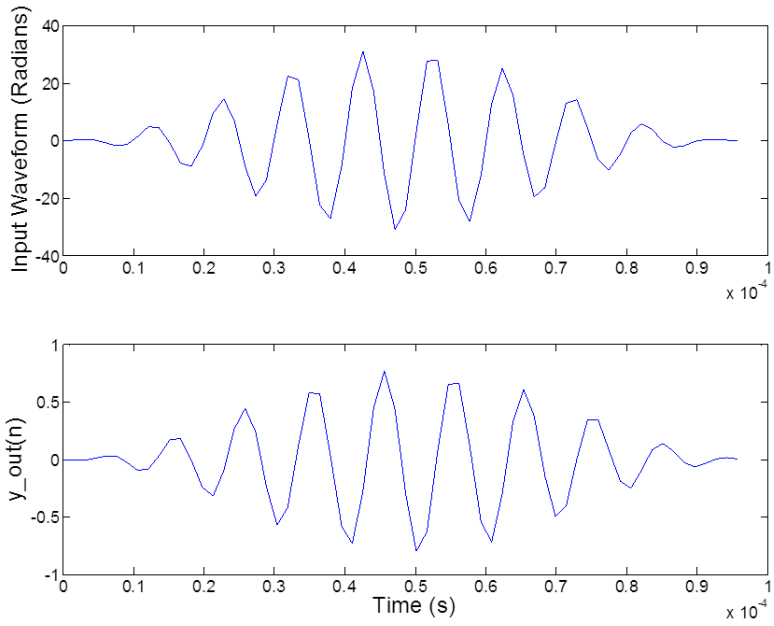

Figure 5.28: Simulated PECM output with $A_s = 32$ radians, $f_s = 100$ kHz, $f_{adc} = 500$ MHz, and CNR = 60 dB

DIFM and the DFT methods demonstrated previously, only a 20 dB CNR was required for successful operation. Higher CNR levels reduced the output noise levels further but was generally not required for successful implementation of the dynamic range extension. However, with PECM, the minimum CNR for operation is 40 dB, with 50-60 dB providing a higher reliability output. This can potentially become an issue for systems which already have a low CNR or for which may generally have a high CNR but momentarily drop as result of polarization signal fading.

The second significant limitation of the PECM method is the requirement for a high sample rate of the carrier signal. It was shown that for a 10 MHz carrier signal being sampled at 100 MHz, the non-linear noise generated at high bandwidths was high enough to make the method impractical. By increasing the sample rate to 500 MHz, the non-linear noise could be reduced to levels which made the approach feasible. However, increasing the demodulator sample rate can present several new challenges.

Because of the significant limitations of the PECM approach and because even with these

limitations, the output has a higher noise level than the DIFM method, PECM is not deemed as a viable frequency discrimination approach for most systems. Likewise, because a sample rate of $f_{adc} = 500$ MHz or greater is required for successful operation, the PECM method will not be tested in the experimental portion of this dissertation. The demodulator hardware available for the experimental testing is limited to $f_{adc} = 100$ MHz and would, therefore, only be viable for a dynamic range increase of approximately 6 dB.

5.5 Summary

Three methods of tracking the instantaneous carrier frequency have been successfully demonstrated. The DIFM approach provides a wide measurement bandwidth, a low noise output, and requires minimal hardware resources. The DFT method allows for the widest measurement bandwidth and, therefore, the largest potential dynamic range increase, but requires significantly more hardware resources than the other techniques presented. PECM offers the lowest hardware resource approach, but suffers from limited bandwidth and high noise. Both the DIFM and DFT methods of frequency measurement are considered viable options for the dynamic range extension technique. Both of these will also be evaluated experimentally in Chapter 7.

Chapter 6 Dynamic Range Extension Via Carrier Frequency Tracking

It was shown in Chapter 5 that the instantaneous carrier frequency in a heterodyne interferometer can be measured to the stated requirements. This chapter addresses how knowledge of the instantaneous heterodyne carrier frequency can be utilized to extend the high-end dynamic range. The first part of the chapter explores how phase excessions at the input of the demodulator introduce deterministic errors in the demodulated output. It is then shown how the instantaneous carrier frequency can be used to determine two valuable pieces of information: the instantaneous direction of phase rotation and the instantaneous angular velocity. These two pieces of information can be used to determine an excession correction factor which can be added to the standard demodulator output, thereby mitigating any errors. This will be shown to provide both an effective and efficient method of dynamic range extension. Dynamic range extension simulations are presented for both the DFT and DIFM methods of carrier frequency tracking. The efficiency and limitations of both are explored.

6.1 Demodulator Excessions

Knowledge of demodulator excession characteristics is vital for understanding the dynamic range extension approach presented within this dissertation. An excession occurs when the fringe rate of the signal being demodulated exceeds $\pm\pi$ radians between samples. In general, there are two types of excessions: those where the demodulated phase rotation direction is in error and those for which it correct.

The first type of excession encountered by a demodulator is one in which the demodulated output direction is in error. When the phase difference between two points is greater than $\pm\pi$, the demodulator, which uses a shortest path traveled algorithm to compute direction of phase rotation, will generate a demodulated output which is in error by 2π. For example, a positive phase rotation of $\frac{3}{2}\pi$ will result in a demodulated output of $-\frac{1}{2}\pi$. Thus, the difference between the actual phase rotation and demodulated output is -2π. A correction factor of 2π

must be added to the demodulated output to correct for the apparent phase reversal. Detecting that this type of excession has occurred and determining the appropriate correction factor can both be accomplished with knowledge of the actual phase rotation direction. It will be shown later in the chapter that this information can be obtained from the instantaneous carrier frequency.

With the second type of excession, the demodulated direction of rotation is valid. However, the input phase shift has still exceeded the limitations of the demodulator. This type of excession occurs when the phase difference between two sample points is greater than $\pm 2\pi$. Since the demodulator only has a measurement range of $\pm\pi$, a 2π rotation will cause a full-cycle phase wrap and will effectively be subtracted from the demodulated output. For example, a phase shift of $\frac{5}{2}\pi$ will be demodulated as $\frac{1}{2}\pi$. A 2π correction factor must again be added to the demodulated output to account for the phase wrap. Determining when a full cycle rotation has occurred and whether or not a correction factor must be added in is made possible by tracking the instantaneous angular velocity. Like the direction of rotation, it will be shown that the angular velocity can be acquired from the instantaneous carrier frequency.

In both excession examples provided above, the phase correction factor was 2π. If, however, the input phase shift exceeded $\pm 3\pi$, the demodulated phase would, again, undergo an apparent phase reversal. The correction factor now required would be 4π. Likewise, a phase shift greater than $\pm 4\pi$ would see the demodulated direction of phase rotation right itself. The correction factor would also be 4π. This pattern of phase reversal continues for each additional π radians added to the input signal. The required correction factor also increases by 2π for every 2π added to the input signal. Thus, the required correction factor will always be a multiple of 2π. These two patterns will play an important role in determining the appropriate correction factor for high fringe rate signals.

6.2 Direction of Phase Rotation

In the standard demodulation process, the direction of phase rotation can only be assumed. A shortest path traveled algorithm is used to predict the current direction of rotation. If, however, the phase advances by more than $\pm\pi$ radians between samples, this assumption will be false, and the demodulated output will be in error. As shown previously, this will introduce an apparent phase reversal in the output.

The instantaneous carrier frequency can, however, provide information regarding the actual instantaneous direction of rotation. The instantaneous direction of rotation can be determined from the instantaneous carrier frequency in equation 6.1 [24].

$$f_i(t) = f_c + \frac{1}{2\pi}\frac{d\phi_s(t)}{dt} \tag{6.1}$$

For sinusoidal phase modulation of $\phi_s(t) = A_s \sin(2\pi f_s t)$, equation 6.1 becomes

$$f_i(t) = f_c + A_s f_s \cos(2\pi f_s t) \tag{6.2}$$

Since the value of f_c is fixed, and it has been shown that the instantaneous carrier frequency f_i can be measured, this allows the value of $A_s f_s \cos(2\pi f_s t)$ to be computed. If $A_s f_s \cos(2\pi f_s t) > 0$, or $(f_i > f_c)$, then the angular phase rotation is determined to be in the positive direction. Likewise, if $A_s f_s \cos(2\pi f_s t) < 0$, or $(f_i < f_c)$, the angular phase rotation is in the negative direction. The instantaneous direction of rotation can therefore be determined simply by checking whether the nominal carrier frequency is greater than or less than the instantaneous carrier frequency. Since absolute frequency values are not required, this approach is well suited to all three frequency discrimination methods discussed in the previous chapter.

Information regarding the actual direction of rotation eliminates the guessing of the standard demodulator output. This, alone, can be used to achieve a 6 dB dynamic range increase. If

the actual direction of rotation and the demodulated direction of rotation do not match, then an excession has been detected. If the actual direction of rotation is in the positive direction, then 2π must be added to the demodulated output to correct for the excession error. Likewise, if the direction of rotation is negative, then -2π must be added. This simple approach, however, does not work for phase excursions exceeding $\pm 2\pi$.

6.3 Angular Velocity Determination

As was just shown, determining the actual direction of phase rotation allows for correcting the first excession point of the demodulator where the phase shifts exceed $\pm\pi$. However, it cannot correct for excessions that exceed $\pm 2\pi$. Correction of such excessions requires tracking of the instantaneous carrier frequency to determine the angular velocity. The instantaneous angular velocity can be used to estimate the magnitude of the phase shift between demodulation points. This will allow for determination of higher order 2π correction factors.

The instantaneous angular velocity ω_i can be derived from equation 6.2 for sinusoidal modulation.

$$\omega_i(t) = \omega_c + A_s\omega_s \cos(\omega_s t) \tag{6.3}$$

However, since the carrier frequency is removed from the equation during demodulation, the only angular velocity component that is of importance is that which is contributed by the input signal. This was shown previously to be simply the derivative of the input. Therefore, the instantaneous angular velocity of a sinusoidal signal ω_{is} is

$$\omega_{is}(t) = A_s\omega_s \cos(\omega_s t) \tag{6.4}$$

Since the units of ω_{is} are radians per second, if multiplied by the time step between demodulation sample points, an estimate can be obtained of the phase change between the two. The accuracy of this estimate, however, is dependent on several factors. First, since the

angular velocity of the signal is also sinusoidal in nature, the location at which the samples are taken is important. If the samples are taken in the linear part of the sinusoid, then the phase estimate will be much closer than for samples taken in the non-linear part of the curve. This leads to the second issue, which is the time step between samples. If the time step between samples is small, then the error will be small. If the time step is large, then the error will be large. Whether the time step is considered small or large depends on the frequency of the signal, relative to the demodulation rate. The higher the signal frequency, the higher the error in the estimate for a given sample rate. This effect will be shown to impose a frequency dependent limitation later in the chapter.

In general, multiplying the instantaneous angular velocity by the demodulation time step will result in a large error in the phase change estimate. As will be discussed later, some form of averaging of the instantaneous angular velocities must be utilized to improve the estimate. This averaging will reduce estimation error in the non-linear parts of the input signal, such as at inflection points. Provided that the signal's angular velocity is averaged over two or more points, a 2π excession correction factor can be calculated from equation 6.5, where n is the number of 2π that must be added or subtracted from the demodulated output. The plus or minus sign in the equation depends on the instantaneous direction of rotation, which was shown could be determined previously.

$$n = \text{floor}(\frac{f_{is\_avg}}{f_{samp}} \pm \frac{1}{2}) \tag{6.5}$$

Therefore, by computing the average instantaneous angular velocity, an estimated excession correction factor can be obtained, which allows for phase excursions greater than $\pm 2\pi$. While this approach could be implemented to provide a dynamic range increase, a simplified and more robust technique has been developed, which is now presented.

6.4 Dynamic Range Extension

Information obtained from the instantaneous carrier frequency can be used in a variety of ways to provide a high-end dynamic range increase. One approach was already presented. However, since the instantaneous direction of rotation and the instantaneous angular velocity are derived from the instantaneous carrier frequency, the excession correction factors can be determined directly from the carrier frequency. That is the approach taken within this dissertation.

6.4.1 Excession Threshold Frequencies

It has been stated previously that an excession will occur if the fringe rate of a signal, also known as the angular velocity, is greater than that of the demodulator. This was shown in Chapter 4 to happen at a fringe rate equal to $\pm\pi f_{samp}$. This peak fringe rate of the demodulator can be converted to an equivalent frequency by dividing by 2π. Thus, the first excession of the demodulator will occur when the instantaneous carrier frequency deviates from the nominal frequency by $\pm\frac{f_{samp}}{2}$. It has also been shown that for each additional π increase in the input phase shift, the demodulated output will undergo an apparent phase reversal. The carrier frequencies at which these phase reversals occur are considered the excession threshold frequencies. The excession threshold frequencies can be found from equation 6.6, where f_e is the instantaneous carrier frequency at the excession crossing.

$$f_e(m) = f_c + \frac{m}{2} f_{samp} \qquad \text{for } m = \pm 1, \pm 2, \ldots \tag{6.6}$$

The excession threshold frequencies will be important in determining the appropriate correction factors. They will also help to define the optimal carrier frequencies or frequency bands within the system bandwidth to track.

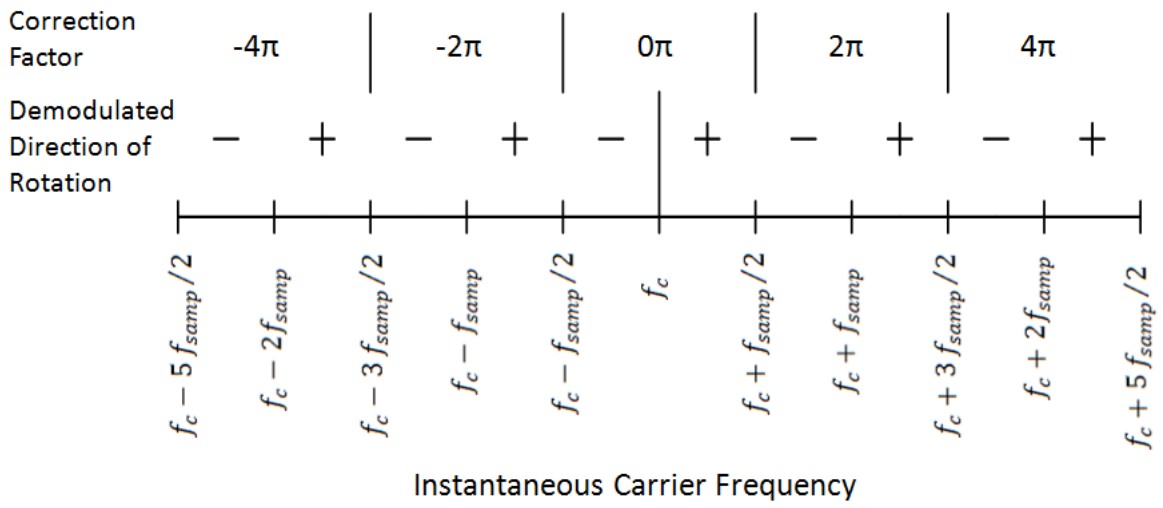

Figure 6.1: Excession threshold frequencies, expected demodulated direction of rotation, and required correction factors

6.4.2 Correction Factor Boundaries

The dynamic range extension approach presented here relies on determining an appropriate correction factor to mitigate excession error offsets. It was discussed at the beginning of this chapter that following the first excession point, a 2π correction factor was needed to correct for the demodulator output phase reversal. Following the second excession point, a 2π offset was needed to account for the full cycle phase wrap. A 4π correction factor was needed after both the third and fourth excession points. This pattern of increasing the correction factor by 2π continues for every two excession threshold frequencies crossed by the instantaneous carrier frequency. Figure 6.1 shows the carrier spectrum of an interferometer system. Included in the figure are the excession threshold frequencies, the correction factors and boundaries, and the demodulated direction of rotation.

The general approach to dynamic range extension is to select the correction factor based on where the measured instantaneous carrier frequency falls within the system spectrum. However, there are three additional considerations which will be addressed that can be used to improve the selection. These include the statistical likelihood of the demodulated direction of rotation, the frequencies that are tracked, and the frequency averaging approach. These issues are now presented.

6.4.3 Maximum and Minimum Likelihood of Demodulated Rotational Direction

When the input phase signal to the demodulator is near zero, the demodulated output will be a low level of phase noise centered around ± 0 radians, and the instantaneous carrier frequency will remain close to the nominal value f_c. Under these conditions, the probability that the demodulator will experience a small positive rotation is equally likely to it experiencing a small negative rotation. If, however, a large phase signal is applied to the input, the likelihood of experiencing either a positive rotation or a negative rotation will no longer be equal when considering a small portion of the waveform. For example, with sinusoidal modulation, during the positive slopes of the waveform, the probability is highest for a positive rotation. On the negative slopes of the waveform, the probability will be highest for a negative rotation. At the maximum and minimum points of the waveform, the probabilities are again equal.

What is of real interest is not the actual rotational probabilities of the waveform, but rather the probability of the demodulated output direction of rotation. Again, with no input signal to the demodulator, the demodulator is equally likely to produce an output with either a positive or negative direction of rotation. If, however, sinusoidal modulation is considered, as the phase between demodulated points begins to increase in the positive direction, the probability of the demodulator producing a demodulated output with a positive direction of rotation also begins to increase. This likelihood continues to increase until the phase shifts between samples reaches $\frac{\pi}{2}$ radians. This is the first maximum likelihood point of demodulated positive rotation. If the phase continues to increase further in the positive direction, the probability will begin to decline until it, again, reaches an equal likelihood at a phase shift of π radians. This is at the first excession threshold point of the demodulator. As a result, even though the actual direction of rotation was in the positive direction, if the phase shift is just slightly greater than π, the demodulator will produce an output value approaching $-\pi$. Therefore, at the excession threshold frequencies, where the demodulated output phase reversals occur, the probability of the demodulator producing an output of positive direction is equally likely as a negative one.

Beyond the first excession threshold, if the input phase advances continue to increase in the

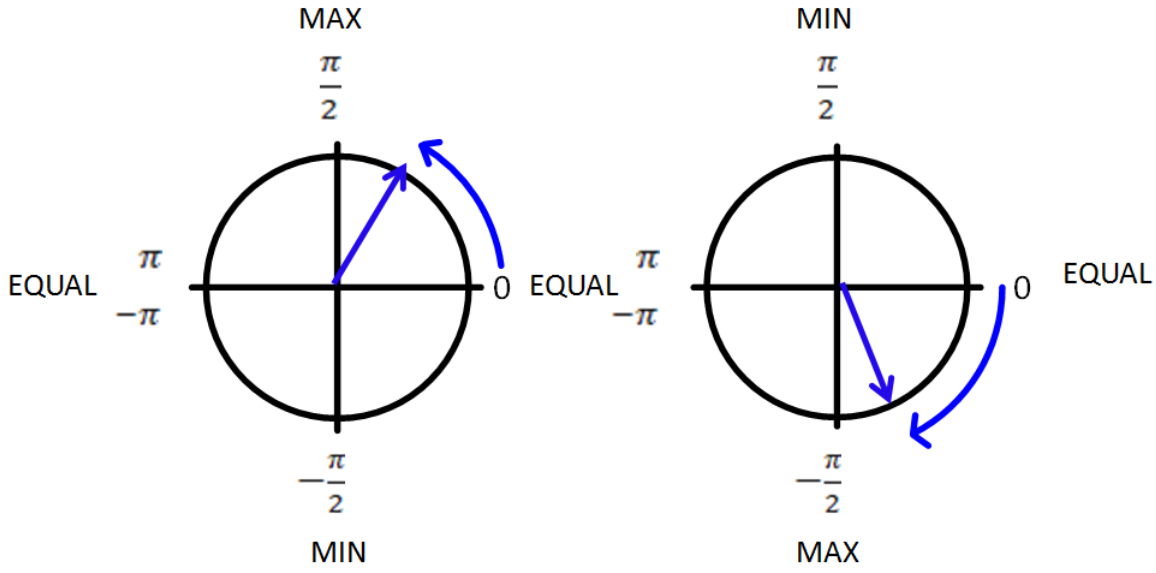

Figure 6.2: Probability of demodulated output direction of rotation given actual direction of rotation

positive direction, the probability of the demodulator producing a positive value will continue to decrease until it hits the positive rotation minimum likelihood point at a positive phase advance of $\frac{3\pi}{2}$. This is the point at which the demodulator is most likely to interpret this positive phase rotation as a negative rotation of $-\frac{\pi}{2}$. Additional increases in the positive rotational phase advances will see the probability of the demodulator producing a positive rotational value begin to increase. As the positive phase advances approach 2π, the probabilities will again be equal at the second excession threshold. This pattern of maximum and minimum likelihood of demodulated rotational direction will continue to repeat for further phase increases in the given direction. A similar analysis could be conducted for the case of the negative rotational direction. The difference between the two cases is in where the maximum and minimum probabilities occur. The points of equal probability are the same for both cases and are located at the excession threshold frequencies. Figure 6.2 shows the expected direction of the demodulated output for both positive and negative rotation.

The points of equal probability were stated as occurring at the excession threshold frequencies. Likewise, the signal fringe rates that equate to the maximum and minimum probabilities can also be converted to equivalent instantaneous carrier frequency values by dividing by 2π.

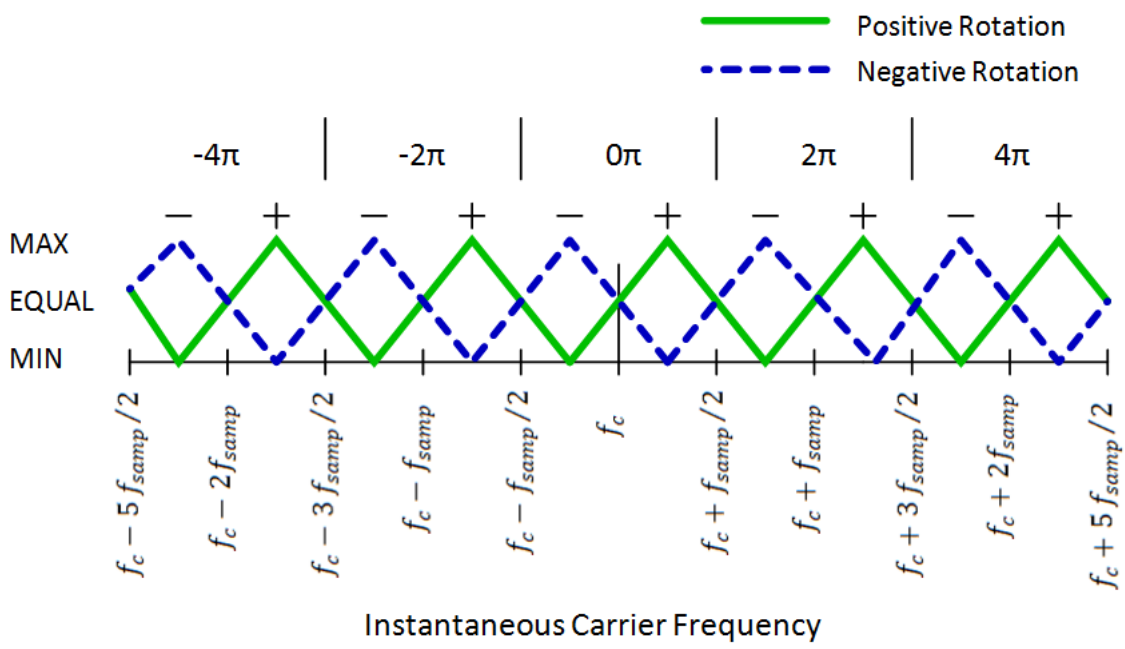

Figure 6.3: Excession correction factor boundaries with maximum and minimum likelihood demodulated directions of rotation

These frequencies can then be overlaid with the correction factor boundaries shown previously in Figure 6.1. The result is Figure 6.3. As can be seen, the maximum and minimum likelihood points occur at frequencies between the excession threshold frequencies. It can also be seen that from one maximum to the next, or from one minimum to the next, for a given rotational direction, the total bandwidth is twice the bandwidth between excession threshold frequencies. This increase in bandwidth will be useful for reducing ambiguity in selecting the appropriate correction factor when the demodulated output direction of rotation is in one direction, but the measured instantaneous carrier frequency falls between excession threshold frequencies where the expected direction of rotation is opposite. Both the maximum and minimum likelihood frequencies are, therefore, useful in helping to establish the correction factor bands and in determining the optimal frequencies within the system bandwidth to track.

6.4.4 Determination of Tracking Frequencies

It was stated previously that only select frequencies within the spectrum of the system must be measured. Which frequencies or frequency bands should be tracked is dependent on the

frequency tracking method itself. There are two primary types of frequency tracking methods: those with continuous tracking ranges and those which track discrete frequencies.

The DIFM approach is an example of a frequency discrimination method with a continuous tracking range. The y_{out} value of the DIFM receiver can range in value between ± 1. The magnitude of the output is directly related to the instantaneous carrier frequency and, as such, can be used to track any frequency within the designed bandwidth of the receiver. For frequency tracking methods that have continuous output ranges, the dynamic range extension approach will place the measured frequency into one of a number of designated frequency bands, which relate to specific correction factors. These bands are generally established by the excession threshold frequencies. The DIFM dynamic range extension approach presented later in the chapter uses two specific sets of frequency bands. One set is used for determining the correction factor given a positive rotation demodulated output, while the other is used for a negative rotation demodulated output. The positive rotation frequency bands are established between the positive rotation minimum likelihood frequencies. The negative rotation frequency bands are established between the negative rotation minimum likelihood frequencies. This method of establishing the correction factor boundaries based on the demodulated output direction increases the effective bandwidth of the correction factor bands by a factor of two over using the excession threshold frequencies alone. Other continuous output tracking methods, such as PECM, would also follow this same approach in selecting tracking frequencies.

The minimum likelihood frequencies, for both positive and negative rotation, can be determined from equations 6.7 and 6.8. These frequencies can then be translated to specific DIFM y_{out} values to be used directly in the dynamic range extension process.

$$f_p(m) = f_c - \frac{f_{samp}}{4} + m f_{samp} \qquad \text{for } m = 0, \pm 1, \pm 2, \ldots \tag{6.7}$$

$$f_n(m) = f_c - \frac{3}{4} f_{samp} + m f_{samp} \qquad \text{for } m = 0, \pm 1, \pm 2, \ldots \tag{6.8}$$

The DFT frequency measurement approach tracks discrete frequencies. With this approach,

the Fourier coefficients of the specific frequencies are measured and compared to one another. The largest coefficient is selected as the instantaneous carrier frequency, determining which excession correction factor is selected. Like the DIFM approach, two sets of frequencies will still need to be monitored. Which one will be used, again, depends on the demodulated output direction of rotation. For positive rotation demodulated output values, the DFT frequencies that must be tracked are those at the maximum likelihood positive rotation locations. Likewise, the negative set of frequencies to be tracked are those at the maximum likelihood negative rotation direction locations. This is done to increase the bandwidth of the correction factor selection bands.

With the DFT method, the number of Fourier coefficients that must be computed is determined by the bandwidth requirement of the dynamic range extension approach and the sampling rate of the system. The frequencies defining the positive and negative bands can be determined from equations 6.9 and 6.10.

$$f_p(m) = f_c + \frac{f_{samp}}{4} + m f_{samp} \qquad \text{for } m = 0, \pm 1, \pm 2, \ldots \tag{6.9}$$

$$f_n(m) = f_c - \frac{f_{samp}}{4} + m f_{samp} \qquad \text{for } m = 0, \pm 1, \pm 2, \ldots \tag{6.10}$$

6.4.5 Frequency Averaging

Selecting the correction factor based solely on the location of the instantaneous carrier frequency within the spectrum will lead to a high error rate. The measured instantaneous carrier frequency only provides the angular velocity at the time of the current demodulation sample point. It does not account for the angular velocity changes that have occurred since the previous demodulation point. For high fringe rate signals, the change in angular velocity between points can be significant. In particular, the minimums, maximums, and inflection points of sinusoidal signals can all be problematic. Such errors, however, can largely be mitigated by considering the instantaneous frequency or angular velocity at the previous demodulation point.

A two-point, equally-weighted, instantaneous carrier frequency average has been determined to substantially reduce potential errors in correction factor selection. There is, however, a frequency dependency that must be considered. As the frequency of the input signal increases, the number of demodulation samples per cycle is reduced. If the number of samples becomes too few, then averaging will fail to determine an accurate averaged angular velocity, and the selected correction factor will likely be in error. It will be shown later in the chapter that for full dynamic range extension, a minimum of 8-12 samples per sinusoidal cycle are required, depending on the frequency measurement technique utilized. A reduced dynamic range extension is possible with fewer data points.

More complex averaging techniques may provide improved angular velocity tracking capabilities. However, these were not explored as part of this dissertation since the two point average provided very good results. Potential improvements include multipoint and weighted averages. One high potential approach is a weighted three-point average that utilizes the previous, the current, and the following demodulation points. This would require delaying the correction factor selection by one demodulation point but could be easily achieved. Such an approach would likely handle higher fringe rate inflection points.

6.4.6 Correction Factor Selection

Selection of the appropriate excession correction factor requires determining the demodulated output direction of rotation and the location of where the averaged instantaneous carrier frequency falls within the system bandwidth. However, how this information is used varies depending on the frequency measurement approach. The specifics of determining the appropriate correction factor, for both the DIFM and the DFT methods, are now provided.

6.5 Dynamic Range Extension Via DIFM

Dynamic range extension via DIFM frequency tracking will be shown to be an efficient and effective technique. Proper selection of the excession correction factor requires two pieces of

information: the demodulated output direction of rotation and the averaged instantaneous carrier frequency. The demodulated output direction of rotation is used to narrow down the potential locations of the correction factor and increase the bandwidth of the measurement frequency bands by a factor of two. If the demodulated output direction of rotation is positive, then the location of the averaged instantaneous carrier frequency will be determined relative to the minimum likelihood positive rotation frequency bands. Likewise, if the direction of rotation is negative, then the location will be determined relative to the minimum likelihood negative rotation frequency bands. The frequency band in which the carrier falls will determine the excession correction factor. The correction factor bands, along with the maximum and minimum likelihood frequencies, were provided earlier in Figure 6.3.

6.5.1 Implementation

The DIFM receiver used in the following simulations is the same as presented in Chapter 5. The output y_{out} was designed to be linear over a bandwidth of $B_{if} = 6.4$ MHz and facilitate a minimum 20 dB dynamic range increase. Values of y_{out} were calculated for both the positive and negative minimum likelihood frequencies. These values are provided in the following simulations. The simulations utilize an if-else comparative statement to determine within which band the averaged instantaneous carrier falls. The hardware implementation utilizes a similar approach.

6.5.2 Simulations

The system parameters of the following simulations were configured to match the demodulation hardware used in the experimental portion of this dissertation. These values are the same as presented in the last chapter; however, they are now repeated for convenience: $f_c = 10$ MHz, $f_{adc} = 100$ MHz, and $f_{samp} = 655360$ Hz.

The MATLAB code used in the selecting the correction factor is provided below, where $phase\_diff$ is the demodulated phase output and $DIFM\_avg$ is the averaged instantaneous carrier value of y_out.

Listing 6.1: DIFM MATLAB simulation correction factor selection code

```
if (phase_diff < 0)   % Negative demodulated phase rotation
      if DIFM_avg < -.792
        phase_cf = 12*pi;
      elseif DIFM_avg < -.722
        phase_cf = 10*pi;
      elseif DIFM_avg < -.638
        phase_cf = 8*pi;
      elseif DIFM_avg < -.544
        phase_cf = 6*pi;
      elseif DIFM_avg < -.441
        phase_cf = 4*pi;
      elseif DIFM_avg < -.330
        phase_cf = 2*pi;
      elseif DIFM_avg < -.215
        phase_cf = 0*pi;
      elseif DIFM_avg < -.096
        phase_cf = -2*pi;
      elseif DIFM_avg < .023
        phase_cf = -4*pi;
      elseif DIFM_avg < .140
        phase_cf = -6*pi;
      elseif DIFM_avg < .253
        phase_cf = -8*pi;
      elseif DIFM_avg < .361
        phase_cf = -10*pi;
      else
        phase_cf = -12*pi;
      endif;
    else % Positive demodulated phase rotation
      if DIFM_avg < -.825
        phase_cf = 12*pi;
```

```
    elseif DIFM_avg < -.759
      phase_cf = 10*pi;
    elseif DIFM_avg < -.682
      phase_cf = 8*pi;
    elseif DIFM_avg < -.593
      phase_cf = 6*pi;
    elseif DIFM_avg < -.494
      phase_cf = 4*pi;
    elseif DIFM_avg < -.386
      phase_cf = 2*pi;
    elseif DIFM_avg < -.273
      phase_cf = 0*pi;
    elseif DIFM_avg < -.156
      phase_cf = -2*pi;
    elseif DIFM_avg < -.036
      phase_cf = -4*pi;
    elseif DIFM_avg < .082
      phase_cf = -6*pi;
    elseif DIFM_avg < .197
      phase_cf = -8*pi;
    elseif DIFM_avg < .308
      phase_cf = -10*pi;
    else
      phase_cf = -12*pi;
    endif;
  endif;
```

One concern of the dynamic range extension approach is the possibility that it may itself introduce errors in the demodulated output. Therefore, the first dynamic range extension simulation conducted was a carrier noise floor analysis. Figure 6.4 shows the results for a zero input radian signal and a typical interferometer CNR of 40 dB. The figure shows that the low level of noise in y_{out} does not introduce errors in the output of the demodulator. Such errors

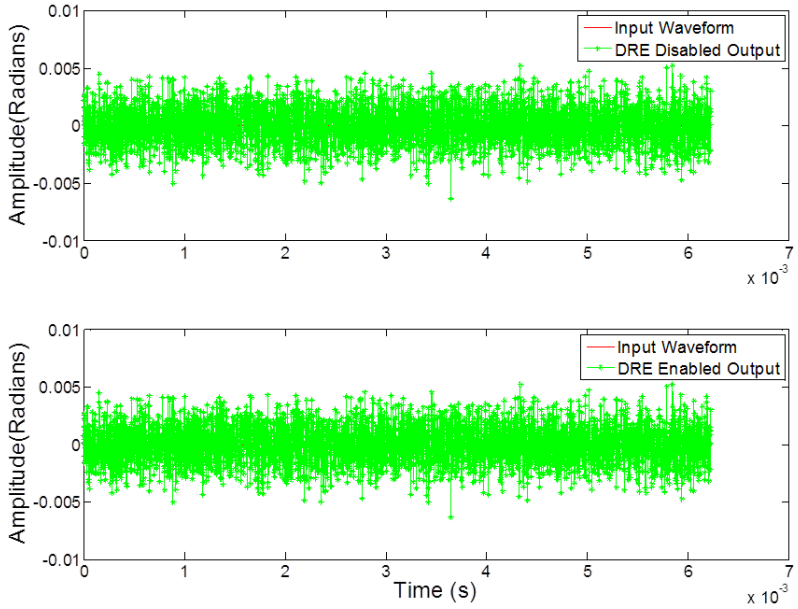

Figure 6.4: Simulated DIFM DRE with $A_s = 0$ radians and CNR = 40 dB

would appear as random 2π shifts in the data.

A second carrier noise floor test was conducted with a CNR of 20 dB. Figure 6.5 confirms the results of the DIFM simulations presented in the last chapter, as no errors are introduced.

Reducing the CNR to 12 dB, as in Figure 6.6, demonstrates the potential errors that can be introduced if the CNR drops low enough.This should not occur in most interferometric systems. However, in systems which do not implement some form of polarization fading mitigation, it is recommended that the dynamic range extension corrections be disabled when the CNR drops below a given level.

The next three simulations were conducted using the three waveforms tested (1 kHz, 10 kHz, and 100 kHz) in the previous chapter. These waveforms test the dynamic range extension approach over a bandwidth of 6.4 MHz. Each test represents a 20 dB dynamic range extension at the given frequency.

The results of the first simulation are shown in Figure 6.7. The input waveform consists of a

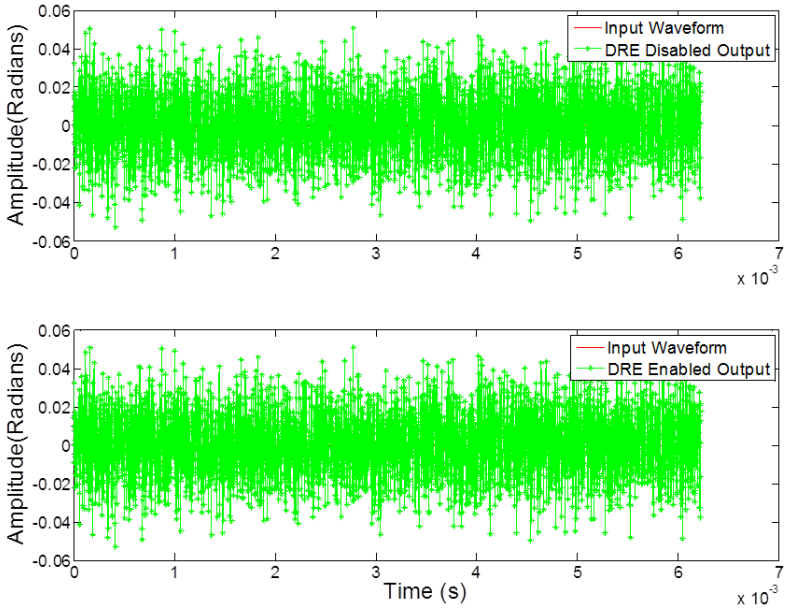

Figure 6.5: Simulated DIFM DRE with $A_s = 0$ radians and CNR = 20 dB

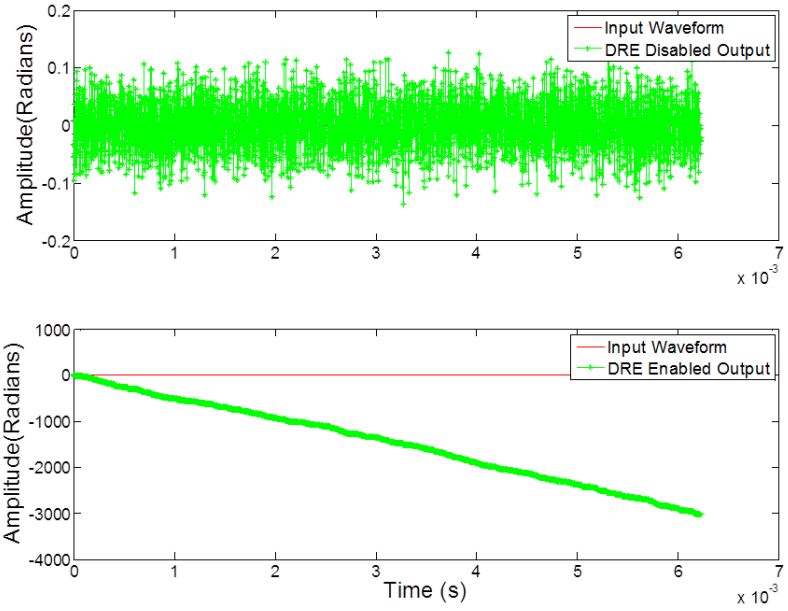

Figure 6.6: Simulated DIFM DRE with $A_s = 0$ radians and CNR = 12 dB

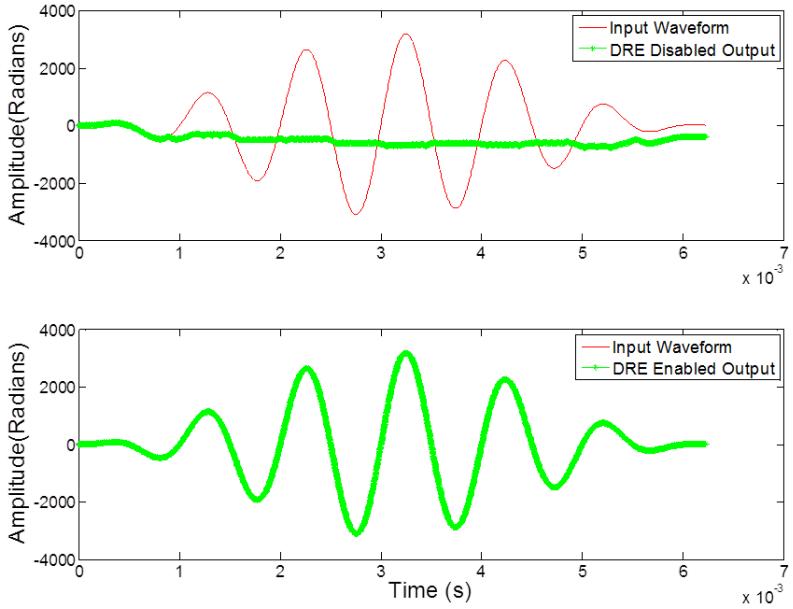

Figure 6.7: Simulated DIFM DRE with $A_s = 3200$ radians, $f_s = 1$ kHz, and CNR = 40 dB

Hanning-weighted 3200 radian sinusoid at 1 kHz. The top plot of the figure shows the demodulated output without the dynamic range extension correction factors added in. As can be seen, without the excession correction factors, the demodulated output quickly loses the ability to track the input waveform, and the final output at the end of waveform is significantly off. However, with the dynamic range extension correction factors added in, the demodulated output is able to correctly track the input waveform. This confirms the ability of the presented approach to successfully extend the dynamic range.

The second waveform test consists of a 320 radian sinusoid at 10 kHz. The results are the same as the previous test. Without the correction factors added in, the demodulated output quickly loses track of the input waveform. With them added in, the demodulator is able to successfully recover the input waveform without any errors. This is shown in Figure 6.8.

The third simulation was conducted with a 32 radian 100 kHz sinusoid. The results of this test are not as successful as the two previous ones. It can be seen from Figure 6.9 that while the dynamic range extended demodulated output initially tracks the input waveform better than the non-extended output, it too loses track at some point. This leads to the large offset at the

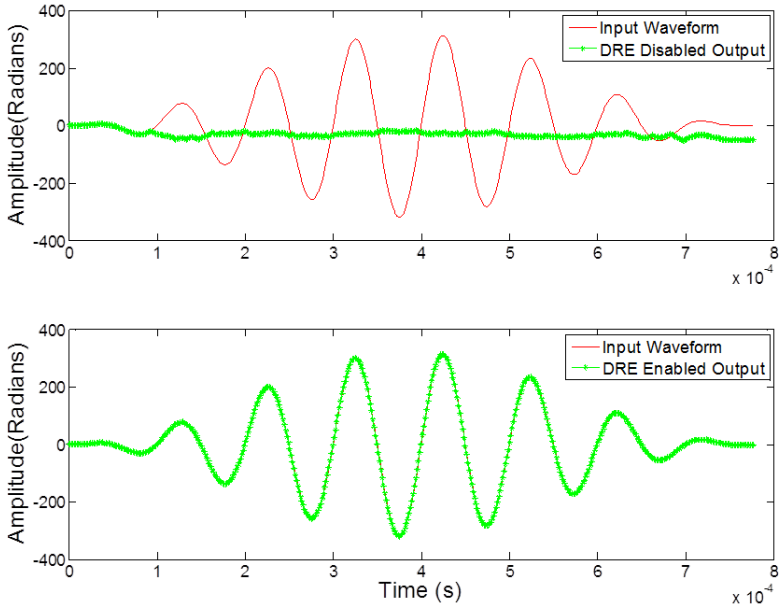

Figure 6.8: Simulated DIFM DRE with $A_s = 320$ radians, $f_s = 10$ kHz, and CNR = 40 dB

end of the waveform. Even though the peak bandwidth of the signal was the same as the previous two simulations, the high frequency signal failed to be correctly demodulated. This demonstrates a limitation of the dynamic range extension approach, a frequency dependence related to f_{samp} of the input waveform. This limitation will be addressed later.

The last two types of simulations conducted were designed to test the dynamic range extension's susceptibility to broadband noise input signals. There are two primary concerns with broadband noise. First, how will the dynamic range extension approach handle high levels of broadband noise? Second, how will it impact the demodulation of other high fringe rate signals such as sinusoids?

The first broadband noise simulations conducted were designed to test the peak levels that could be handled by the dynamic range extension approach. The noise was shaped to have a sharp roll-off between 10 kHz and 50 kHz. This was done to give the noise a more realistic shape when compared to actual physical systems. Simulations were first conducted to test the level of noise at which non-dynamic range extended output would fail to correctly track the input waveform. Once this level was established, simulations were then conducted to test the

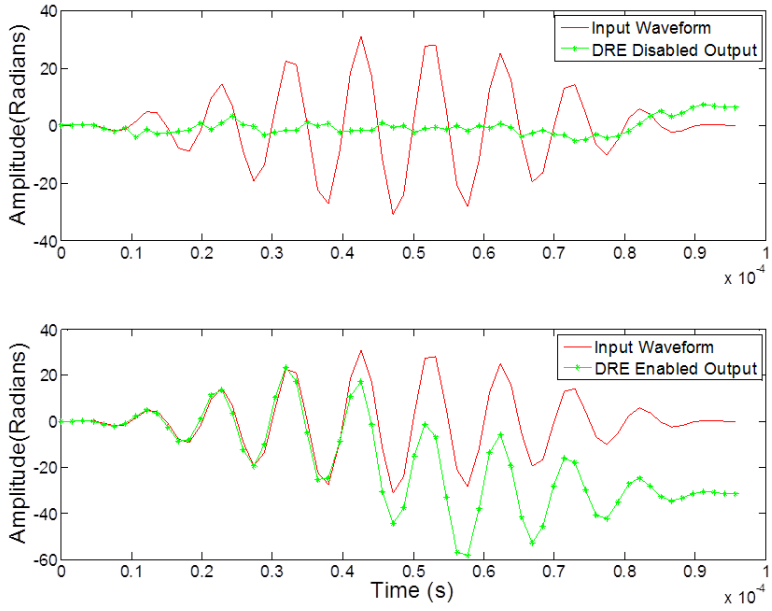

Figure 6.9: Simulated DIFM DRE with $A_s = 32$ radians, $f_s = 100$ kHz, and CNR = 40 dB

peak levels of noise that could be properly demodulated with the dynamic range extension correction factors enabled. The dynamic range extension capability for broadband noise was found to just exceed 20 dB. The results of one of the dynamic range extended broadband noise tests are provided in Figure 6.10.

The second set of broadband noise tests were designed to test the impact of the noise on the demodulation of other high fringe rate signals. The noise for these simulations was, again, designed to have a passband frequency of 10 kHz and a stopband of 50 kHz. Previous simulations have shown that a peak sinusoid of 320 radians at 10 kHz could properly be demodulated with the dynamic range extension approach. Likewise, the analysis provided in Chapter 4 of the impact of broadband noise on sinusoidal modulation showed that for a 6 dB reduction in the peak sinusoid, an equal level of broadband noise could be tolerated. Therefore, the simulations were conducted with both the sinusoid and noise reduced by 6 db from their maximum amplitudes. The results of one of these simulations is provided in Figure 6.11. As can be seen from the figure, the dynamic range extension approach is able accurately track the input waveform without any resulting offsets. The results of this and the previous noise test confirms that the impact of broadband noise on the dynamic range extension

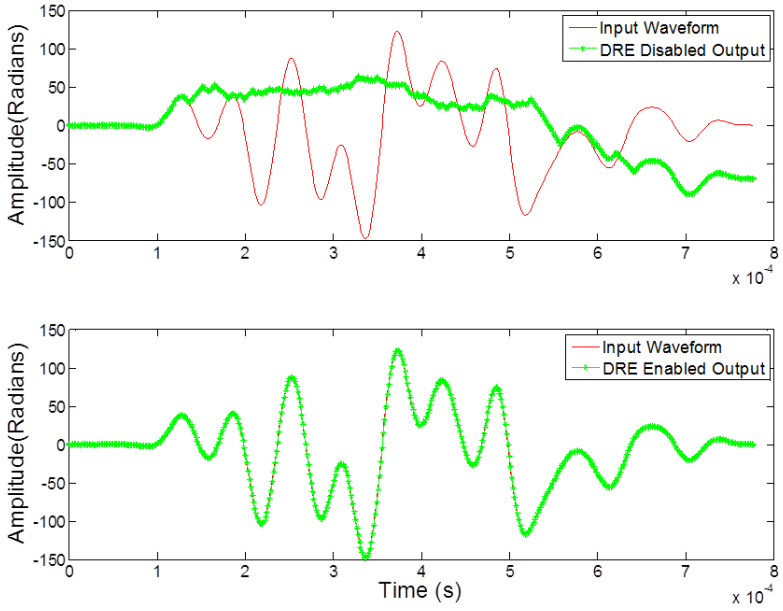

Figure 6.10: Simulated DIFM DRE with BBN(shaped) = 22000 radians and CNR = 40 dB

approach are minimal at best. These results also confirm the broadband fringe rate analysis provided in Chapter 4.

6.5.3 Limitations

There are a few limitations to the DIFM dynamic range extension approach. The primary limitation is the maximum bandwidth which can be tracked by the DIFM receiver, limiting the overall dynamic range increase that can be obtained. This issue was addressed previously in Chapter 5. However, one other issue was identified in the preceding simulations. Of the three sinusoidal waveforms tested, only the waveforms at 1 kHz and 10 kHz were successfully demodulated. The dynamic range extension approach failed to properly demodulate the waveform at 100 kHz despite the fact that all three waveforms had the same total bandwidth. This suggests that there is a frequency dependence to the dynamic range extension method.

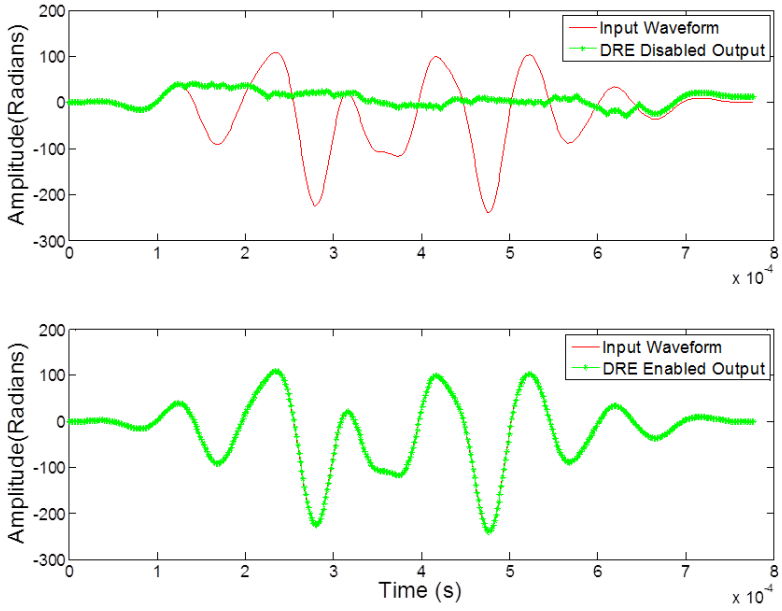

Figure 6.11: Simulated DIFM DRE with BBN(shaped) = 11000 radians, A_s = 160 radians, f_s = 10 kHz, and CNR = 40 dB

Frequency Dependence

The dynamic range extension technique was shown in Figure 6.9 to not properly determine the appropriate correction factors for a waveform at 100 kHz. With a 100 kHz waveform and f_{samp} = 655360 Hz, only 6.5 samples of the waveform are obtained per cycle. Given these few points and given that these points are then averaged, it is difficult for the dynamic range extension approach to calculate the actual correction factors at the non-linear parts of the input waveform. It has been determined, primarily through simulations, that to correctly demodulate the input waveform with a high reliability, a minimum of 11-12 samples per waveform is required for the DIFM method. Figure 6.12 shows that a full 20 dB dynamic range increase can be obtained for a sinusoidal waveform at 60 kHz.

While the full dynamic range increase requires a minimum 11-12 samples per waveform, some increase can be obtained with fewer points. Figure 6.13 shows the results for a sinusoid at $\frac{fsamp}{4}$. Even at this high a frequency, a dynamic range increase of 8 dB is achieved.

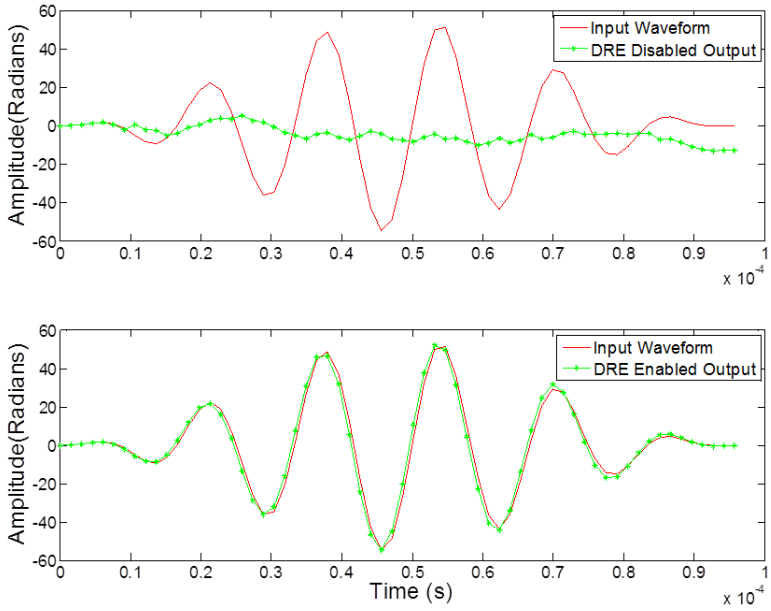

Figure 6.12: Simulated DIFM DRE with $A_s = 55$ radians, $f_s = 60$ kHz, and CNR = 40 dB

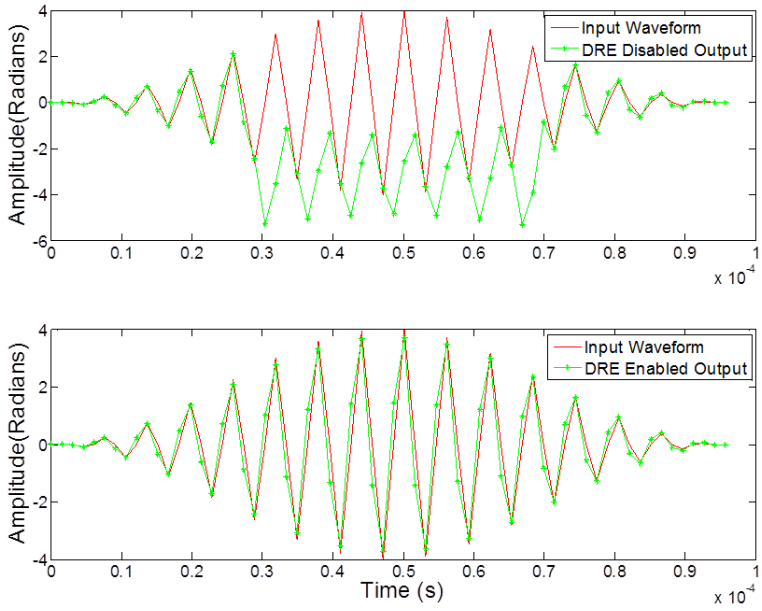

Figure 6.13: Simulated DIFM DRE with $A_s = 4$ radians, $f_s = 164$ kHz, and CNR = 40 dB

Despite the apparent frequency dependence of the dynamic range approach, this will not generally be an issue. For the application at hand, after f_{samp} has been filter decimated down to the desired output rate of 81920 Hz, the full dynamic range extended bandwidth will still be greater than the Nyquist frequency. Even for systems which are not oversampled, a minimum number of samples per waveform are generally required such that the data is not acquired at or near the Nyquist rate. As such, the frequency dependency should not be a limiting factor.

6.5.4 DIFM Summary

The DIFM dynamic range extension method was just shown to provide a more than 20 dB dynamic range increase. The approach required determining the demodulated direction of rotation and the averaged instantaneous carrier frequency. From these two pieces of information, an excession correction factor could be determined which was added to the standard demodulated output. This technique was successfully demonstrated through various simulations. While a high frequency waveform limitation was identified, it should not be an issue for most practical systems. As a result, the DIFM dynamic range extension approach has been demonstrated to successfully provide a 20 dB dynamic range increase, while requiring minimal hardware resources and having few limitations.

6.6 Dynamic Range Extension Via DFT

Dynamic range extension via DFT frequency tracking largely follows that defined earlier for DIFM. Proper selection of the excession correction factor again requires two pieces of information: the demodulated output direction of rotation and the averaged instantaneous carrier frequency. The difference between the two methods is in how the averaged instantaneous carrier frequency is determined. With the DIFM approach, the carrier measurement bands were defined by the minimum likelihood frequencies. With DFT, the instantaneous carrier frequency is determined by measuring the DFT coefficients at the maximum likelihood frequencies. The previous and current measurements are averaged

together to provide an averaged instantaneous carrier frequency. The DFT frequency with the largest averaged coefficient is then used to select the appropriate correction factor.

6.6.1 Implementation

The DFT implementation used in the following simulations is the same as that presented in Chapter 5. A total of 22 frequencies are used to track the instantaneous carrier frequency over a bandwidth of 6.4 MHz. Eleven of the 22 frequencies measure the carrier frequencies where the expected demodulated output direction of rotation is positive; the other 11 frequencies measured are where the expected demodulated output direction of rotation is negative. The tracking of both the positive and negative directions of rotation is, again, done to reduce potential ambiguity when the demodulated direction of rotation is in one direction, but the averaged instantaneous carrier falls at a contradictory location. It also provides a doubling of the bandwidth in which the appropriate correction factor can be selected from.

6.6.2 Simulations

As previously, the system parameters for the following simulations were designed to match the demodulation hardware used in the experimental portion of this dissertation. These values are the same as presented in the last chapter and the preceding simulations.

The MATLAB code used in the selecting the correction factor is provided below, where $phase\_diff$ is the demodulated phase output, p_lst is the list of expected positive rotation frequency coefficients, and n_lst is the list of expected negative rotation frequency coefficients.

Listing 6.2: DFT MATLAB simulation correction factor selection code

```
%Determine direction of rotation and select
%peak DFT coeff from appropriate list
if ( phase_diff > 0 )
  [max_val,fr_index] = max(p_lst);
```

```
 else
  [max_val,fr_index] = max(n_lst);
end

%Select correction factor
if fr_index == 11
  phase_cf = 10*pi;
elseif fr_index == 10
  phase_cf = 8*pi;
elseif fr_index == 9
  phase_cf = 6*pi;
elseif fr_index == 8
  phase_cf = 4*pi;
elseif fr_index == 7
  phase_cf = 2*pi;
elseif fr_index == 6
  phase_cf = 0*pi;
elseif fr_index == 5
  phase_cf = -2*pi;
elseif fr_index == 4
  phase_cf = -4*pi;
elseif fr_index == 3
  phase_cf = -6*pi;
elseif fr_index == 2
  phase_cf = -8*pi;
else
  phase_cf = -10*pi;
end;
```

It was shown in Chapter 5 that the DFT frequency measurement approach has a substantially higher noise level output, when compared to DIFM, for a given input. As a result, there was a high concern that the DFT approach may itself introduce errors in the demodulated output.

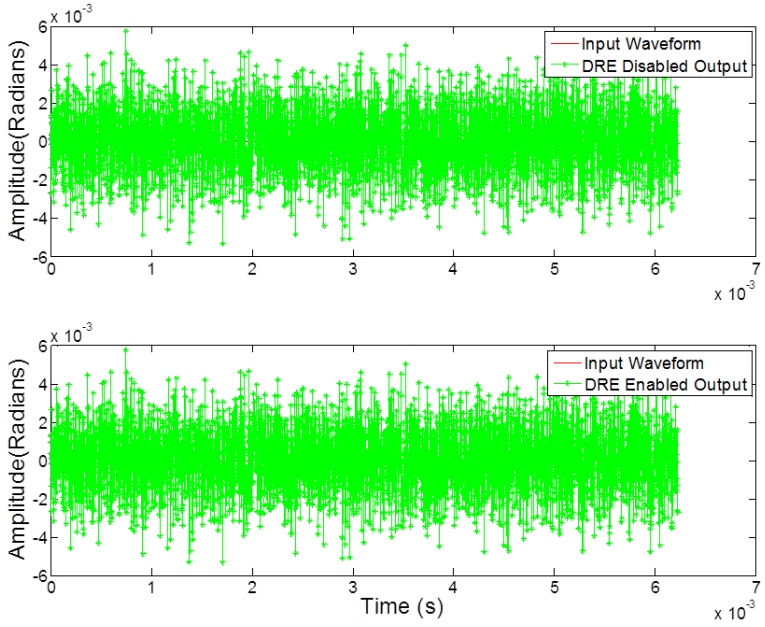

Figure 6.14: Simulated DFT DRE with $A_s = 0$ radians and CNR = 40 dB

Therefore, the first set of DFT dynamic range extension simulations were conducted to evaluate the approach at the different CNR levels tested previously in Chapter 5. The first simulation, shown in Figure 6.14, shows the results for a zero input radian signal at a CNR of 40 dB. The figure shows that despite the visibly high levels of noise in the DFT coefficients, no DC offsets are present in the dynamic range extended output.

Figure 6.15 shows the effects of reducing the CNR to 20 dB. The simulated DFT coefficients were presented previously in Figure 5.20. Even though the magnitude of the noise in both the DFT coefficients and the demodulated has increased by an order of magnitude, surprisingly, no offsets have been introduced in the dynamic range extended outputs.

By reducing the CNR to a level of only 12 dB, the dynamic range extension approach actually begins introducing errors in the demodulated output. This is depicted in Figure 6.16. From the figure, it can be determined that only three errors where introduced over the waveform. This is substantially better than the DIFM approach in which errors were introduced across the entire simulation at this CNR level. However, as stated previously, this will not be an issue for most interferometer systems since a high CNR is required for normal operation. In

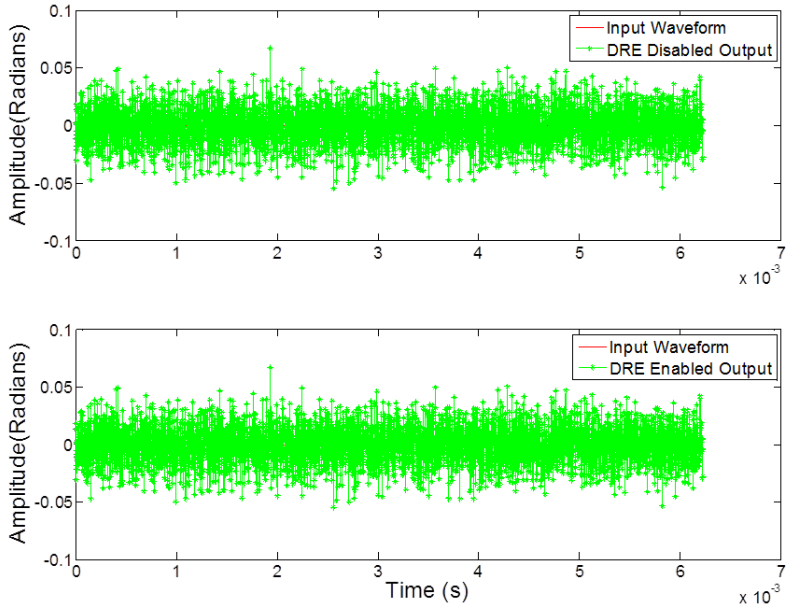

Figure 6.15: Simulated DFT DRE with $A_s = 0$ radians and CNR = 20 dB

the event that the CNR does drop this low, such as in systems without polarization fading mitigation, it is recommended that an option be available for disabling the dynamic range extension correction factors.

The next set of DFT dynamic range extension simulations were conducted using the three waveforms previously identified at 1 kHz, 10 kHz, and 100 kHz. All three waveforms were scaled to demonstrate a 20 dB dynamic range increase. The simulation results of the 1 kHz waveform are shown in Figure 6.17. This figure confirms the ability of the dynamic range extension approach, using DFT as the frequency discrimination method, to correctly recover the input signal. As can be seen in the top of the figure, with the correction factors disabled, the demodulated output quickly loses track of the waveform. However, with the correction factors added in to the output, the input is accurately demodulated.

The simulation results for the waveform testing at 10 kHz is similar. With the dynamic range extension correction factors added in, the waveform is properly tracked. These results are shown in Figure 6.18.

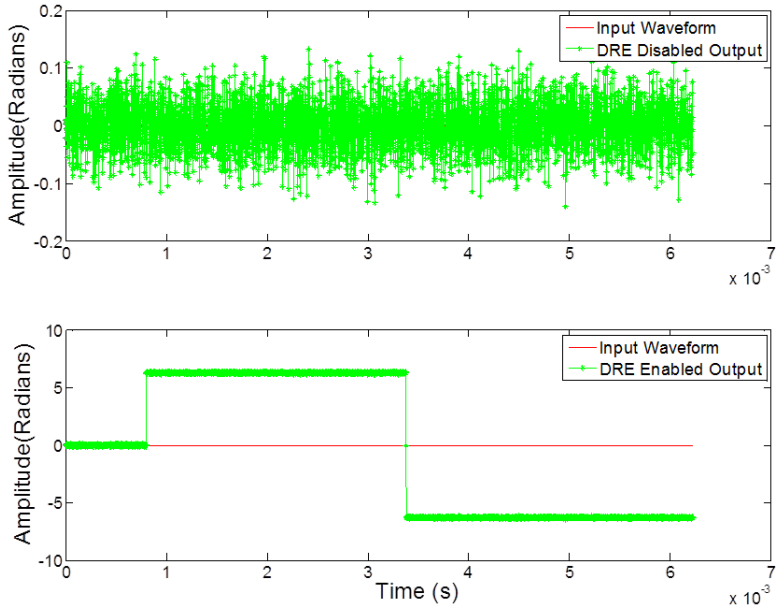

Figure 6.16: Simulated DFT DRE with $A_s = 0$ radians and CNR = 12 dB

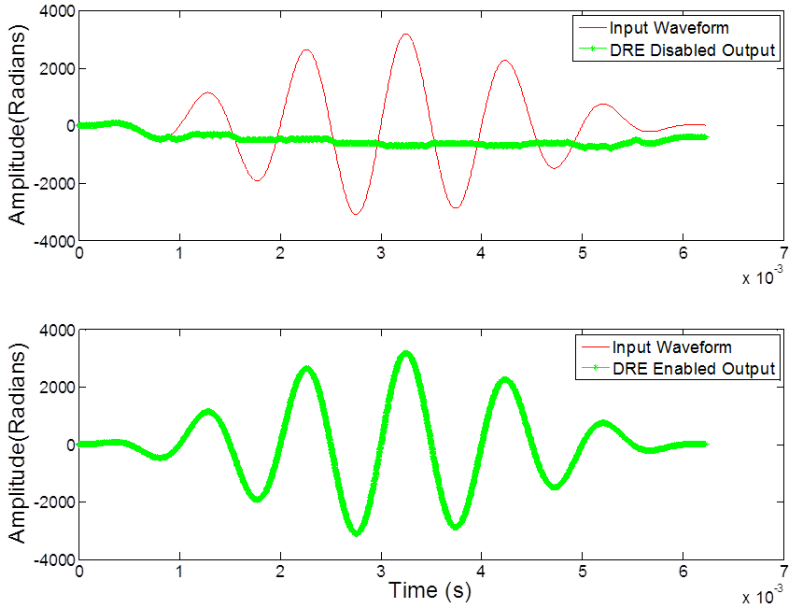

Figure 6.17: Simulated DFT DRE with $A_s = 3200$ radians, $f_s = 1$ kHz, and CNR = 40 dB

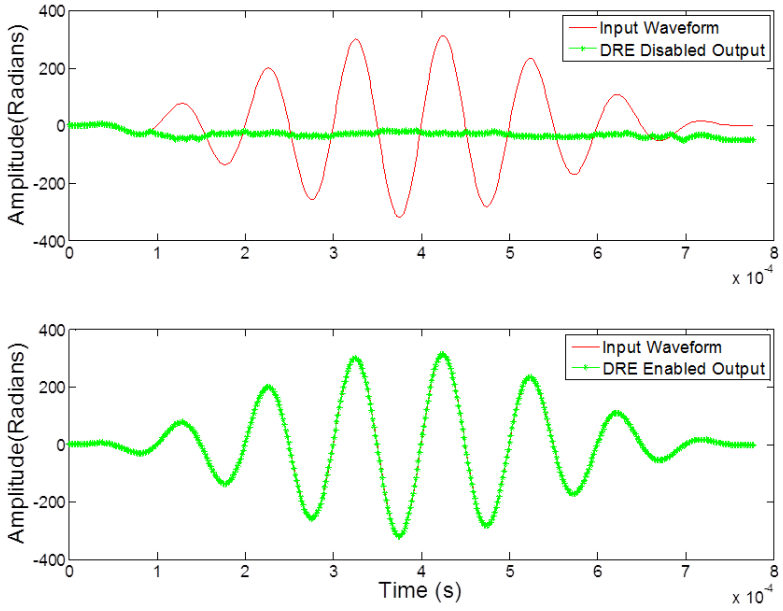

Figure 6.18: Simulated DFT DRE with $A_s = 320$ radians, $f_s = 10$ kHz, and CNR = 40 dB

Much like the simulated waveform tests conducted for the DIFM method, the DFT method fails to properly demodulate the entire input waveform at 100 kHz. This is evident from the results shown in Figure 6.19. However, there are two points of interest regarding this simulation. First, as with the DIFM method, DFT also fails at 100 kHz. This will, again, be shown to be related to a frequency dependency of the dynamic range extension approach itself. The second item of interest is that although both methods fail, the DFT method does a better job at tracking the waveform. The final offset for the DFT output is much less than that of the DIFM. This provides some early indication that the DFT method will provide slightly better results overall when compared to DIFM.

The same concerns exist regarding the impact of broadband noise for the DFT approach as those documented previously for DIFM. The first broadband noise simulation was, therefore, to test the peak levels of noise that could be correctly demodulated by the dynamic range extension approach. Although both the DIFM and DFT methods were designed for a 20 dB dynamic range extension, the DFT method, again, provided slightly better results. These results are displayed in Figure 6.20. Where as the DIFM approach could handle a peak shaped noise input of 22,000 radians, DFT was capable of reliably demodulating levels of

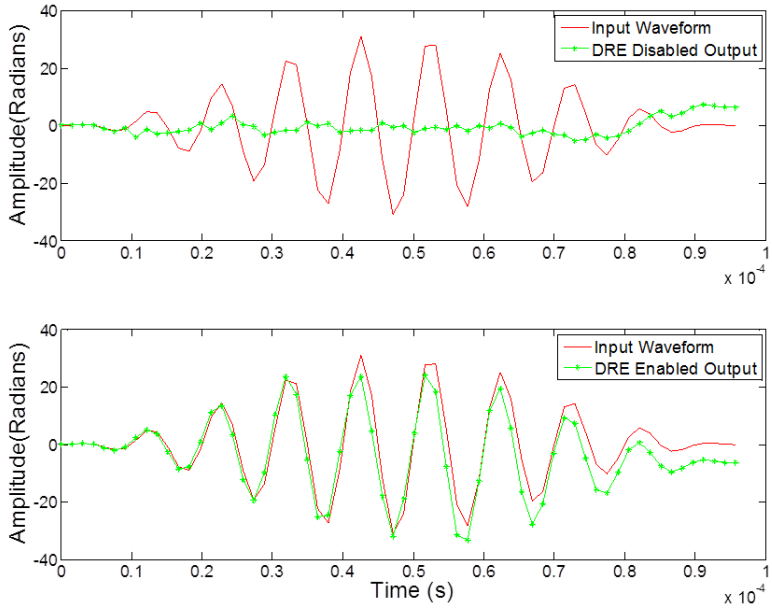

Figure 6.19: Simulated DFT DRE with $A_s = 32$ radians, $f_s = 100$ kHz, and CNR = 40 dB

25,000 radians. In both cases, not only did the broadband noise not negatively impact the dynamic range extension approach, the peak noise levels were shown to be extended by more than the designed 20 dB.

The second broadband noise simulation conducted was to evaluate the impact of the noise on a high fringe rate signal. However, from the results of the similar DIFM test, the impact was believed to be low. The results shown in Figure 6.21 confirm this. The 320 radian peak sinusoid at 10 kHz, tested previously, was reduced by 6 dB and combined with a 6 dB reduced level of broadband noise. For the DFT simulation, this peak level was 12,500 radians, where the noise was shaped the same as in the previous simulations. These results also confirmed that the DFT method, again, had a slight performance edge over the DIFM approach, which could only tolerate a peak noise level of 11,000 radians.

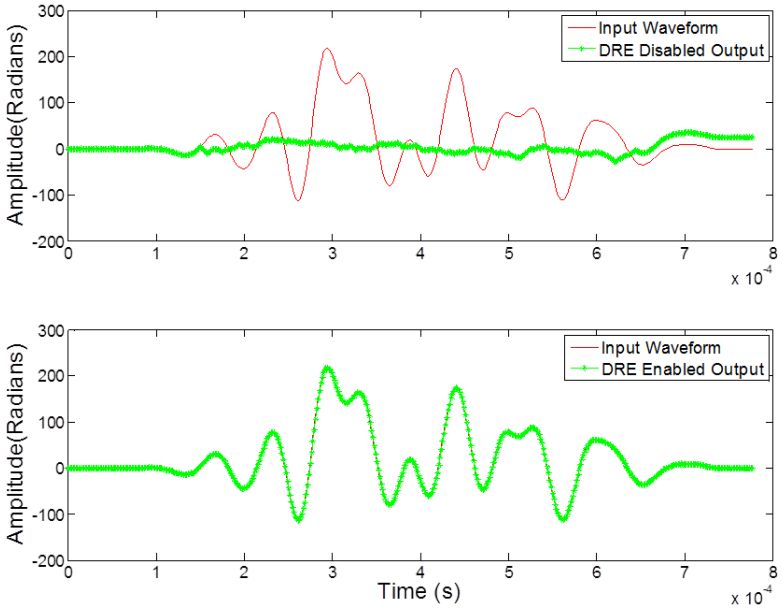

Figure 6.20: Simulated DFT DRE with BBN(shaped) = 25000 radians and CNR = 40 dB

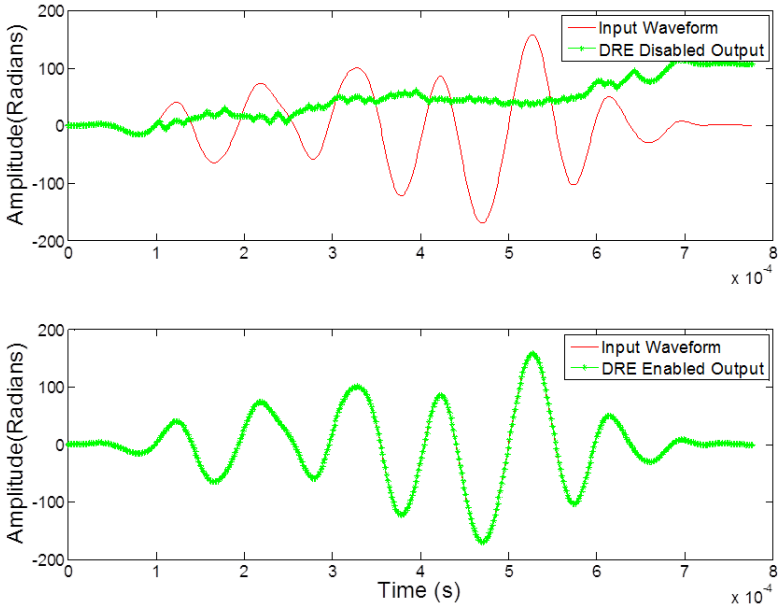

Figure 6.21: Simulated DFT DRE with BBN(shaped) = 12500 radians, A_s = 160 radians, f_s = 10 kHz, and CNR = 40 dB

6.6.3 Limitations

The dynamic range extension approach, using DFT as the frequency discrimination method, suffers from two primary limitations. First, as was shown in the previous simulations, the DFT method experiences the same frequency dependent limitation as was found with DIFM. The second limitation is the amount of hardware resources required. Although this issue was partially addressed in the previous chapter, it will be quantified in a moment.

One additional limitation alluded to earlier was the level of noise present in the DFT coefficients. However, while the relative magnitude of the DFT coefficient noise is substantially higher than that of the DIFM y_{out} output, the simulations have actually shown that the DFT method marginally out performs the other. As such, the apparently high levels of noise impose no actual limitation. The minimal impact of the noise is believed to be related to the fact that the noise is common to all coefficients. Although, why the DFT method performs slightly better than the DIFM is not well understood.

Frequency Dependence

In the DIFM extension simulations, it was shown that a full 20 dB dynamic range increase could be obtained out to a frequency of 60 kHz. A similar round of DFT simulations were conducted to determine the highest frequency that could still achieve the full 20 dB increase. These tests showed that the full increase could be obtained at a frequency of 80 kHz. The results are shown in Figure 6.22. From this, it can be determined that approximately 8-9 samples per waveform cycle are needed for full dynamic range extension. This can be used to estimate the usable frequency range for other f_{samp} rates.

At the maximum dynamic range extended frequency of $\frac{f_{samp}}{4}$, simulations determined that a peak 7 radians could be measured. This is nearly 6 dB higher than the level achieved by the DIFM approach at the same frequency. The 7 radians also equals a nearly 13 dB dynamic range extension at this frequency. Therefore, between 80 kHz and 164 kHz, the maximum dynamic range extension that can be achieved is only reduced by 7 dB. Likewise, this should

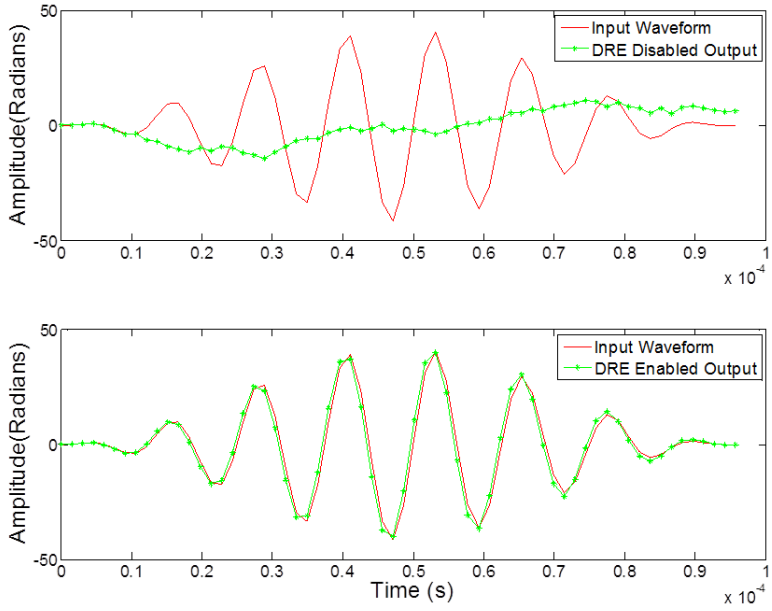

Figure 6.22: Simulated DFT DRE with $A_s = 42$ radians, $f_s = 80$ kHz, and CNR = 40 dB

not be an issue for most interferometric systems where the primary measurement band is typically lower in frequency. It may be a concern where f_{samp} is substantially lower, such as in large scale TDM systems.

Hardware Resources

Each 6 dB increase in dynamic range requires a doubling of the carrier bandwidth. As a result, each 6 dB increase in dynamic range also requires roughly a doubling in the amount of hardware resources to compute the DFT coefficients. Likewise, a doubling of the logic used in selecting the largest coefficient is required. This leads to a limitation of the dynamic range increase that can be achieved based on the available hardware.

The DFT FPGA hardware implementation used within this dissertation was presented in Chapter 5. The DFT computations are performed as integer operations since they require fewer clock cycles than floating-point. The problem with using integer operations, however, is in the number of bits required at each stage for accurate results. For 16 bit integer input data,

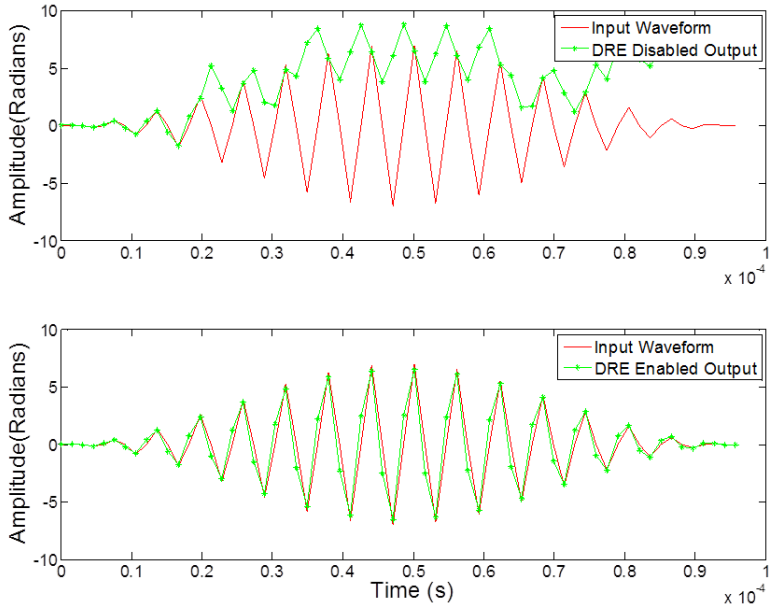

Figure 6.23: Simulated DFT DRE with $A_s = 7$ radians, $f_s = 164$ kHz, and CNR = 40 dB

which is windowed by 16 bits and where the DFT reference waveforms are 16 bit, the required DFT multipliers are 32 x 16 bit. The 48 bit multiplier output is then fed to a summing circuit; the bit size of which is dependent on the total number of samples of the carrier acquired. A 64 x 64 bit secondary multiplier was used to compute the square of each DFT component. Only a single squaring multiplier was required for all frequencies to meet the required data rate. The bit size of the squaring multiplier output is 128. Bit truncation was used to reduce the final DFT coefficient outputs to 64 bits. Although 64 bit processing can be tolerated by most modern programmable logic devices, the required resources are not insignificant.

The DFT processing used within the experimental portion of the dissertation was implemented in an Altera Cyclone V 5CEA7 FPGA device. This is one of the largest FPGAs in the low-cost device family. The standard demodulation process, which includes the I/Q reprocessing, a 160 point FIR low-pass filter, and second order IIR high-pass output filter, required 19% of the total device resources and 38% of the available DSP blocks. With 22 DFT coefficients being processed, the total device resource usage increased to 42%, and 63% of the DSP blocks. Therefore, a 20 dB dynamic range improvement increased the total device usage more than double. This is is the hardware required to process only a single channel.

This makes implementation of more than a single channel in a low-cost device difficult. It also imposes a dynamic range extension limitation in that obtaining a 26 dB increase would be difficult with the resources remaining within the selected device.

6.6.4 DFT Summary

Dynamic range extension via DFT frequency discrimination was just shown to provide a more than 20 dB dynamic range increase. The averaged instantaneous carrier frequency was able to be determined from the largest DFT coefficient. As with the DIFM method, the averaged instantaneous carrier frequency and the demodulated direction of rotation were used to determine an excession correction factor that could be added to the standard demodulated output. Simulations were presented to verify the approach. A high frequency waveform limitation was identified. However, it should, again, not be an issue for most practical systems. A second limitation was shown to be related to the amount of hardware resources required. While a 20 dB extension could be implemented as part of this work, additional increases could not be obtained with the available resources. Regardless of the two limitations, the DIFM dynamic range extension approach has been demonstrated to successfully provide a 20 dB dynamic range increase.

6.7 Summary

Chapter 6 presented a novel approach to dynamic range extension of heterodyne fiber-optic interferometers. It was shown how the deterministic nature of the demodulator excessions could be used to help determine an $n2\pi$ correction factor. By measuring the instantaneous carrier frequency and calculating an average value, the averaged instantaneous frequency could be used to obtain the number of 2π radians that had occurred between demodulation points. It was also shown that determination of the correction factor could be enhanced by using information about the current demodulated direction of rotation. Information about the demodulated direction of rotation allowed for a doubling of the correction factor bin bandwidths and helped to reduce ambiguity in the correction factor selection process.

The dynamic range extension approach was successfully demonstrated using two separate methods of frequency discrimination. Both methods, DIFM and DFT, were able to achieve a 20 dB dynamic range extension under simulated conditions. The DIFM method, however, has an advantage in that the number of hardware resources required is substantially less. Likewise, the DFT method has the advantage regarding a frequency dependent limitation. DFT requires only 8-9 samples of the waveform for full dynamic range extension, where as DIFM requires 12-13. The DFT approach is also capable of handling slightly higher levels of broadband noise. However, both approaches are well suited for dynamic range extension implementations and, as such, will be tested as part of the experimental work of Chapter 7.

Chapter 7 Dynamic Range Extension Experimental Results

Chapter 7 documents the dynamic range extension experimental tests results. These in-water fiber-optic hydrophone tests were designed to verify the theoretical and simulated work presented in the previous chapters. However, equipment and environmental limitations prevented direct comparison in some of the tests. Despite this, both the DIFM and DFT variants of the approach are experimentally validated. Differences between the simulated and experimental results are discussed.

7.1 Test Configuration

A custom-manufactured fiber-optic hydrophone was used as the receiving element for the following in-water tests. The sensor has a high responsivity of 1.6 radians per Pascal and a corner frequency of 20 kHz. Interferometric signals received from the fiber-optic sensor were demodulated using a custom I/Q reprocessing demodulator, implemented in an Altera Cyclone V 5CEA7 FPGA. The dynamic range extension hardware was added within the same device.

Under normal operation, the demodulator streams the processed data out over Ethernet at a rate of 81920 samples per second. However, the interrogation rate of the sensor occurs at an 8x oversample rate of 655360 Hz. The oversampled data is then filter-decimated down and passed through an IIR high-pass filter with a 100 Hz corner frequency. The high-pass filter removes large static offsets that can occur through either temperature changes of the fiber coils or demodulator excessions. The raw, unfiltered data could not be streamed from the demodulator continuously at the oversample rate, as was needed for the experimental testing. Likewise, information such as the DIFM y_{out} value and the DFT coefficients needed to be acquired to fully evaluate both approaches.

The Altera SignalTap-II software was used to collect the necessary data. The SignalTap software allows for implementing an embedded logic analyzer within the FPGA device. Acquired data is stored to memory blocks within the device before being read using one of

Altera's programming dongles and the SignalTap software. This approach allowed for acquisition of all of the necessary pieces of information. However, memory requirements limited the number of DFT coefficients that could be obtained to four.

The high fringe rate acoustic waveforms used for the tests were generated by an International Transducer Corp. ITC-1007 sound source. An Instruments Inc. L40 power amplifier was used to drive the ITC-1007. However, this configuration resulted in several issues. First, the ITC-1007 source has a poor Transmit Voltage Response (TVR) below several kilohertz. Therefore, the transducer would have needed to be driven with a substantial amount of power for the 1 kHz waveform tests. The L40 amplifier and the ITC-1007 transducer both supported the required power levels. However, the available cabling and connectors were only rated at 600 Volts. Testing confirmed that the breakdown voltage was just over 800 Volts, limiting the total amount of power that could be supplied to the transducer. Higher voltage rated cabling and connectors could not be procured in time for these tests. Likewise, a much larger sound source could have been used to improve the TVR at 1 kHz. However, deployment of the different source would have created several new challenges. As a result of these issues, it was decided to move the 1 kHz waveform test to 2.5 kHz. This resulted in an improvement in the TVR and an increase in the fringe rate, such that it could be used to drive the demodulator more than 20 dB past the excession point at that frequency.

A standard RESON TC-4032 hydrophone was used as a reference to determine the actual acoustic signal applied to the fiber-optic sensor. A National Instruments PXIe-4461 card was used to both record the analog signal of the reference hydrophone and generate the analog output waveform. This card has a maximum input and output rate of 204.8 kSPS. However, the card was configured for 163,840 SPS, an integer rate of the fiber-optic system. This imposed a practical limitation on the highest frequency tests that could be conducted to around 60 kHz. Likewise, since the fiber-optic sensor has a sharp roll-off above 20 kHz, higher frequency testing would have been impractical.

The site where the tests were conducted was determined by three primary requirements: the need for fiber access, the need for power, and the size of the available acoustic free-field. A suitable site was located off the end of a shore-side tethered barge. The free-field at this

location was approximately 20 ft, enough to ensure that no reflections would influence the direct path of the waveform for the 2.5 kHz tests.

The fiber-optic hydrophone, the RESON reference hydrophone, and the ITC-1007 sound source were all deployed off the end of the barge to an approximate depth of 20 ft. The reference and fiber-optic hydrophones were located at roughly an equal distance from the source. However, exact measurements were not made since this was not intended to be a calibrated test. Likewise, all three units were freely suspended from the barge. No attempt was made to fix their positions since it was not a requirement of the test.

The location of the test elements was approximately 200 ft from shore, in the middle of a busy bay. As a result, several different sources of noise were present during the testing. High levels of transformer hum at 60 Hz and harmonics were present throughout all of the tests. Likewise, low levels of background boat traffic was consistently present. Higher levels of transient boat noise was also experienced, as was transient wave slap off of the nearby shore and barges. The noise was viewed as beneficial to the tests since this is the type of environment that the dynamic range extension approach must be able to work in. However, as would be expected, the noise reduced the overall peak levels of the input waveform that could be demodulated when compared to the simulated results.

Polarization fading mitigation was not implemented in the fiber-optic test sensor. As a result, the CNR experienced variations during testing and could not be accurately controlled. Therefore, the CNR values specified for each test is only an approximation. Some degree of CNR control was possible by adjusting the output power of an EDFA within the interrogation system. This, however, would not guarantee the CNR during the duration of the actual test window. This was particularly true for the 100 pulse reliability tests.

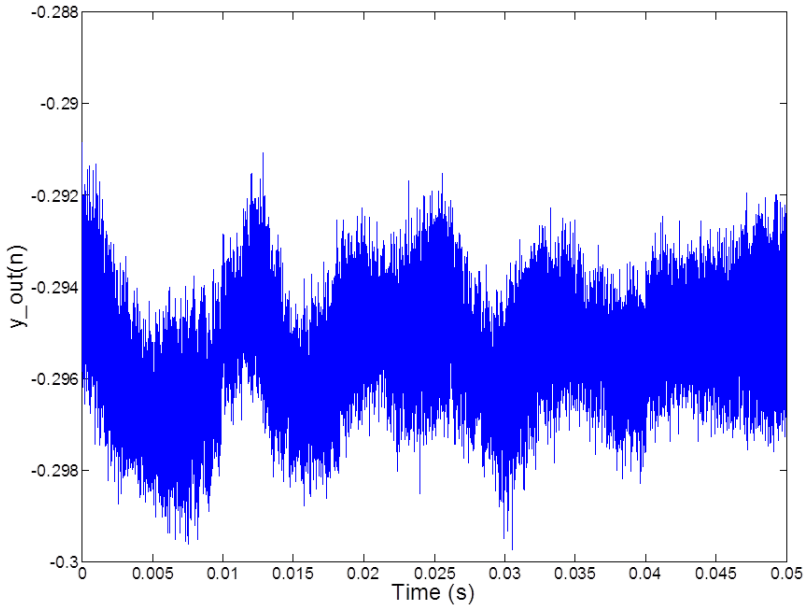

Figure 7.1: DIFM noise analysis, CNR ≈ 40 dB

7.2 Dynamic Range Extension Via DIFM Tests

7.2.1 Noise Floor Test

The first DIFM experimental test conducted was to evaluate the nominal output value and degree of noise of y_{out}. This test was conducted with an approximate CNR of 40 dB. The background noise addressed previously was present, but there were no high level transients during the acquisition. Figure 7.1 shows the results. The y_{out} output shows a nominal value of .295 with a variation of $\pm$.003. This is essentially identical to the simulated values determined in the previous chapter.

7.2.2 2.5 kHz Waveform Test

The next three tests were designed to experimentally validate the approach at the three frequencies used in the previous simulations. However, as was discussed earlier, generating a

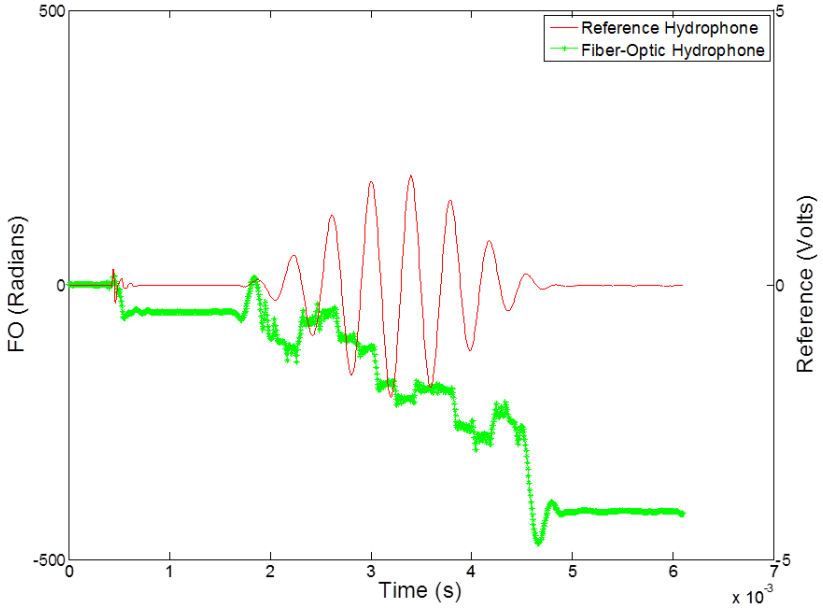

Figure 7.2: Experimental test with DRE disabled - $A_s = 1300$ radians, $f_s = 2.5$ kHz, and CNR ≈ 40 dB

high enough fringe rate signal at 1 kHz turned out to be impossible with the available equipment. Therefore, it was determined that the lowest frequency that could generate a high enough signal was at 2.5 kHz. This is actually a more stringent test since it is known that a frequency dependent limitation exists.

The first waveform test conducted was at 2.5 kHz. A peak drive level of 1300 radians was used. An attempt was made to collect the data when the CNR was approximately 40 dB. First, Figure 7.2 shows the demodulated output with the dynamic range extension correction factors disabled. The large DC offset in the fiber-optic output clearly shows that the demodulator has been been driven well into excession. The first DC shift in the demodulated output, occurring before the pulse, is the result of an excession caused by a gate enable transient of the L40 amplifier. Figure 7.3 now shows the same waveform with the dynamic range extension correction factors added in. The demodulated output and the reference waveform are in exact agreement. The figure also shows that the y_{out} output values are as expected. This provides an initial confirmation of the dynamic range extension approach via DIFM.

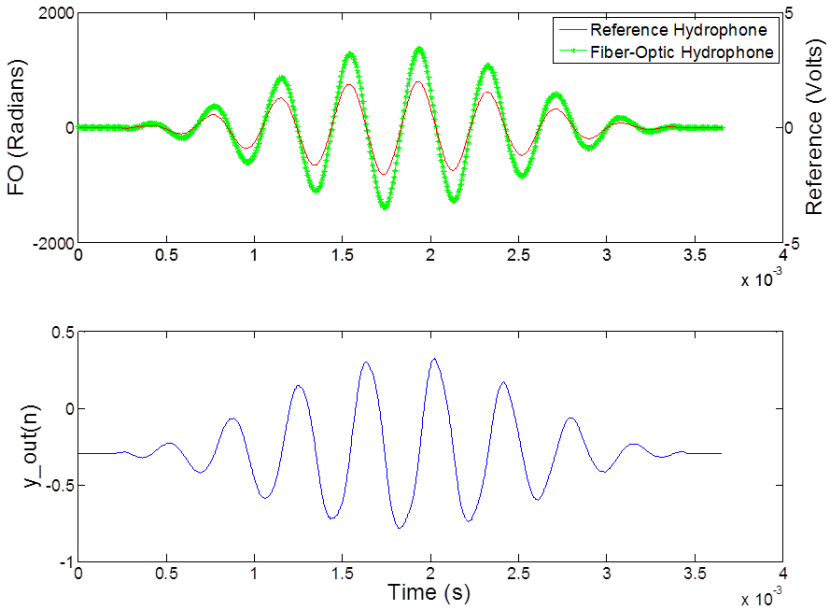

Figure 7.3: Experimental test with DRE enabled - $A_s = 1300$ radians, $f_s = 2.5$ kHz, and CNR ≈ 40 dB

7.2.3 10 kHz Waveform Test

The second waveform test was conducted at 320 radians, 10 kHz. Figures 7.4 and 7.5 show the results with and without the dynamic range extension enabled. As expected, with it disabled, the demodulator quickly loses track of the waveform. With it enabled, the correct waveform is recovered.

7.2.4 60 kHz Waveform Test

As described earlier, the 100 kHz waveform simulation tests could not be experimentally validated as the result of limitations of the available hardware. Rather, it was determined that 60 kHz was the highest frequency that could accurately be tested. Figures 7.6 and 7.7, again, show the results of the waveform tests at this frequency, both with the extension approach enabled and disabled. As can be seen in Figure 7.7, the demodulator is able to correctly recover the signal at 60 kHz. All three of the previous waveform tests have, therefore, been

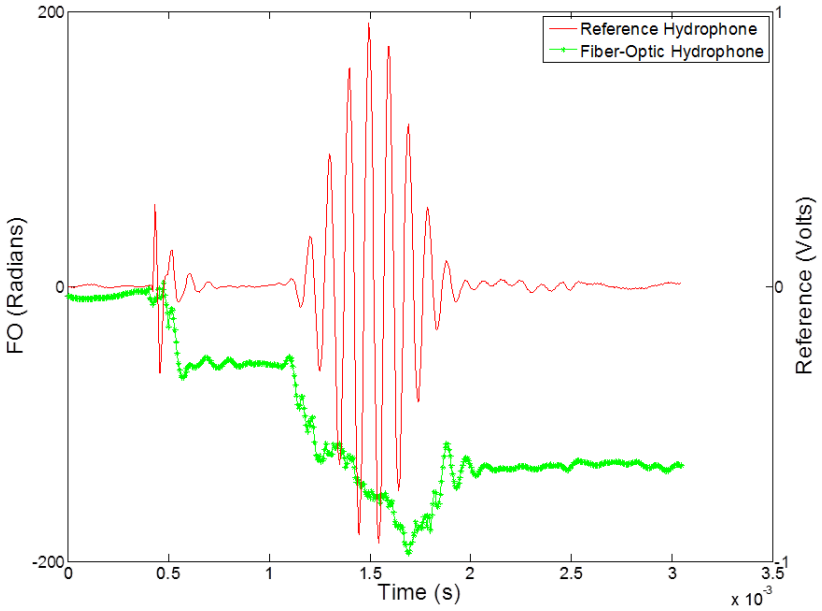

Figure 7.4: Experimental test with DRE disabled - $A_s = 320$ radians, $f_s = 10$ kHz, and CNR ≈ 40 dB

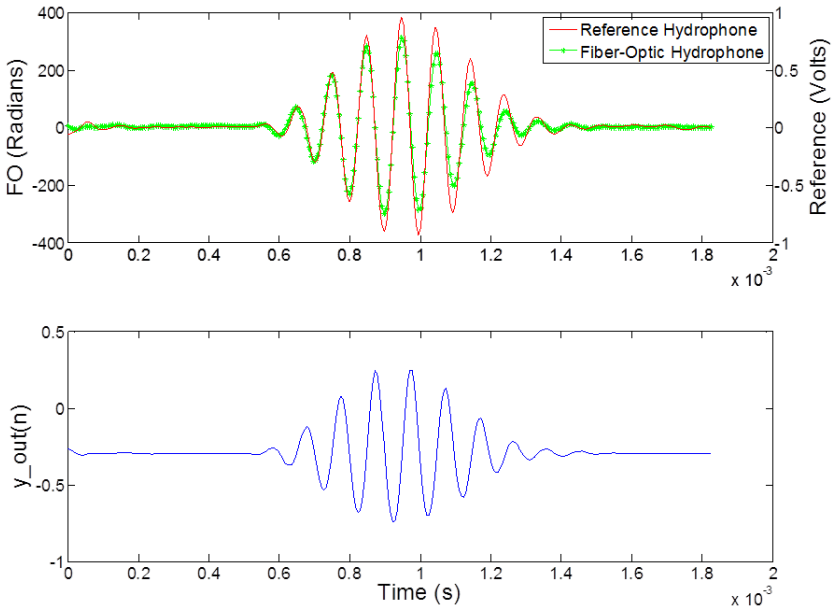

Figure 7.5: Experimental test with DRE enabled - $A_s = 320$ radians, $f_s = 10$ kHz, and CNR ≈ 40 dB

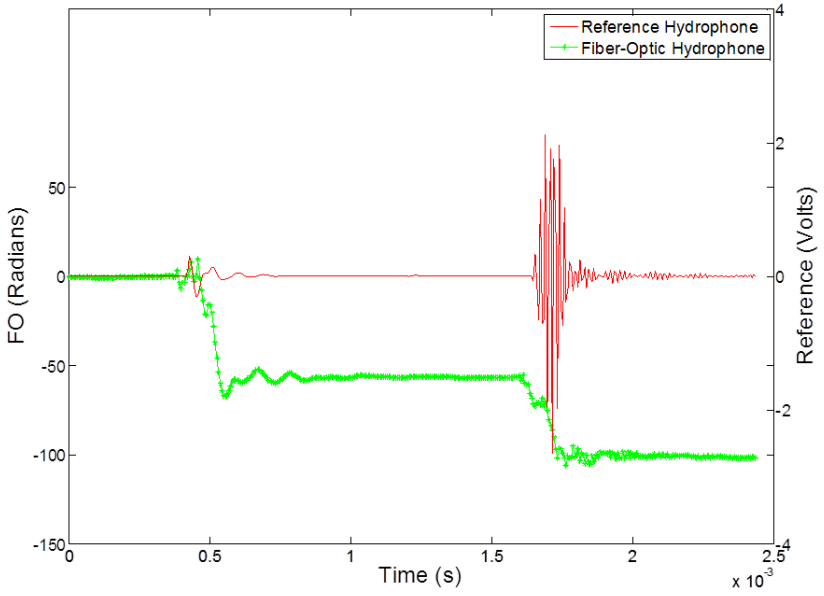

Figure 7.6: Experimental test with DRE disabled - $A_s = 50$ radians, $f_s = 60$ kHz, and CNR $\approx$ 40 dB

shown to achieve the stated dynamic range increase, validating the simulation results.

7.2.5 Frequency Dependency Tests

Simulation results from the previous chapter showed that dynamic range extension via DIFM required a minimum of 12-13 samples of the waveform for full extension. For the system at hand, the simulations showed that 60 kHz was the highest frequency that could achieve the full 20 dB extension. As the experimental tests just confirmed, 20 dB extension at 60 kHz is possible. However, limitations of the test system prevented higher frequency testing. As such, the frequency dependent roll-off of the dynamic range extension approach could not be experimentally validated.

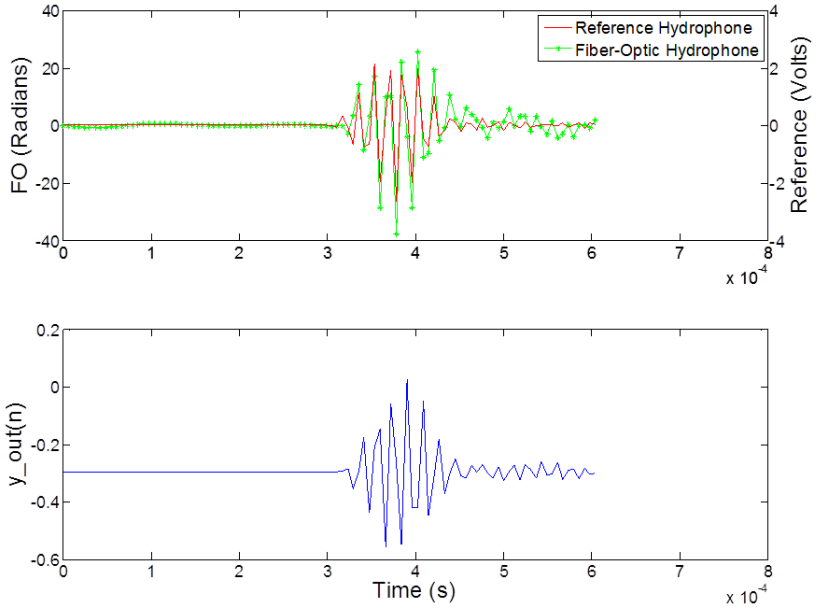

Figure 7.7: Experimental test with DRE enabled - $A_s = 50$ radians, $f_s = 60$ kHz, and CNR $\approx$ 40 dB

7.2.6 Reliability Tests

The previous experimental waveform tests confirmed the ability of the dynamic range extension approach to achieve the maximum designed increase. However, these tests were conducted under low ambient noise conditions, with a moderately high CNR level. Such conditions are ideal and not typical. To better determine the reliability of the approach, an additional round of testing was conducted.

A series of 100 pulses at each of the three test frequencies was used to test the reliability of the approach. These pulses were transmitted over several hours. During this time, the ambient and transient noise conditions varied widely. Likewise, the polarization visibility drifted over this period, varying the overall CNR.

Initial testing showed that ambient and transient acoustic noise conditions consumed as much as 2 dB of the available demodulator bandwidth. As a result, tests conducted with the maximum peak sinusoidal amplitude were likely to fail. This is as expected. Therefore, it was

determined that a more realistic test would be to reduce the peak sinusoidal drive levels by 3 dB and allow for high level transients.

The first round of reliability tests were conducted with a nominal CNR of 40 dB. During the test period, the CNR was observed varying by only ± 3 dB. The background ambient was significantly high but was considered desirable to more rigorously test the overall reliability. Of the three different waveforms transmitted, it was expected that the reliability of correctly demodulating the input would have some dependence on the waveform frequency. However, this was not observed. All 300 pulses transmitted were correctly recovered without any detected excessions.

A second round of reliability tests was conducted with a reduced CNR of 20 dB. The same polarization induced CNR variations of approximately ±3 dB were observed during the test. It was anticipated that some failures would be observed with the reduced level. However, all 300 pulses were again demodulated correctly.

The CNR level had to be reduced to nearly 12 dB before significant errors were introduced by the dynamic range extension approach. As stated previously, such low CNR levels are uncommon in most interferometric systems . The overall conclusion from this testing is that the reliability of the approach is very high.

7.2.7 DIFM Analysis

The DIFM experimental tests largely confirmed the simulated work of the previous chapter. All three sinusoidal waveforms could be demodulated with a 20 dB extension over the standard output process. Extended reliability tests, conducted over various CNR levels, confirmed the approach to be viable in applications subjected to high levels of ambient and transient noise. One aspect of the approach that could not be tested was the frequency dependency. The experimental tests were, however, able to demodulate the highest frequency signals that could be generated. The excellent results provided by the approach, combined with the minimal hardware resources required for implementation, makes DIFM ideal for dynamic range extension.

7.3 Dynamic Range Extension Via DFT Tests

The same set of experimental tests used to validate the DIFM method were conducted for DFT. However, correct interpretation of the DFT coefficients is more challenging than the y_{out} value of DIFM. Complicating matters is the fact that the FPGA only had enough internal memory to acquire four of the 22 coefficients. Therefore, the figures in the following experimental tests only display the four coefficients closest to the nominal carrier frequency.

7.3.1 Noise Floor Test

The first DFT experimental test was to determine the nominal output and noise levels of the DFT coefficients. Figure 7.8 shows the results for a typical low acoustic noise measurement and nominal CNR of 40 dB. The results are largely as expected. The high levels of noise are consistent with the simulated results. However, what was not as apparent from the simulations was how the nominal values varied with the magnitude of the received carrier signal. As a modulating signal was applied to the sensor, the CNR would vary based on the polarization states, and as a result, the nominal DFT coefficients would also track the waveform. While this issue was initially a concern, subsequent testing has shown it to have little to no impact on the ability of the approach to correctly demodulate waveforms.

7.3.2 2.5 kHz Waveform Test

The second test conducted was the 1300 radian, 2.5 kHz waveform pulse. The results without the correction factors added in were presented earlier in the chapter and will not be repeated in this section. Figure 7.9 shows that with the dynamic range extension correction factors added in the waveform is correctly recovered. Closer analysis confirmed that no DC offsets were present over the duration of the waveform. This, again, provides an initial confirmation that dynamic range extension via DFT carrier measurement is feasible.

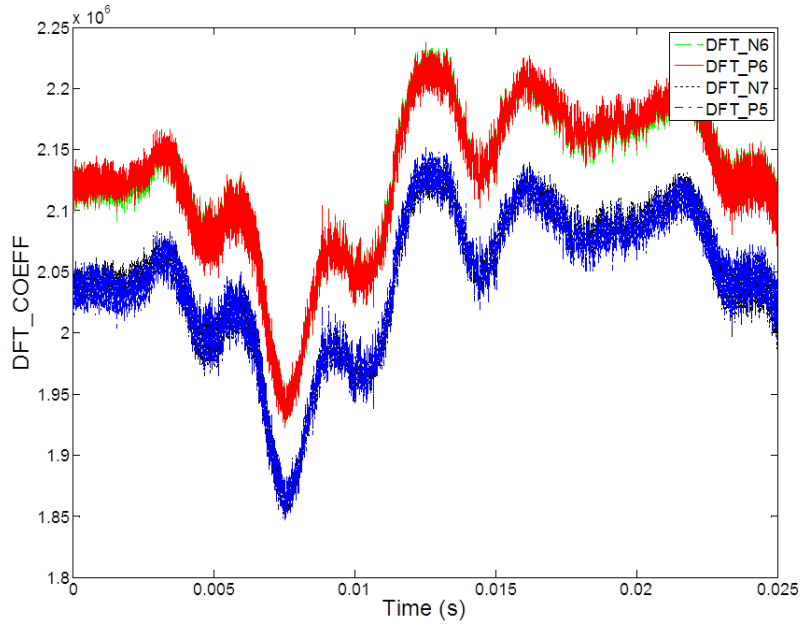

Figure 7.8: DFT noise analysis, CNR ≈ 40 dB

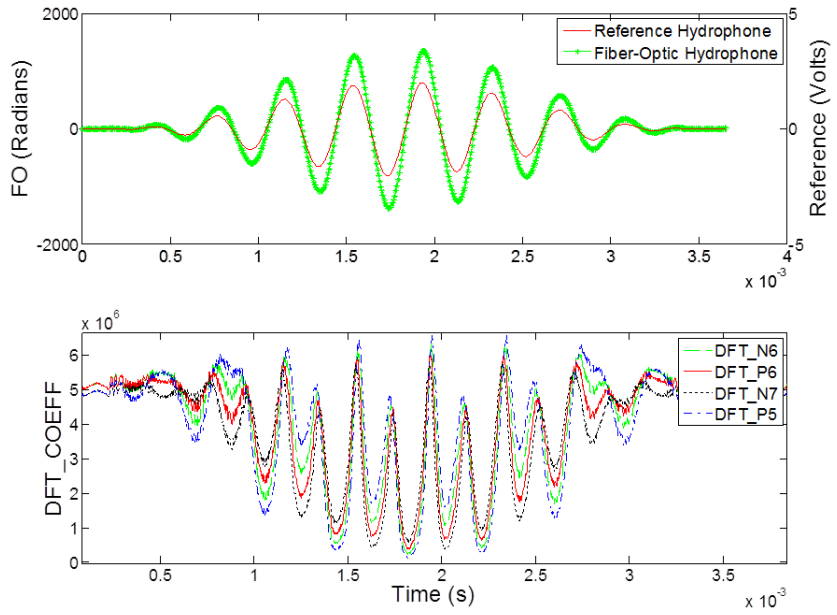

Figure 7.9: Experimental test with DFT DRE enabled - $A_s = 1300$ radians, $f_s = 2.5$ kHz, and CNR ≈ 40 dB

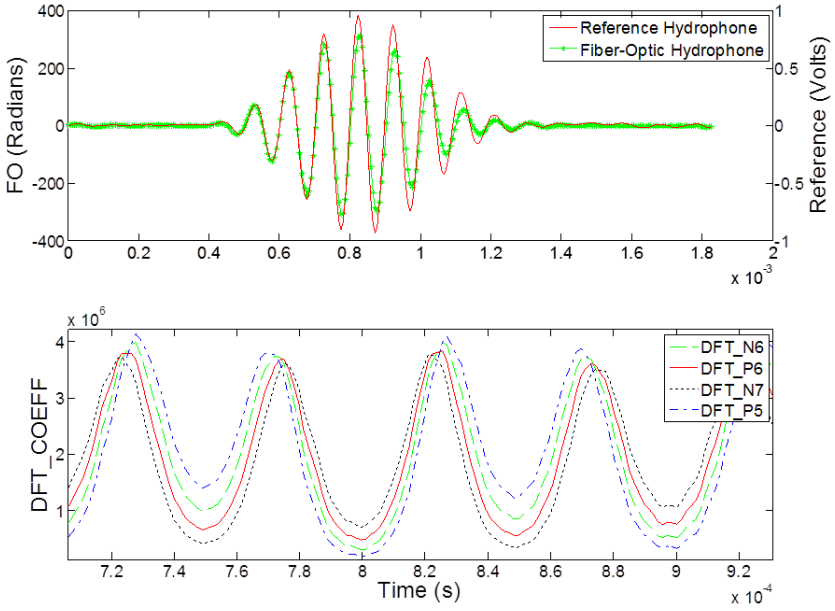

Figure 7.10: Experimental test with DFT DRE enabled - $A_s = 320$ radians, $f_s = 10$ kHz, and CNR ≈ 40 dB (Zoom)

7.3.3 10 kHz Waveform Test

Figure 7.10 shows the results of the 10 kHz waveform test. The figure confirms that the approach is able to accurately track the incoming wave. Likewise, the DFT coefficient plot of the figure has been zoomed in over a small section of the waveform to more clearly show the transitions. These transitions match the expected results as obtained previously from the simulations.

7.3.4 60 kHz Waveform Test

The last waveform test that was conducted was, again, at 60 kHz. Figure 7.11 shows that the DFT method is able to correctly demodulate the high frequency signal. Therefore, the DFT approach has been shown to successfully demodulate all three of the waveforms, and as such, the simulated results of the previous chapter have been validated.

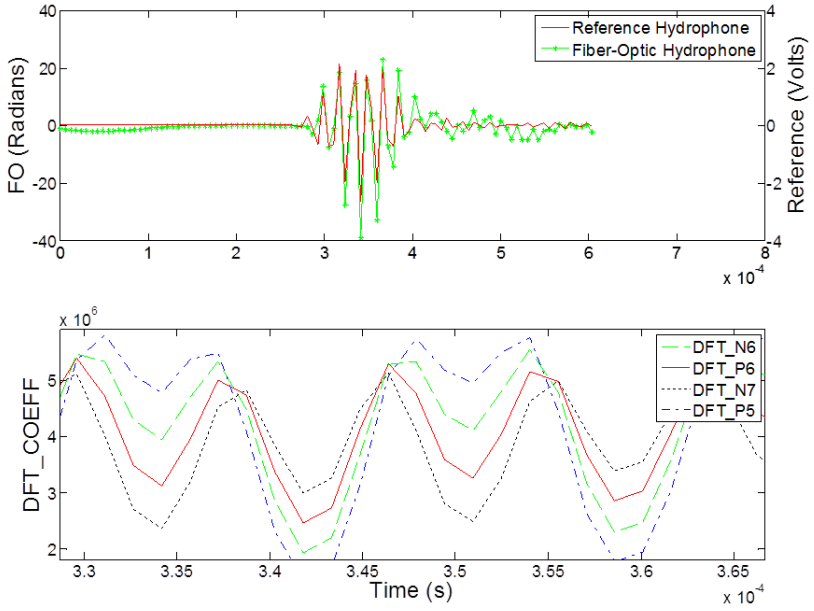

Figure 7.11: Experimental test with DFT DRE enabled - $A_s = 50$ radians, $f_s = 60$ kHz, and CNR ≈ 40 dB (Zoom)

7.3.5 Frequency Dependency Tests

Simulation results from the previous chapter showed that dynamic range extension via DFT required a minimum of 8-9 samples of the waveform for full extension. The simulations showed that 80 kHz was the highest frequency that could achieve the full 20 dB extension for the given system. However, hardware limitations prevented experimental testing beyond 60 kHz. While the DFT approach was able to successfully demodulate the 60 kHz waveform, the highest frequency that could actually be handled could not be determined. Likewise, determining the degree of frequency dependent roll-off was not possible. Therefore, it was not possible to validate the apparent high-frequency advantage that DFT has over DIFM; as determined through simulations in the previous chapter.

7.3.6 Reliability Tests

The same set of reliability tests conducted for the DIFM method were repeated for DFT. This included transmitting and demodulating a series of 100 pulses of each of the three test waveforms. However, as discussed previously, the peak sinusoidal drive levels were reduced by 3 dB to account for the bandwidth consumed by the ambient and transient acoustic noise present during the tests. The test was conducted at two nominal CNR levels.

The experimental reliability test results were the same as determined previously for the DIFM method. The 300 pulse tests were conducted at both 40 dB and 20 dB CNR nominal levels. All pulses were successfully demodulated. Therefore, the dynamic range extension via DFT method has also been shown to provide a very high level of reliability. Experimental testing was not able to determine any reliability differences between the two methods, as was detected by the simulated results.

7.3.7 DFT Analysis

The DFT experimental tests confirmed the simulated work of the previous chapter. All three sinusoidal waveforms could be demodulated with a 20 dB extension over the standard output process. Extended reliability tests conducted over various CNR levels confirmed the approach to be viable in applications subjected to high levels of ambient and transient noise. However, as with the DIFM testing, the frequency dependent roll-off could not be verified as a result of hardware limitations. While experimental tests were able to demodulate the highest frequency signals that could be generated at 60 kHz, the maximum simulated frequency of 80 kHz could not be confirmed. However, the experimental testing did validate the dynamic range extension approach via DFT as being highly reliable within the primary measurement band.

7.4 Summary

Both the DIFM and the DFT variants of the dynamic range extension approach were experimentally validated. Waveform tests conducted at low, mid, and high frequencies all confirmed the ability of both variants to successfully extended the dynamic range by more than 20 dB. Few differences were detected between the two approaches. Both achieved 100% success during the extended reliability testing. However, the previous simulations showed that the DFT method had a slight frequency dependent improvement above 60 kHz. While sensor and system limitations prevented higher frequency testing, both methods are deemed as viable candidates for systems which require dynamic range extension.

Chapter 8 Conclusion

8.1 Contributions

This dissertation has made several contributions to the field of fiber-optic sensing, the primary of which is the successful development and demonstration of a technique for extending the dynamic range of heterodyne fiber-optic sensors by more than 20 dB. In the process of completing such work, multiple tasks have been accomplished.

First, the development of a heterodyne fiber-optic demodulation MATLAB simulation script was completed. Using this simulator, three methods of instantaneous carrier measurement and two methods of dynamic range extension were successfully tested and evaluated. The results of the simulator matched closely with the experimental results. This simulator can, therefore, be used in the design and testing of future demodulation hardware.

Three unique methods of instantaneous carrier measurement were presented and tested as part of this dissertation. The DIFM approach was shown to require minimal hardware, yet, provide low-noise wide-bandwidth frequency tracking capabilities. The DFT method provided the widest bandwidth tracking but was limited by the amount of required hardware resources. The last method presented, PECM, required the fewest hardware resources but was found to have significant performance limitations when compared to the other two methods.

Both the DIFM and the DFT methods of instantaneous carrier measurement were experimentally tested for use in the dynamic range extension approach. They were found to provide comparable results. Both were able to achieve bandwidth limited dynamic range increases in excess of 20 dB. The DIFM approach required substantially less hardware resources and was determined to be the optimal solution for dynamic range extension applications. DFT did have a small frequency dependent performance advantage in the simulated results. However, hardware limitations prevented the experimental validation of this advantage. The experimental dynamic range testing, therefore, largely confirmed the analysis and theory of this dissertation.

8.2 Future Work

The work completed as part of this dissertation has not addressed all issues related to the topic. Several potential areas of future research need to be addressed.

The simulated results showed a frequency dependent roll-off of the available dynamic range extension. This is as expected given the carrier averaging requirement of the extension approach. The simulations showed that the DIFM approach could provide full dynamic range extension to 60 kHz, while DFT was out to 80 kHz. A lesser degree of extension was possible at higher frequencies. However, limitations of both the fiber-optic sensor and the hardware used to generate the acoustic pulses prevented testing beyond 60 kHz. Therefore, work remains to experimentally test the high-frequency roll-off.

For large dynamic range extensions, the bandwidth required by the demodulator can be substantial. It is also well known that for wideband modulated systems, distortion can be introduced from the phase response of the communication channel and/or system components. With an all-digital heterodyne demodulator, the front-end still requires several analog stages that can present differing phase delays over a wide bandwidth. Digital filtering stages of the demodulator can also introduce wideband modulation phase errors. These were not addressed as part of this work; however, the carrier frequency tracking methods presented could be used to help equalize such errors.

In a heterodyne modulated system where TDM is not utilized, two types of pulses are received at the demodulator. The first occurs when the two overlapping optical pulses have traveled an equal distance from the pulse generator to the receiver. In the second type, one of the two overlapping optical pulses has traveled twice the length of the sensor more than the other pulse. This large differential in path lengths generates high levels of phase noise as a result of laser frequency noise within these pulses. As a result, these pulses are discarded. However, although the phase noise of these pulses may be too high for the standard demodulation process, they may be suitable for obtaining carrier frequency information and further dynamic range increases.

It was mentioned previously that the dynamic range extension approach presented in this dissertation utilized a two-point, equally-weighted average of the current and the previous instantaneous carrier measurements. Although this was shown to reliably provide more than a 20 dB dynamic range increase, a more advanced averaging approach may provide additional improvements. One potential method mentioned previously is the use of the current, the previous, and the following instantaneous carrier measurements. This approach could be coupled with utilizing the discarded heterodyne pulses, as just discussed. This combination could potentially provide dynamic range increases well in excess of 20 dB.

8.3 Conclusion

This dissertation documented a method of extending the dynamic range of a heterodyne fiber-optic interferometer by tracking the instantaneous carrier frequency. The demonstrated dynamic range increase was in excess of 20 dB. In addition, the results of the simulated and experimental tests matched with a high level of agreement, further validating the technique. Because of the success of this research, the DIFM dynamic range extension approach has already been implemented in a new large-scale heterodyne fiber-optic sensor array.

Bibliography

[1] A. Udd, *Fiber Optic Sensors: An Introduction for Engineers and Scientists*, 1st ed. John Wiley & Sons, Inc., 1991, pp. 271–320.

[2] R. Kashyap, *Fiber Bragg Gratings*, 1st ed. Elsevier, Inc., 2010, pp. 441–496.

[3] C. E. Webb, J. C. Jones, G. A. Cranch, and P. J. Nash, *Handbook of Laser Technology: Optical Fibre Hydrophones*, 1st ed. UK: Inst. Physics Publishing, 2004, pp. 1839–1880, sec. D2.5.

[4] C. K. Kirkendall and A. Dandridge, "Overview of high performance fibre-optic sensing," *Journal of Physics D: Applied Physics*, vol. 37, no. 18, p. R197, 2004. [Online]. Available: http://stacks.iop.org/0022-3727/37/i=18/a=R01

[5] N. Zhang, Z. Meng, S. Xiong, and Q. Yao, "Heterodyne demodulation scheme for fiber-optic hydrophone arrays," pp. 78 530R–78 530R–8, 2010. [Online]. Available: + http://dx.doi.org/10.1117/12.870444

[6] G. A. Cranch and P. J. Nash, "Large-scale multiplexing of interferometric fiber-optic sensors using TDM and DWDM," *Lightwave Technology, Journal of*, vol. 19, no. 5, pp. 687–699, 2001.

[7] Y. Liao, E. Austin, P. J. Nash, S. A. Kingsley, and D. J. Richardson, "Highly scalable amplified hybrid TDM/DWDM array architecture for interferometric fiber-optic sensor systems," *Lightwave Technology, Journal of*, vol. 31, no. 6, pp. 882–888, 2013.

[8] Y. Liao, E. Austin, P. Nash, S. Kingsley, and D. Richardson, "Phase sensitivity characterization in fiber-optic sensor systems using amplifiers and tdm," *Lightwave Technology, Journal of*, vol. 31, no. 10, pp. 1645–1653, 2013.

[9] "RIO ORION data sheet," Redfern Integrated Optics Inc., Santa Clara, California.

[10] K. Wanser, "Fundamental phase noise limit in optical fibres due to temperature fluctuations," *Electronics Letters*, vol. 28, no. 1, pp. 53–54, 1992.

[11] M. J. Marrone, A. D. Kersey, and A. D. Dandridge, "Polarization-independent array configurations based on michelson interferometer networks," pp. 196–200, 1993. [Online]. Available: + http://dx.doi.org/10.1117/12.141288

[12] N. Zhang, Z. Meng, W. Rao, and S. Xiong, "Investigation on upper limit of dynamic range of fiber optic interferometric sensors base on the digital heterodyne demodulation scheme," pp. 8421BE–8421BE–4, 2012. [Online]. Available: + http://dx.doi.org/10.1117/12.975121

[13] T. Berkoff and A. Kersey, "Signal processing techniques for absolute displacement/strain sensing using a fiber interferometer," *Optics and Lasers in Engineering*, vol. 16, no. 23, pp. 153 – 161, 1992, ¡ce:title¿Special Issue on Optical Sensors for Aerospace Applications¡/ce:title¿. [Online]. Available: http://www.sciencedirect.com/science/article/pii/014381669290006S

[14] A. D. Kersey and A. Dandridge, "Dual-wavelength approach to interferometric sensing," pp. 176–181, 1987. [Online]. Available: + http://dx.doi.org/10.1117/12.941102

[15] C. E. Towers, D. P. Towers, D. T. Reid, W. N. MacPherson, R. R. J. Maier, and J. D. C. Jones, "Fiber interferometer for simultaneous multiwavelength phase measurementwith a broadband femtosecond laser," *Opt. Lett.*, vol. 29, no. 23, pp. 2722–2724, Dec 2004. [Online]. Available: http://ol.osa.org/abstract.cfm?URI=ol-29-23-2722

[16] C. E. Towers, D. P. Towers, and J. D. C. Jones, "Optimum frequency selection in multifrequency interferometry," *Opt. Lett.*, vol. 28, no. 11, pp. 887–889, Jun 2003. [Online]. Available: http://ol.osa.org/abstract.cfm?URI=ol-28-11-887

[17] K. Falaggis, D. P. Towers, and C. E. Towers, "A hybrid technique for ultra-high dynamic range interferometry," pp. 70 630X–70 630X–8, 2008. [Online]. Available: + http://dx.doi.org/10.1117/12.795293

[18] M. Corke, J. Jones, A. Kersey, and D. Jackson, "Combined michelson and polarimetric fibre-optic interferometric sensor," *Electronics Letters*, vol. 21, no. 4, pp. 148–149, 1985.

[19] P. W. East, "Fifty years of instantaneous frequency measurement," *Radar, Sonar Navigation, IET*, vol. 6, no. 2, pp. 112–122, 2012.

[20] P. L. Herselman and J. E. Cilliers, "A digital instantaneous frequency measurement technique using high-speed analogue-to-digital converters and field programmable gate arrays," *South African Journal of Science*, vol. 102, Aug 2006.

[21] D. M. Lin, L. L. Liou, S. Benson, and H. Chen, "Mono-bit digital chirp receiver using mono-bit IFM (instantaneous frequency measurement) receiver as a core," in *Aerospace and Electronics Conference (NAECON), Proceedings of the 2011 IEEE National*, 2011, pp. 348–351.

[22] I. Hatai and I. Chakrabarti, "FPGA implementation of a digital FM modem for SDR architecture," in *Computers and Devices for Communication, 2009. CODEC 2009. 4th International Conference on*, 2009, pp. 1–4.

[23] M. Rice, M. Padilla, and B. Nelson, "On FM demodulators in software defined radios using FPGAs," in *Military Communications Conference, 2009. MILCOM 2009. IEEE*, 2009, pp. 1–7.

[24] L. W. Couch, *Analog and Digital Communication Systems*, 8th ed. Pearson Education Inc., 2013, pp. 331–348.

Appendix A Derivation of Heterodyne Current Equation

This appendix provides a derivation of the heterodyne photodetector current. The following has been derived largely from the Mach-Zehnder current derivation presented in [3].

The heterodyne current i_{pd} is generated from two optical pulses overlapping and mixing on the demodulator's photodetector. One of the pulses is considered the signal and is modulated at f_1, using an AOM, to a frequency of $f_T + f_1$. The value f_T is the natural oscillation frequency of the light and is in on the order of several hundred Terahertz. The second pulse is the reference pulse, and is modulated to a frequency of $f_T + f_2$. Assuming the power levels in the both the reference and the signal pulses are equal to P, the optical fields can be determined from the following equations.

$$E_s(t) = \sqrt{P}\cos(2\pi(f_T + f_1)t + \phi_s(t)) \tag{A.1}$$

$$E_r(t) = \sqrt{P}\cos(2\pi(f_T + f_2)t + \phi_r(t)) \tag{A.2}$$

The two pulses travel difference paths within the interferometer but arrive simultaneously at the demodulator's photodetector. The photodetector, being a square-law device, will produce an output which is the square of the total input, provided the optical polarization states are not orthogonal. Therefore, the amount of current produced by the photodetector will be equal to the square of the total input optical field, times the responsivity r of the photodetector itself.

$$i_{pd}(t) = r * (E_s(t) + E_r(t))^2 \tag{A.3}$$

$$i_{pd}(t) = r * (\sqrt{P}\cos(2\pi(f_T + f_1)t + \phi_s(t)) + \sqrt{P}\cos(2\pi(f_T + f_2)t + \phi_r(t)))^2 \tag{A.4}$$

$$i_{pd}(t) = rP\cos^2(2\pi(f_T + f_1)t + \phi_s(t)) + rP\cos^2(2\pi(f_T + f_2)t + \phi_r(t)) + 2rP\cos(2\pi(f_T + f_1)t + \phi_s(t)) * \cos(2\pi(f_T + f_2)t + \phi_r(t)) \quad \text{(A.5)}$$

Using the cosine power reduction and the product-to-sum identifies, the above equation can be reduced to

$$\begin{aligned} i_{pd}(t) = {} & \frac{rP}{2} + \frac{rP}{2}\cos(4\pi(f_T + f_1)t + 2\phi_s(t)) + \\ & \frac{rP}{2} + \frac{rP}{2}\cos(4\pi(f_T + f_2)t + 2\phi_r(t)) + \\ & rP\cos(2\pi(f_1 - f_2)t + \phi_s(t) - \phi_r(t)) + \\ & rP\cos(2\pi(2f_T + f_1 + f_2)t + \phi_s(t) + \phi_r(t)) \end{aligned} \quad \text{(A.6)}$$

All of the terms in equation A.6 containing f_T can be omitted by taking the time average of the output over the photodetector's time constant. This effectively removes the high frequency components which cannot be observed. The equation therefore reduces to

$$i_{pd}(t) = rP + rP\cos(2\pi(f_1 - f_2)t + \phi_s(t) - \phi_r(t)) \quad \text{(A.7)}$$

The difference between f_1 and f_2 is designed to be the heterodyne interferometer carrier frequency, thus $f_1 - f_2$ can be replaced with f_c. It was also mentioned previously that proper mixing of the optical fields on the photodetector will only take place if the polarization states between the signal and the reference pulses are not orthogonal. When they are, the time varying component will fade. As a result, a polarization visibility factor V is added to the equation. This factor can range from $0 \leq V \leq 1$, depending on the degree of orthogonality. Making these replacements, the final heterodyne current equation is obtained.

$$i_{pd}(t) = rP + rPV\cos(2\pi f_c t + (\phi_s(t) - \phi_r(t))) \quad \text{(A.8)}$$

Appendix B DIFM MATLAB Simulation Code

Listing B.1: DIFM MATLAB simulation code

```
%Use FIR (odd) filter or (even) simple BOX FIR filter
filt_en = 0;

%Set time series and sample rate parameters
N = 8;
M = 1;
cycles = 64*N; %fsamp samples
fc = 10e6*M; %10nsec
pw = 76*M; %10nsec
delay = 10*M; %10nsec
samples = 50*M+1;

%Set digiziter parameters
dig_bits = 16;
peak_dig = 2^(dig_bits-1);
iq_bits = 16;
peak_iq = 2^(iq_bits-1);
fir_bits = 16;
peak_fir = 2^(fir_bits-1);

%Set the digitization sample rate
fs = 100e6*M;
ts = (0:(1/fs):(1/fs)*pw*(cycles)*2);
ts = ts(1:end-1);

%Time series of individual acquired pulses
t_ext = (0:(1/fs):(1/fs)*(samples-1));

%Time series of demodulated pulses
fsamp = 1/(pw*2*(1/fs));
tsamp = (0:(1/fsamp):(1/fsamp)*(cycles));
tsamp = tsamp(1:end-1);
fr_demod = fsamp*pi

%Window the input signal being demodulated
%to avoid initial transients
data_win = tukeywin(size(ts,2),1)';
data_win_sampled = tukeywin(size(tsamp,2),1)';
```

```
%Window the individual pulses to simulate
%the ramp and fall times of the carrier
win = tukeywin(pw,.1)';

%Create the time series windows to sample the
%incoming signal
window = [];
for i = 0:cycles-1
  window = [ window, win ];
  window = [ window, zeros(pw,1)' ];
end;

%Window the acquired samples of the pulses
%to reduce error
%iq_win = ones(samples,1)';
%iq_win = tukeywin(samples,1)';
%iq_win = blackman(samples)';
%iq_win = flattopwin(samples)';
%iq_win = hanning(samples)';
iq_win = nuttallwin(samples)';
iq_win = floor(iq_win.*peak_fir);
box_win = nuttallwin(samples-1)';
box_win = floor(box_win.*peak_fir);

%Create the low-pass filters if simple BOX averaging
%filter is not used
if filt_en == 1
%    n_filt = samples-1;
%    fnyq = fs/2;
%    fch = 18e6; %20MHz null
%    fcl = 2e6; %3MHz bandwidth max
%    f = [0 (fcl/fnyq) (fch/fnyq) 1];
%    w = [1 1 0 0];
%    b = remez(n_filt, f, w);
%    b = floor(b*peak_fir);
     a = 1;
     fir = load('fir_51pt.mat','b');
     b = fir.b;
```

```
%   figure;
%   freqz(b);
end;
fir = load('fir_51pt.mat','b');

%Create the ambient noise shaping low-pass filters
n_filt = 1000;
fnyq = fs/2;
fch = 200e3; %20MHz null
fcl = 1e3; %3MHz bandwidth max
f = [0 (fcl/fnyq) (fch/fnyq) 1];
w = [1 1 0 0];
%bn = remez(n_filt, f, w);
h = load('filt_coeff_1k_50k_8001.mat','h');
bn = h.h;
an = 1;
%figure;
%freqz(bn);


%Carrier amplitude for CNR testing and
%autocorrelation correction
Ac = .5;

%Create signal and noise waveforms
Asig = 160; %
fsig = 10000; %81920 or 10e3
phi = 0;
fr_sig = 2*pi*Asig*fsig
bw = Asig*fsig

%Signal noise
An_sig = 26000;
sig_noise = filter(bn, an, An_sig*(rand(size(ts))-.5));
sig_noise = filter(bn, an, sig_noise);
sig_noise = filter(bn, an, sig_noise);

%Carrier Noise
An = .01;
```

```
fn = 10e6+157e3;
phin = 0;
%noise = An*sin(2*pi*fn*ts + phin);
car_noise = An*(rand(size(ts))-.5);

%Create multitone noise components (if used)
An1 = 0.0001;
fn1 = 10e6+157e3;
An2 = 0.0001;
fn2 = 10e6-157e3;
An3 = 0.0001;
fn3 = 157e3;

%noise = An1*sin(2*pi*fn1*ts) + An2*sin(2*pi*fn2*ts) + An3*sin(2*pi*fn3*ts);

%Create the pulsed carrier waveform
%used for testing the carrier spectrum
pulsed_carrier = sin(2*pi*fc*ts).*window - .5;



%Create the "analog" signal and only keep
%data at the pulses
sig = (Asig*sin(2*pi*fsig*ts + phi) + sig_noise ).*data_win;
data = (Ac*sin(2*pi*fc*ts + sig )).*window + car_noise;

%Create a copy of the incoming signal at the
%actual demodulation rate for comparison testing
%of the output
%sig_sampled = Asig*sin(2*pi*fsig*tsamp).*data_win_sampled;
sig_sampled = [];
for i = 1:size(tsamp,2)
  sig_sampled = [sig_sampled sig(pw+(i-1)*pw*2)];
end

%Digitize the acquired pulses
data = floor(data*peak_dig);

%Create the digital I/Q components
I = floor(cos(2*pi*fc*ts)*peak_iq);
```

```
Q = floor(sin(2*pi*fc*ts)*peak_iq);
I_data = I.*data;
Q_data = Q.*data;

%Initialize loop parameters
acquire = 0;
delay_cnt = 0;
num_samples = 0;
phase_last = 0;
phase_cur = 0;
phase_diff = 0;
phase_accum = 0;
phase_accum_no_dre = 0;
phase_cf = 0;
demod = [];
demod_no_dre = [];
I_samp = [];
Q_samp = [];
D_samp = [];
diff_lst = [];

%Initial DR extension variables
%AVG must be 2 or more
navg = 2;
DIFM_last = -.295;
DIFM_cur = -.295;
DIFM_lst = [];
D_auto = [];

%Process over all digitized samples of
%the incoming carrier signal
for i = 1:pw*cycles*2

    %Only select samples for demodulation within
    %the specified window
    if ( delay_cnt >= delay )&&( delay_cnt <= delay+samples-1 )
      acquire = 1;
    else
      acquire = 0;
```

```
end;

%The sample window starts on the rising edge of
%received optical pulse
if ( window(i) > .5 )
  delay_cnt = delay_cnt + 1;
else
  delay_cnt = 0;
end;

%The number of specified digital samples has been
%received, begin demodulating the pulse
if ( num_samples == samples-1 ) && ( acquire == 1 )

  phase_last = phase_cur;

  %Obtain I/Q components and the carrier signal for DR ext
  I_samp = [I_samp, I_data(i)];
  Q_samp = [Q_samp, Q_data(i)];
  D_samp = [D_samp, data(i)];

  %If filter enable is enabled, used an N (odd) point
  %FIR filter to process the I/Q data, otherwise use
  %use and N (even) point BOX FIR filter
  if filt_en == 1
    i_filt = filter(b,a,I_samp);
    q_filt = filter(b,a,Q_samp);
    phase_cur = atan2(i_filt(end),q_filt(end));
  else
    i_sum = sum(I_samp(1:end-1).*box_win);
    q_sum = sum(Q_samp(1:end-1).*box_win);
    phase_cur = atan2(i_sum,q_sum);
  end;

  %Compute the phase change and unwrap the signal
  phase_diff = phase_cur - phase_last;
  if ( phase_diff > pi )
    phase_diff = phase_diff - 2*pi;
  elseif ( phase_diff < -pi )
```

```
  phase_diff = phase_diff + 2*pi;
end;

diff_lst = [diff_lst, phase_diff];


%Peform the DIFM DR approach
D_samp = D_samp;
D_samp = D_samp.*iq_win;
DIFM_auto = sum([D_samp,0,0,0].*[0,0,0,D_samp]);
DIFM_cf   = sum(D_samp.*D_samp);
DIFM_last = DIFM_cur;
DIFM_cur  = DIFM_auto/DIFM_cf;
DIFM_avg  = mean([DIFM_cur DIFM_last]);
DIFM_lst  = [DIFM_lst, DIFM_avg];

if (phase_diff < 0)

  if DIFM_avg < -.792
    phase_cf = 12*pi;
  elseif DIFM_avg < -.722
    phase_cf = 10*pi;
  elseif DIFM_avg < -.638
    phase_cf = 8*pi;
  elseif DIFM_avg < -.544
    phase_cf = 6*pi;
  elseif DIFM_avg < -.441
    phase_cf = 4*pi;
  elseif DIFM_avg < -.330
    phase_cf = 2*pi;
  elseif DIFM_avg < -.215
    phase_cf = 0*pi;
  elseif DIFM_avg < -.096
    phase_cf = -2*pi;
  elseif DIFM_avg < .023
    phase_cf = -4*pi;
  elseif DIFM_avg < .140
    phase_cf = -6*pi;
  elseif DIFM_avg < .253
```

```
    phase_cf = -8*pi;
  elseif DIFM_avg < .361
    phase_cf = -10*pi;
  else
    phase_cf = -12*pi;
  end;

else

  if DIFM_avg < -.825
    phase_cf = 12*pi;
  elseif DIFM_avg < -.759
    phase_cf = 10*pi;
  elseif DIFM_avg < -.682
    phase_cf = 8*pi;
  elseif DIFM_avg < -.593
    phase_cf = 6*pi;
  elseif DIFM_avg < -.494
    phase_cf = 4*pi;
  elseif DIFM_avg < -.386
    phase_cf = 2*pi;
  elseif DIFM_avg < -.273
    phase_cf = 0*pi;
  elseif DIFM_avg < -.156
    phase_cf = -2*pi;
  elseif DIFM_avg < -.036
    phase_cf = -4*pi;
  elseif DIFM_avg < .082
    phase_cf = -6*pi;
  elseif DIFM_avg < .197
    phase_cf = -8*pi;
  elseif DIFM_avg < .308
    phase_cf = -10*pi;
  else
    phase_cf = -12*pi;
  end;

end;
```

```
        %Accumulate the phase using the DR extension
        %correction factor
        phase_accum = phase_accum + phase_diff + phase_cf;
        demod = [demod , phase_accum];

        phase_accum_no_dre = phase_accum_no_dre + phase_diff;
        demod_no_dre = [demod_no_dre , phase_accum_no_dre];


        %Reset variable for next pulse
        I_samp = [];
        Q_samp = [];
        D_samp = [];
        num_samples = 0;

      elseif (acquire == 1)

        %Continue to acquire data samples
        num_samples = num_samples + 1;

        I_samp = [I_samp, I_data(i)];
        Q_samp = [Q_samp, Q_data(i)];
        D_samp = [D_samp, data(i)];

      end;

end;

%subtract out dc offset
%demod = demod - (max(demod)+min(demod))/2;

%figure;
%plot(ts, window,'r',ts, pulsed_carrier,'g');

%figure;
%plot(tsamp, demod,'r')

% if 0
%   figure;
```

```
%    NFFT=1024*2^10;
%     f = fs/2*linspace(0,1,NFFT/2+1);
%    Y = 20*log10(2*abs(fft(window,NFFT))/NFFT);
%     plot(f,Y(1:NFFT/2+1));
%     xlim([0  12e6]);
%     ylim([-100  0]);
% end;
%
% if 0
%     figure;
%    NFFT=1024*2^10;
%     f = fs/2*linspace(0,1,NFFT/2+1);
%    Y = 20*log10(2*abs(fft(pulsed_carrier,NFFT))/NFFT);
%     plot(f,Y(1:NFFT/2+1));
%     xlim([8e6  12e6]);
%     ylim([-100  0]);
% end;
%
figure;
NFFT = cycles;
win = hanning(NFFT)';
f = fsamp/2*linspace(0,1,NFFT/2+1);
if isempty(Y_curr) == 1
   Y_curr = 20*log10((2*abs(fft(win.*demod,NFFT))/NFFT)/1e-6);
   plot(f,Y_curr(1:NFFT/2+1),'r');
else
   Y_last = Y_curr;
   Y_curr = 20*log10((2*abs(fft(win.*demod,NFFT))/NFFT)/1e-6);
   plot(f,Y_last(1:NFFT/2+1),'g',f,Y_curr(1:NFFT/2+1),'r');
end;
xlim([0  320e3]);
ylim([-20  200]);

%figure;
%plot(sig);

% figure;
% subplot(5,1,1);
% plot(tsamp,demod,'b');
```

```
% title('demod');
% subplot(5,1,2);
% plot(tsamp,diff_lst,'r');
% title('diff_lst');
% subplot(5,1,3);
% plot(tsamp,sig_sampled,'k');
% title('sig_orig');
% subplot(5,1,4);
% plot(tsamp,[0,diff(demod)],'r');
% title('diff_of_demod');
% subplot(5,1,5);
% plot(tsamp,DIFM_lst,'g');
% title('DIFM_lst');

%plot(tsamp,demod,'b', tsamp,diff_lst,'r+', tsamp,sig_sampled,'k', ...
%        tsamp,[0,diff(demod)],'b', tsamp, DIFM_lst, 'g');

figure;
[haxes,hline1,hline2] = plotyy(tsamp,sig_sampled,tsamp,DIFM_lst);
set(hline2,'LineStyle','--');
xlabel('Time (s)');
axes(haxes(1));
ylabel('Radians');
ylim([-.5 .5]);
axes(haxes(2));
ylabel('y\_out(n)');
ylim([ -.4 -.2]);
legend('y\_out(n)','Input Waveform');

figure;
subplot(2,1,1);
plot(tsamp, sig_sampled,'r',tsamp,demod_no_dre,'g*-');
ylabel('Amplitude(Radians)','FontSize',24);
legend('Input Waveform ', 'DRE Disabled Output')
set(gca,'FontSize', 18);
subplot(2,1,2);
plot(tsamp, sig_sampled,'r',tsamp,demod,'g*-');
ylabel('Amplitude(Radians)','FontSize',24);
set(gca,'FontSize', 18);
```

```
xlabel('Time (s)','FontSize',24);
legend('Input Waveform ', 'DRE Enabled Output')

cnr = 20*log10(Ac*2/(An))
error = 20*log10(max(demod)/max(sig))
db_ext = 20*log10(fr_sig/fr_demod)
max_difm = max(DIFM_lst)
min_difm = min(DIFM_lst)
mean_difm = mean(DIFM_lst)
diff_difm = max(DIFM_lst) - min(DIFM_lst)
```

Appendix C DFT MATLAB Simulation Code

Listing C.1: DFT MATLAB simulation code

```
%Use FIR (odd) filter or (even) simple BOX FIR filter
filt_en = 0;

%Set time series and sample rate parameters
N = 8;
M = 1;
cycles = 64*N; %fsamp samples
fc = 10e6*M; %10nsec
pw = 76*M; %10nsec
delay = 10*M; %10nsec
samples = 50*M+1;

%Set digiziter parameters
dig_bits = 16;
peak_dig = 2^(dig_bits-1);
iq_bits = 16;
peak_iq = 2^(iq_bits-1);
fir_bits = 16;
peak_fir = 2^(fir_bits-1);

%Set the digitization sample rate
fs = 100e6*M;
ts = (0:(1/fs):(1/fs)*pw*(cycles)*2);
ts = ts(1:end-1);

%Time series of individual acquired pulses
t_ext = (0:(1/fs):(1/fs)*(samples-1));

%Time series of demodulated pulses
fsamp = 1/(pw*2*(1/fs));
tsamp = (0:(1/fsamp):(1/fsamp)*(cycles));
tsamp = tsamp(1:end-1);
fr_demod = fsamp*pi

%Window the input signal being demodulated
%to avoid initial transients
data_win = tukeywin(size(ts,2),1)';
```

```
data_win_sampled = tukeywin(size(tsamp,2),1)';

%Window the individual pulses to simulate
%the ramp and fall times of the carrier
win = tukeywin(pw,.1)';

%Create the time series windows to sample the
%incoming signal
window = [];
for i = 0:cycles-1
  window = [ window, win ];
  window = [ window, zeros(pw,1)' ];
end;

%Window the acquired samples of the pulses
%to reduce error
%iq_win = ones(samples,1)';
%iq_win = tukeywin(samples,1)';
%iq_win = blackman(samples)';
%iq_win = flattopwin(samples)';
%iq_win = hanning(samples)';
iq_win = nuttallwin(samples)';
iq_win = floor(iq_win.*peak_fir);
box_win = nuttallwin(samples-1)';
box_win = floor(box_win.*peak_fir);

%Create the low-pass filters if simple BOX averaging
%filter is not used
%Enable remez or firpm if signal toolbox is available
if filt_en == 1
%   n_filt = samples-1;
%   fnyq = fs/2;
%   fch = 18e6; %20MHz null
%   fcl = 2e6; %3MHz bandwidth max
%   f = [0 (fcl/fnyq) (fch/fnyq) 1];
%   w = [1 1 0 0];
%   b = remez(n_filt, f, w);
%   b = floor(b*peak_fir);
    a = 1;
```

```
    fir = load('fir_51pt.mat','b');
    b = fir.b;
%   figure;
%   freqz(b);
end;
fir = load('fir_51pt.mat','b');

%Create the ambient noise shaping low-pass filters
%Enable remez or firpm if signal toolbox is available
n_filt = 1000;
fnyq = fs/2;
fch = 200e3; %20MHz null
fcl = 1e3; %3MHz bandwidth max
f = [0 (fcl/fnyq) (fch/fnyq) 1];
w = [1 1 0 0];
%bn = remez(n_filt, f, w);
h = load('filt_coeff_1k_50k_8001.mat','h');
bn = h.h;
an = 1;
%figure;
%freqz(bn);

%Carrier amplitude for CNR testing and
%autocorrelation correction
Ac = .5;

%Create signal and noise waveforms
Asig = 160;
fsig = 10e3;
phi = 0;
fr_sig = 2*pi*Asig*fsig
bw = Asig*fsig

%Signal noise
An_sig = 25000;
sig_noise = filter(bn, an, An_sig*(rand(size(ts))-.5));
sig_noise = filter(bn, an, sig_noise);
sig_noise = filter(bn, an, sig_noise);
```

```
%Carrier noise
An = .01;
fn = 10e6+157e3;
phin = 0;
%noise = An*sin(2*pi*fn*ts + phin);
noise = An*(rand(size(ts))-.5);

%Create multitone noise components (if used)
An1 = 0.0001;
fn1 = 10e6+157e3;
An2 = 0.0001;
fn2 = 10e6-157e3;
An3 = 0.0001;
fn3 = 157e3;

%noise = An1*sin(2*pi*fn1*ts) + An2*sin(2*pi*fn2*ts) + An3*sin(2*pi*fn3*ts);

%Create the pulsed carrier waveform
%used for testing the carrier spectrum
pulsed_carrier = sin(2*pi*fc*ts).*window - .5;

%Create the "analog" signal and only keep
%data at the pulses
sig = (Asig*sin(2*pi*fsig*ts + phi) + sig_noise ).*data_win;
data = (Ac*sin(2*pi*fc*ts + sig )).*window + noise;

%Create a copy of the incoming signal at the
%actual demodulation rate for comparison testing
%of the output
%sig_sampled = Asig*sin(2*pi*fsig*tsamp).*data_win_sampled;
sig_sampled = [];
for i = 1:size(tsamp,2)
  sig_sampled = [sig_sampled sig(pw+(i-1)*pw*2)];
end

%Digitize the acquired pulses
data = floor(data*peak_dig);

%Create the digital I/Q components
```

```
I = floor(cos(2*pi*fc*ts)*peak_iq);
Q = floor(sin(2*pi*fc*ts)*peak_iq);
I_data = I.*data;
Q_data = Q.*data;

%Initialize loop parameters
acquire = 0;
delay_cnt = 0;
num_samples = 0;
phase_last = 0;
phase_cur = 0;
phase_diff = 0;
phase_accum = 0;
phase_accum_no_dre = 0;
phase_cf = 0;
demod = [];
demod_no_dre = [];
I_samp = [];
Q_samp = [];
D_samp = [];
diff_lst = [];

%Create Fourier components
pl1  = fc - 19*fsamp/4;
pl2  = fc - 15*fsamp/4;
pl3  = fc - 11*fsamp/4;
pl4  = fc - 7*fsamp/4;
pl5  = fc - 3*fsamp/4;
pl6  = fc + 1*fsamp/4;
pl7  = fc + 5*fsamp/4;
pl8  = fc + 9*fsamp/4;
pl9  = fc + 13*fsamp/4;
pl10 = fc + 17*fsamp/4;
pl11 = fc + 21*fsamp/4;

nl1  = fc - 21*fsamp/4;
nl2  = fc - 17*fsamp/4;
nl3  = fc - 13*fsamp/4;
nl4  = fc - 9*fsamp/4;
```

```
nl5  = fc - 5*fsamp/4;
nl6  = fc - 1*fsamp/4;
nl7  = fc + 3*fsamp/4;
nl8  = fc + 7*fsamp/4;
nl9  = fc + 11*fsamp/4;
nl10 = fc + 15*fsamp/4;
nl11 = fc + 19*fsamp/4;

DFT_pc1 = [];
DFT_nc1 = [];
DFT_pc2 = [];
DFT_nc2 = [];
DFT_pc3 = [];
DFT_nc3 = [];
DFT_pc4 = [];
DFT_nc4 = [];
DFT_pc5 = [];
DFT_nc5 = [];
DFT_pc6 = [];
DFT_nc6 = [];
DFT_pc7 = [];
DFT_nc7 = [];
DFT_pc8 = [];
DFT_nc8 = [];
DFT_pc9 = [];
DFT_nc9 = [];
DFT_pc10 = [];
DFT_nc10 = [];
DFT_pc11 = [];
DFT_nc11 = [];

%AVG must be 2 or more
navg = 2;
p1_buf = zeros(navg,1)';
n1_buf = zeros(navg,1)';
p2_buf = zeros(navg,1)';
n2_buf = zeros(navg,1)';
p3_buf = zeros(navg,1)';
n3_buf = zeros(navg,1)';
```

```
p4_buf = zeros(navg,1)';
n4_buf = zeros(navg,1)';
p5_buf = zeros(navg,1)';
n5_buf = zeros(navg,1)';
p6_buf = zeros(navg,1)';
n6_buf = zeros(navg,1)';
p7_buf = zeros(navg,1)';
n7_buf = zeros(navg,1)';
p8_buf = zeros(navg,1)';
n8_buf = zeros(navg,1)';
p9_buf = zeros(navg,1)';
n9_buf = zeros(navg,1)';
p10_buf = zeros(navg,1)';
n10_buf = zeros(navg,1)';
p11_buf = zeros(navg,1)';
n11_buf = zeros(navg,1)';

n7_buf(2) = 4.459e9;
p5_buf(2) = 4.459e9;

n6_buf(2) = 4.67e9;
p6_buf(2) = 4.67e9;

n5_buf(2) = 4.405e9;
p7_buf(2) = 4.405e9;

%Process over all digitized samples of
%the incoming carrier signal
for i = 1:pw*cycles*2

    %Only select samples for demodulation within
    %the specified window
    if ( delay_cnt >= delay )&&( delay_cnt <= delay+samples-1 )
      acquire = 1;
    else
      acquire = 0;
    end;

    %The sample window starts on the rising edge of
```

```
%received optical pulse
if ( window(i) > .5 )
  delay_cnt = delay_cnt + 1;
else
  delay_cnt = 0;
end;

%The number of specified digital samples has been
%received, begin demodulating the pulse
if ( num_samples == samples-1 ) && ( acquire == 1 )

  phase_last = phase_cur;

  %Obtain I/Q components and the carrier signal for DR ext
  I_samp = [I_samp, I_data(i)];
  Q_samp = [Q_samp, Q_data(i)];
  D_samp = [D_samp, data(i)];

  %If filter enable is enabled, used an N (odd) point
  %FIR filter to process the I/Q data, otherwise use
  %use and N (even) point BOX FIR filter
  if filt_en == 1
    i_filt = filter(b,a,I_samp);
    q_filt = filter(b,a,Q_samp);
    phase_cur = atan2(i_filt(end),q_filt(end));
  else
    i_sum = sum(I_samp(1:end-1).*box_win);
    q_sum = sum(Q_samp(1:end-1).*box_win);
    phase_cur = atan2(i_sum,q_sum);
  end;

  %Compute the phase change and unwrap the signal
  phase_diff = phase_cur - phase_last;
  if ( phase_diff > pi )
    phase_diff = phase_diff - 2*pi;
  elseif ( phase_diff < -pi )
    phase_diff = phase_diff + 2*pi;
  end;
```

```
diff_lst = [diff_lst, phase_diff];

p_lst = [];
n_lst = [];

%%Extension approach
fr_c  = cos(2*pi*pl1*t_ext).*D_samp.*iq_win;
fr_s  = sin(2*pi*pl1*t_ext).*D_samp.*iq_win;
fr_l = sqrt(sum(fr_s)^2 + sum(fr_c)^2);
p1_buf = [p1_buf(2:end), fr_l];
p1_avg = mean(p1_buf);
DFT_pc1 = [DFT_pc1, p1_avg];
p_lst = [p_lst, p1_avg];

fr_c  = cos(2*pi*nl1*t_ext).*D_samp.*iq_win;
fr_s  = sin(2*pi*nl1*t_ext).*D_samp.*iq_win;
fr_l = sqrt(sum(fr_s)^2 + sum(fr_c)^2);
n1_buf = [n1_buf(2:end), fr_l];
n1_avg = mean(n1_buf);
DFT_nc1 = [DFT_nc1, n1_avg];
n_lst = [n_lst, n1_avg];

fr_c  = cos(2*pi*pl2*t_ext).*D_samp.*iq_win;
fr_s  = sin(2*pi*pl2*t_ext).*D_samp.*iq_win;
fr_l = sqrt(sum(fr_s)^2 + sum(fr_c)^2);
p2_buf = [p2_buf(2:end), fr_l];
p2_avg = mean(p2_buf);
DFT_pc2 = [DFT_pc2, p2_avg];
p_lst = [p_lst, p2_avg];

fr_c  = cos(2*pi*nl2*t_ext).*D_samp.*iq_win;
fr_s  = sin(2*pi*nl2*t_ext).*D_samp.*iq_win;
fr_l = sqrt(sum(fr_s)^2 + sum(fr_c)^2);
n2_buf = [n2_buf(2:end), fr_l];
n2_avg = mean(n2_buf);
DFT_nc2 = [DFT_nc2, n2_avg];
n_lst = [n_lst, n2_avg];

fr_c  = cos(2*pi*pl3*t_ext).*D_samp.*iq_win;
```

```
fr_s  = sin(2*pi*pl3*t_ext).*D_samp.*iq_win;
fr_l = sqrt(sum(fr_s)^2 + sum(fr_c)^2);
p3_buf = [p3_buf(2:end), fr_l];
p3_avg = mean(p3_buf);
DFT_pc3 = [DFT_pc3, p3_avg];
p_lst = [p_lst, p3_avg];

fr_c  = cos(2*pi*nl3*t_ext).*D_samp.*iq_win;
fr_s  = sin(2*pi*nl3*t_ext).*D_samp.*iq_win;
fr_l = sqrt(sum(fr_s)^2 + sum(fr_c)^2);
n3_buf = [n3_buf(2:end), fr_l];
n3_avg = mean(n3_buf);
DFT_nc3 = [DFT_nc3, n3_avg];
n_lst = [n_lst, n3_avg];

fr_c  = cos(2*pi*pl4*t_ext).*D_samp.*iq_win;
fr_s  = sin(2*pi*pl4*t_ext).*D_samp.*iq_win;
fr_l = sqrt(sum(fr_s)^2 + sum(fr_c)^2);
p4_buf = [p4_buf(2:end), fr_l];
p4_avg = mean(p4_buf);
DFT_pc4 = [DFT_pc4, p4_avg];
p_lst = [p_lst, p4_avg];

fr_c  = cos(2*pi*nl4*t_ext).*D_samp.*iq_win;
fr_s  = sin(2*pi*nl4*t_ext).*D_samp.*iq_win;
fr_l = sqrt(sum(fr_s)^2 + sum(fr_c)^2);
n4_buf = [n4_buf(2:end), fr_l];
n4_avg = mean(n4_buf);
DFT_nc4 = [DFT_nc4, n4_avg];
n_lst = [n_lst, n4_avg];

fr_c  = cos(2*pi*pl5*t_ext).*D_samp.*iq_win;
fr_s  = sin(2*pi*pl5*t_ext).*D_samp.*iq_win;
fr_l = sqrt(sum(fr_s)^2 + sum(fr_c)^2);
p5_buf = [p5_buf(2:end), fr_l];
p5_avg = mean(p5_buf);
DFT_pc5 = [DFT_pc5, p5_avg];
p_lst = [p_lst, p5_avg];
```

```
fr_c  = cos(2*pi*nl5*t_ext).*D_samp.*iq_win;
fr_s  = sin(2*pi*nl5*t_ext).*D_samp.*iq_win;
fr_l = sqrt(sum(fr_s)^2 + sum(fr_c)^2);
n5_buf = [n5_buf(2:end), fr_l];
n5_avg = mean(n5_buf);
DFT_nc5 = [DFT_nc5, n5_avg];
n_lst = [n_lst, n5_avg];

fr_c  = cos(2*pi*pl6*t_ext).*D_samp.*iq_win;
fr_s  = sin(2*pi*pl6*t_ext).*D_samp.*iq_win;
fr_l = sqrt(sum(fr_s)^2 + sum(fr_c)^2);
p6_buf = [p6_buf(2:end), fr_l];
p6_avg = mean(p6_buf);
DFT_pc6 = [DFT_pc6, p6_avg];
p_lst = [p_lst, p6_avg];

fr_c  = cos(2*pi*nl6*t_ext).*D_samp.*iq_win;
fr_s  = sin(2*pi*nl6*t_ext).*D_samp.*iq_win;
fr_l = sqrt(sum(fr_s)^2 + sum(fr_c)^2);
n6_buf = [n6_buf(2:end), fr_l];
n6_avg = mean(n6_buf);
DFT_nc6 = [DFT_nc6, n6_avg];
n_lst = [n_lst, n6_avg];

fr_c  = cos(2*pi*pl7*t_ext).*D_samp.*iq_win;
fr_s  = sin(2*pi*pl7*t_ext).*D_samp.*iq_win;
fr_l = sqrt(sum(fr_s)^2 + sum(fr_c)^2);
p7_buf = [p7_buf(2:end), fr_l];
p7_avg = mean(p7_buf);
DFT_pc7 = [DFT_pc7, p7_avg];
p_lst = [p_lst, p7_avg];

fr_c  = cos(2*pi*nl7*t_ext).*D_samp.*iq_win;
fr_s  = sin(2*pi*nl7*t_ext).*D_samp.*iq_win;
fr_l = sqrt(sum(fr_s)^2 + sum(fr_c)^2);
n7_buf = [n7_buf(2:end), fr_l];
n7_avg = mean(n7_buf);
DFT_nc7 = [DFT_nc7, n7_avg];
n_lst = [n_lst, n7_avg];
```

```
fr_c  = cos(2*pi*pl8*t_ext).*D_samp.*iq_win;
fr_s  = sin(2*pi*pl8*t_ext).*D_samp.*iq_win;
fr_l = sqrt(sum(fr_s)^2 + sum(fr_c)^2);
p8_buf = [p8_buf(2:end), fr_l];
p8_avg = mean(p8_buf);
DFT_pc8 = [DFT_pc8, p8_avg];
p_lst = [p_lst, p8_avg];

fr_c  = cos(2*pi*nl8*t_ext).*D_samp.*iq_win;
fr_s  = sin(2*pi*nl8*t_ext).*D_samp.*iq_win;
fr_l = sqrt(sum(fr_s)^2 + sum(fr_c)^2);
n8_buf = [n8_buf(2:end), fr_l];
n8_avg = mean(n8_buf);
DFT_nc8 = [DFT_nc8, n8_avg];
n_lst = [n_lst, n8_avg];

fr_c  = cos(2*pi*pl9*t_ext).*D_samp.*iq_win;
fr_s  = sin(2*pi*pl9*t_ext).*D_samp.*iq_win;
fr_l = sqrt(sum(fr_s)^2 + sum(fr_c)^2);
p9_buf = [p9_buf(2:end), fr_l];
p9_avg = mean(p9_buf);
DFT_pc9 = [DFT_pc9, p9_avg];
p_lst = [p_lst, p9_avg];

fr_c  = cos(2*pi*nl9*t_ext).*D_samp.*iq_win;
fr_s  = sin(2*pi*nl9*t_ext).*D_samp.*iq_win;
fr_l = sqrt(sum(fr_s)^2 + sum(fr_c)^2);
n9_buf = [n9_buf(2:end), fr_l];
n9_avg = mean(n9_buf);
DFT_nc9 = [DFT_nc9, n9_avg];
n_lst = [n_lst, n9_avg];

fr_c  = cos(2*pi*pl10*t_ext).*D_samp.*iq_win;
fr_s  = sin(2*pi*pl10*t_ext).*D_samp.*iq_win;
fr_l = sqrt(sum(fr_s)^2 + sum(fr_c)^2);
p10_buf = [p10_buf(2:end), fr_l];
p10_avg = mean(p10_buf);
DFT_pc10 = [DFT_pc10, p10_avg];
```

```
p_lst = [p_lst, p10_avg];

fr_c  = cos(2*pi*nl10*t_ext).*D_samp.*iq_win;
fr_s  = sin(2*pi*nl10*t_ext).*D_samp.*iq_win;
fr_l = sqrt(sum(fr_s)^2 + sum(fr_c)^2);
n10_buf = [n10_buf(2:end), fr_l];
n10_avg = mean(n10_buf);
DFT_nc10 = [DFT_nc10, n10_avg];
n_lst = [n_lst, n10_avg];

fr_c  = cos(2*pi*pl11*t_ext).*D_samp.*iq_win;
fr_s  = sin(2*pi*pl11*t_ext).*D_samp.*iq_win;
fr_l = sqrt(sum(fr_s)^2 + sum(fr_c)^2);
p11_buf = [p11_buf(2:end), fr_l];
p11_avg = mean(p11_buf);
DFT_pc11 = [DFT_pc11, p11_avg];
p_lst = [p_lst, p11_avg];

fr_c  = cos(2*pi*nl11*t_ext).*D_samp.*iq_win;
fr_s  = sin(2*pi*nl11*t_ext).*D_samp.*iq_win;
fr_l = sqrt(sum(fr_s)^2 + sum(fr_c)^2);
n11_buf = [n11_buf(2:end), fr_l];
n11_avg = mean(n11_buf);
DFT_nc11 = [DFT_nc11, n11_avg];
n_lst = [n_lst, n11_avg];

%Determine direction of rotation and select
%peak DFT coeff from appropriate list
if ( phase_diff > 0 )
  [max_val,fr_index] = max(p_lst);
 else
  [max_val,fr_index] = max(n_lst);
end

%Select correction factor
if fr_index == 11
  phase_cf = 10*pi;
elseif fr_index == 10
  phase_cf = 8*pi;
```

```
  elseif fr_index == 9
    phase_cf = 6*pi;
  elseif fr_index == 8
    phase_cf = 4*pi;
  elseif fr_index == 7
    phase_cf = 2*pi;
  elseif fr_index == 6
    phase_cf = 0*pi;
  elseif fr_index == 5
    phase_cf = -2*pi;
  elseif fr_index == 4
    phase_cf = -4*pi;
  elseif fr_index == 3
    phase_cf = -6*pi;
  elseif fr_index == 2
    phase_cf = -8*pi;
  else
    phase_cf = -10*pi;
  end;

  %Accumulate the phase using the DR extension
  %correction factor
  phase_accum = phase_accum + phase_diff + phase_cf;
  demod = [demod , phase_accum];

  phase_accum_no_dre = phase_accum_no_dre + phase_diff;
  demod_no_dre = [demod_no_dre , phase_accum_no_dre];

  %Reset variable for next pulse
  I_samp = [];
  Q_samp = [];
  D_samp = [];
  num_samples = 0;

elseif (acquire == 1)

  %Continue to acquire data samples
  num_samples = num_samples + 1;
```

```
        I_samp = [I_samp, I_data(i)];
        Q_samp = [Q_samp, Q_data(i)];
        D_samp = [D_samp, data(i)];

    end;

end;

%subtract out dc offset
%demod = demod - (max(demod)+min(demod))/2;

%figure;
%plot(ts, window,'r',ts, pulsed_carrier,'g');

%figure;
%plot(tsamp, demod,'r')

% if 0
%   figure;
%   NFFT=1024*2^10;
%   f = fs/2*linspace(0,1,NFFT/2+1);
%   Y = 20*log10(2*abs(fft(window,NFFT))/NFFT);
%   plot(f,Y(1:NFFT/2+1));
%   xlim([0 12e6]);
%   ylim([-100 0]);
% end;
%
% if 0
%   figure;
%   NFFT=1024*2^10;
%   f = fs/2*linspace(0,1,NFFT/2+1);
%   Y = 20*log10(2*abs(fft(pulsed_carrier,NFFT))/NFFT);
%   plot(f,Y(1:NFFT/2+1));
%   xlim([8e6 12e6]);
%   ylim([-100 0]);
% end;

 figure;
NFFT = cycles;
```

```
win = hanning(NFFT)';
f = fsamp/2*linspace(0,1,NFFT/2+1);
if isempty(Y_curr) == 1
   Y_curr = 20*log10((2*abs(fft(win.*demod,NFFT))/NFFT)/1e-6);
   plot(f,Y_curr(1:NFFT/2+1),'r');
else
   Y_last = Y_curr;
   Y_curr = 20*log10((2*abs(fft(win.*demod,NFFT))/NFFT)/1e-6);
   plot(f,Y_last(1:NFFT/2+1),'g',f,Y_curr(1:NFFT/2+1),'r');
end;
xlim([0 320e3]);
ylim([-20 200]);

%figure;
%plot(sig);

% figure;
% subplot(5,1,1);
% plot(tsamp,demod,'b');
% title('demod');
% subplot(5,1,2);
% plot(tsamp,diff_lst,'r');
% title('diff_lst');
% subplot(5,1,3);
% plot(tsamp,sig_sampled,'k');
% title('sig_orig');
% subplot(5,1,4);
% plot(tsamp,[0,diff(demod)],'r');
% title('diff_of_demod');
% subplot(5,1,5);
% plot(tsamp,DFT_nc6,'g',tsamp,DFT_pc6,'r');
% title('DFT_pc6');

%plot(tsamp,demod,'b', tsamp,diff_lst,'r+', tsamp,sig_sampled,'k', ...
%        tsamp,[0,diff(demod)],'b', tsamp, DIFM_lst, 'g');

%figure;
%[haxes,hline1,hline2] = plotyy(tsamp,sig_sampled,tsamp,DFT_nc6);
%[haxes,hline1,hline2] = plotyy(tsamp,DFT_pc6,tsamp,DFT_nc6);
```

```
%set(hline2,'LineStyle','--');
%xlabel('Time (s)');
%axes(haxes(1));
%ylabel('Radians');
%axes(haxes(2));
%ylabel('y_out[k]');
%legend('Input Waveform','y_out');
%offset = 3000;
%scale = min(DFT_nc7)/1000;
%plot(tsamp, sig_sampled, 'm', ...
%     tsamp, DFT_pc6/scale - offset, 'r', ...
%     tsamp, DFT_nc6/scale - offset, 'g', ...
%     tsamp, DFT_pc5/scale - offset, 'b', ...
%     tsamp, DFT_nc7/scale - offset, 'k');

% figure;
% subplot(2,1,1);
% plot(tsamp, sig_sampled);
% ylabel('Input Waveform (Radians)','FontSize',24);
% xlim([2e-4 4e-4]);
% set(gca,'FontSize', 18);
% subplot(2,1,2);
%%% plot(tsamp, DFT_pc6, '-ro', tsamp, DFT_nc6,'-g*', ...
%%%       tsamp, DFT_pc5, '-bd', tsamp, DFT_nc7,'-kx');
% plot(tsamp, DFT_pc6, '-r', tsamp, DFT_nc6,'--g', ...
%      tsamp, DFT_pc5, '-.b', tsamp, DFT_nc7,':k');
% ylabel('DFT\_COEFF','FontSize',24);
% set(gca,'FontSize', 18);
% xlabel('Time (s)','FontSize',24);
% legend('DFT\_P1','DFT\_N1','DFT\_P2','DFT\_N2');
% xlim([2e-4 4e-4]);

figure;
subplot(2,1,1);
plot(tsamp, sig_sampled,'r',tsamp,demod_no_dre,'g*-');
ylabel('Amplitude(Radians)','FontSize',24);
legend('Input Waveform ', 'DRE Disabled Output')
set(gca,'FontSize', 18);
subplot(2,1,2);
```

```
plot(tsamp, sig_sampled,'r',tsamp,demod,'g*-');
ylabel('Amplitude(Radians)','FontSize',24);
set(gca,'FontSize', 18);
xlabel('Time (s)','FontSize',24);
legend('Input Waveform ', 'DRE Enabled Output')

cnr = 20*log10(Ac*2/(An))
error = 20*log10(max(demod)/max(sig))
db_ext = 20*log10(fr_sig/fr_demod)
max_dft = max(DFT_pc1)
min_dft = min(DFT_pc1)
```

Appendix D PECM MATLAB Simulation Code

Listing D.1: PECM MATLAB simulation code

```
%Use FIR (odd) filter or (even) simple BOX FIR filter
filt_en = 0;

%Set time series and sample rate parameters
N = 1;
M = 5;
cycles = 64*N; %fsamp samples
fc = 10e6*1; %10nsec
pw = 76*M; %10nsec
delay = 10*M; %10nsec
if filt_en == 0
  samples = 50*M;
else
  samples = 50*M+1;
end;

%Set digiziter parameters
dig_bits = 16;
peak_dig = 2^(dig_bits-1);
iq_bits = 16;
peak_iq = 2^(iq_bits-1);
fir_bits = 16;
peak_fir = 2^(fir_bits-1);

%Set the digitization sample rate
fs = 100e6*M;
ts = (0:(1/fs):(1/fs)*pw*(cycles)*2);
ts = ts(1:end-1);

%Time series of individual acquired pulses
t_ext = (0:(1/fs):(1/fs)*(samples-1));

%Time series of demodulated pulses
fsamp = 1/(pw*2*(1/fs));
tsamp = (0:(1/fsamp):(1/fsamp)*(cycles));
tsamp = tsamp(1:end-1);
fr_demod = fsamp*pi
```

```
%Window the input signal being demodulated
%to avoid initial transients
data_win = tukeywin(size(ts,2),1)';
data_win_sampled = tukeywin(size(tsamp,2),1)';

%Window the individual pulses to simulate
%the ramp and fall times of the carrier
win = tukeywin(pw,.1)';

%Create the time series windows to sample the
%incoming signal
window = [];
for i = 0:cycles-1
  window = [ window, win ];
  window = [ window, zeros(pw,1)' ];
end;

%Window the acquired samples of the pulses
%to reduce error
%iq_win = tukeywin(samples,1)';
%iq_win = blackman(samples)';
%iq_win = flattopwin(samples)';

%Nuttall window
n = (1:1:samples);
N = samples - 1;
a0 = 0.355768;
a1 = 0.487396;
a2 = 0.144232;
a3 = 0.012604;
iq_win = a0 - a1*cos(2*pi.*n/N) + ...
         a2*cos(4*pi.*n/N) - a3*cos(6*pi.*n/N);
iq_win = floor(iq_win.*peak_fir);


%Create the low-pass filters if simple BOX averaging
%filter is not used
if filt_en == 1
```

```
    n_filt = samples-1;
    fnyq = fs/2;
    fch = 18e6; %20MHz null
    fcl = 2e6; %3MHz bandwidth max
    f = [0 (fcl/fnyq) (fch/fnyq) 1];
    w = [1 1 0 0];
    b = remez(n_filt, f, w);
    b = floor(b*peak_fir);
    a = 1;
    %figure;
    %freqz(b);
end;

%Carrier amplitude for CNR testing and
%autocorrelation correction
Ac = .5;

%Create signal and noise waveforms
Asig = 32;
fsig = 100e3;
phi = 0;
fr_sig = 2*pi*Asig*fsig
bw = Asig*fsig
An = .001;
fn = 10e6+157e3;
phin = 0;
%noise = An*sin(2*pi*fn*ts + phin);
noise = An*(rand(size(ts))-.5);

%Create multitone noise components (if used)
An1 = 0.0001;
fn1 = 10e6+157e3;
An2 = 0.0002;
fn2 = 10e6-157e3;
An3 = 0.001;
fn3 = 157e3;

%noise = An1*sin(2*pi*fn1*ts) + An2*sin(2*pi*fn2*ts) + An3*sin(2*pi*fn3*ts);
```

```
%Create the pulsed carrier waveform
%used for testing the carrier spectrum
pulsed_carrier = sin(2*pi*fc*ts).*window - .5;

%Create a copy of the incoming signal at the
%actual demodulation rate for comparison testing
%of the output
sig_sampled = Asig*sin(2*pi*fsig*tsamp).*data_win_sampled;

%Create the "analog" signal and only keep
%data at the pulses
sig = Asig*sin(2*pi*fsig*ts + phi).*data_win;
data = (Ac*sin(2*pi*fc*ts + sig )).*window + noise;

%Digitize the acquired pulses
data = floor(data*peak_dig);

%Create the digital I/Q components
I = floor(cos(2*pi*fc*ts)*peak_iq);
Q = floor(sin(2*pi*fc*ts)*peak_iq);
I_data = I.*data;
Q_data = Q.*data;

%Initialize loop parameters
acquire = 0;
delay_cnt = 0;
num_samples = 0;
phase_last = 0;
phase_cur = 0;
phase_diff = 0;
phase_accum = 0;
phase_cf = 0;
demod = [];
I_samp = [];
Q_samp = [];
D_samp = [];
diff_lst = [];

%Initial DR extension variables
```

```
%AVG must be 2 or more
navg = 2;
PECM_lst = [];
PECM_cur = 0;

%Process over all digitized samples of
%the incoming carrier signal
for i = 1:pw*cycles*2

    %Only select samples for demodulation within
    %the specified window
    if ( delay_cnt >= delay )&&( delay_cnt <= delay+samples-1 )
      acquire = 1;
    else
      acquire = 0;
    end;

    %The sample window starts on the rising edge of
    %received optical pulse
    if ( window(i) > .5 )
      delay_cnt = delay_cnt + 1;
    else
      delay_cnt = 0;
    end;

    %The number of specified digital samples has been
    %received, begin demodulating the pulse
    if ( num_samples == samples-1 ) && ( acquire == 1 )

      phase_last = phase_cur;

      %Obtain I/Q components and the carrier signal for DR ext
      I_samp = [I_samp, I_data(i)];
      Q_samp = [Q_samp, Q_data(i)];
      D_samp = [D_samp, data(i)];

      %If filter enable is enabled, used an N (odd) point
      %FIR filter to process the I/Q data, otherwise use
      %use and N (even) point BOX FIR filter
```

```
if filt_en == 1
  i_filt = filter(b,a,I_samp);
  q_filt = filter(b,a,Q_samp);
  phase_cur = atan2(i_filt(end),q_filt(end));
else
  i_sum = sum(I_samp.*iq_win);
  q_sum = sum(Q_samp.*iq_win);
  phase_cur = atan2(i_sum,q_sum);
end;

%Compute the phase change and unwrap the signal
phase_diff = phase_cur - phase_last;
if ( phase_diff > pi )
  phase_diff = phase_diff - 2*pi;
elseif ( phase_diff < -pi )
  phase_diff = phase_diff + 2*pi;
end;

diff_lst = [diff_lst, phase_diff];

phase_cf = 0;

PECM_last = PECM_cur;
for j = 1:samples
 if ( D_samp(j) < 0 ) && ( D_samp(j+1) > 0 )
   PECM_cur = D_samp(j) + D_samp(j+(fs/fc)/2);
   PECM_cur = PECM_cur/max(D_samp);
   break;
 end;
end;
PECM_avg = (PECM_last+PECM_cur)/2;
PECM_lst = [PECM_lst PECM_avg];


%Accumulate the phase using the DR extension
%correction factor
phase_accum = phase_accum + phase_diff + phase_cf;
demod = [demod , phase_accum];
```

```
        %Reset variable for next pulse
        I_samp = [];
        Q_samp = [];
        D_samp = [];
        num_samples = 0;

      elseif (acquire == 1)

        %Continue to acquire data samples
        num_samples = num_samples + 1;

        I_samp = [I_samp, I_data(i)];
        Q_samp = [Q_samp, Q_data(i)];
        D_samp = [D_samp, data(i)];

      end;

end;

%subtract out dc offset
%demod = demod - (max(demod)+min(demod))/2;

%figure;
%plot(ts, window,'r',ts, pulsed_carrier,'g');

%figure;
%plot(tsamp, demod,'r')

if 0
   figure;
   NFFT=1024*2^10;
   f = fs/2*linspace(0,1,NFFT/2+1);
   Y = 20*log10(2*abs(fft(window,NFFT))/NFFT);
   plot(f,Y(1:NFFT/2+1));
   xlim([0 12e6]);
   ylim([-100 0]);
end;

if 0
```

```
    figure;
    NFFT=1024*2^10;
    f = fs/2*linspace(0,1,NFFT/2+1);
    Y = 20*log10(2*abs(fft(pulsed_carrier,NFFT))/NFFT);
    plot(f,Y(1:NFFT/2+1));
    xlim([8e6 12e6]);
    ylim([-100 0]);
end;

% figure;
% NFFT = cycles;
% win = hanning(NFFT)';
% f = fsamp/2*linspace(0,1,NFFT/2+1);
% if isempty(Y_curr) == 1
%    Y_curr = 20*log10((2*abs(fft(win.*demod,NFFT))/NFFT)/1e-6);
%    plot(f,Y_curr(1:NFFT/2+1),'r');
% else
%    Y_last = Y_curr;
%    Y_curr = 20*log10((2*abs(fft(win.*demod,NFFT))/NFFT)/1e-6);
%    plot(f,Y_last(1:NFFT/2+1),'g',f,Y_curr(1:NFFT/2+1),'r');
% end;
% xlim([0 320e3]);
% ylim([-80 60]);

%figure;
%plot(sig);

% figure;
% subplot(5,1,1);
% plot(tsamp,demod,'b');
% title('demod');
% subplot(5,1,2);
% plot(tsamp,diff_lst,'r');
% title('diff_lst');
% subplot(5,1,3);
% plot(tsamp,sig_sampled,'k');
% title('sig_orig');
% subplot(5,1,4);
% plot(tsamp,[0,diff(demod)],'r');
```

```
% title('diff_of_demod');
% subplot(5,1,5);
% plot(tsamp,PECM_lst,'g');
% title('PECM_lst');

%plot(tsamp,demod,'b', tsamp,diff_lst,'r+', tsamp,sig_sampled,'k', ...
%        tsamp,[0,diff(demod)],'b', tsamp, DIFM_lst, 'g');

% figure;
% [haxes,hline1,hline2] = plotyy(tsamp,sig_sampled,tsamp,PECM_lst);
% set(hline2,'LineStyle','--');
% xlabel('Time (s)');
% axes(haxes(1));
% ylabel('Radians');
% axes(haxes(2));
% ylabel('y_out[k]');
% legend('Input Waveform','y_out');

figure;
subplot(2,1,1);
plot(tsamp, sig_sampled);
ylabel('Input Waveform (Radians)','FontSize',24);
set(gca,'FontSize', 18);
subplot(2,1,2);
plot(tsamp, PECM_lst);
ylabel('y\_out(n)','FontSize',24);
set(gca,'FontSize', 18);
xlabel('Time (s)','FontSize',24);

cnr = 20*log10(Ac*2/(An))
error = 20*log10(max(demod)/max(sig))
db_ext = 20*log10(fr_sig/fr_demod)
max_difm = max(PECM_lst)
min_difm = min(PECM_lst)
```